Magnetic Activity of Neutron Stars and Black Holes

Ashley Bransgrove

Submitted in partial fulfillment of the
requirements for the degree of
Doctor of Philosophy
under the Executive Committee
of the Graduate School of Arts and Sciences

COLUMBIA UNIVERSITY

2023

© 2023

Ashley Bransgrove

All Rights Reserved

Abstract

Magnetic Activity of Neutron Stars and Black Holes

Ashley Bransgrove

This dissertation deals with the following topics related to the magnetic activity of neutron stars and black holes:

(I) Magnetic field evolution of neutron stars: We develop a numerical code which models the internal magnetic field evolution of neutron stars in axisymmetry. Our code includes the Hall drift and Ohmic effects in the crust, and the drift of superconducting flux tubes and superfluid vortices inside the liquid core. We enforce the correct hydromagnetic equilibrium in the core. We also model the elastic deformation of the crust and its feedback on the magnetic field evolution. We find that (i) The Hall attractor found by Gourgouliatos and Cumming in the crust also exists for B-fields which penetrate the core. (ii) If the flux tube drift is fast in the core, the pulsar magnetic fields are depleted on the Ohmic timescale ($\sim$ 150 Myr for hot neutron stars, or $\sim$ 1.8 Gyr for cold neutron stars such as recycled pulsars, depending on impurity levels). (iii) The outward motion of superfluid vortices during the rapid spin-down of a young highly magnetized pulsar, can partially expel magnetic flux from the core when $B \lesssim 10^{13}$ G.

(II) Neutron star quakes and glitches: We develop a theoretical model to explain the remarkable null pulse coincident with the 2016 glitch in Vela rotation. We propose that a crustal quake associated with the glitch strongly disturbed the Vela magnetosphere and thus interrupted its radio emission. We develop the first numerical code which models the global dynamics of a neutron

star quake. Our code resolves the elasto-dynamics of the entire crust and follows the evolution of Alfvén waves excited in the magnetosphere. We find that Alfvén waves launched by the quake become de-phased in the magnetosphere, and generate strong electric currents, capable of igniting electric discharge. Most likely, the discharge floods the magnetosphere with electron-positron plasma, quenching the pulsar radio emission. The observed ~0.2 s duration of the disturbance indicates that the crust is magnetically coupled to the superconducting core of the neutron star.

(III) Pulsar magnetospheres and radio emission: We present an extreme high resolution kinetic plasma simulation of a pulsar magnetosphere using the Pigeon code. The simulation shows from first-principles how and where radio emission can be produced in pulsar magnetospheres. We observe the self-consistent formation of electric gaps which periodically ignite electron-positron discharge. The gaps form above the polar-cap, and in the bulk return-current. Discharge of the gaps excites electromagnetic modes which share several features with the radio emission of real pulsars. We also observe the excitation of plasma waves and charge bunches by streaming instabilities in the outer magnetosphere.

(IV) Black hole magnetospheres and no-hair theorem: We explore the evolution of highly magnetized magnetospheres on Kerr black holes by performing general relativistic kinetic plasma simulations with the GRZeltron code, and general relativistic resistive magnetohydrodynamics simulations with the BHAC code. We show that a dipole magnetic field on the event horizon opens into a split-monopole and reconnects in a plasmoid-unstable current-sheet. The plasmoids are ejected from the magnetosphere, or swallowed by the black hole. The no-hair theorem is satisfied, in the sense that all components of the stress-energy tensor decay exponentially in time. We measure the decay time of magnetic flux on the event horizon for plasmoid-dominated reconnection in collisionless and collisional plasma.

Table of Contents

Acknowledgments ix

Preface 1

Chapter 1: Introduction 2

1.1 Neutron Stars 2

1.2 Black Holes 9

Chapter 2: Magnetic Field Evolution of Neutron Stars 12

2.1 Introduction 12

2.2 Equations and Formalism 15

2.3 Results 34

2.4 Discussion 53

Chapter 3: Pulsar Glitches and Star Quakes 58

3.1 Introduction 58

3.2 Vela Model 60

3.3 Quake Excitation of Shear Waves 63

3.4 Magnetospheric Waves and Electric Discharge 71

3.5 Setup of the Numerical Simulation 75

3.6 Sample Models 84
3.7 Discussion 90

Chapter 4: Pulsar Magnetospheres and Radio Emission 94
4.1 Introduction 94
4.2 Numerical Method 95
4.3 Magnetosphere Structure 96
4.4 Gaps and Electric Discharge 97
4.5 Discharge Waves 99
4.6 Instabilities 100
4.7 Discussion 102

Chapter 5: Black Hole Magnetospheres and No-Hair Theorem 104
5.1 Introduction 104
5.2 Numerical Method 105
5.3 Global Dynamics 107
5.4 Reconnection Dynamics 108
5.5 Flux Decay Rate 111
5.6 Emission 112
5.7 Discussion 113

Conclusion 115

References 118

Appendix A: Twist Evolution of the Core 133

Appendix B: Numerical Details of the Code 135

Appendix C: Elastic Modes 139

Appendix D: Crust Dynamics: Numerical Method 142

Appendix E: Magnetosphere Dynamics: Numerical Method 145

Appendix F: A Test for Wave Transmission 147

Appendix G: Dispersion Relation and Normal Modes of Pulsar Plasma 149

Appendix H: Beam Instability in Pulsar Plasma 151

Appendix I: Instability Growth Rate 153

Appendix J: Numerical Convergence 155

Appendix K: Collisionality of the Reconnection Layer 157

Appendix L: Magnetic Flux Decay Timescale 159

Appendix M: Luminosity 161

List of Figures

1.1 Dipole magnetic field strength vs. characteristic spin-down age of known galactic neutron stars. Data is from the ATNF pulsar catalogue [1]. 3

1.2 A superconducting flux tube (black curve) is pushed out of the core by the expanding neutron vortex array (vertical lines aligned with the angular velocity vector $\boldsymbol{\Omega}$): (a) Side view and (b) top view before expulsion, (c) top view after expulsion. Figure by M. Ruderman [7]. 4

1.3 An $e^{\pm}$ discharge in a gap (region of unscreened electric field $\boldsymbol{E} \cdot \boldsymbol{B} \neq 0$). An e^{-} (1) is accelerated along the magnetic field and emits a curvature photon (2) which converts to a secondary $e^{\pm}$ (3). The created $e^{\pm}$ creates further generations of pairs (4-7). Figure by M. Ruderman [44]. 8

1.4 Collapse of a magnetized star into a black hole. The star is surrounded by a vacuum dipole magnetosphere. The panels display (a) a star with a dipolar magnetic field, and (b) the black hole formed immediately after collapse. Panels (c) and (d) show the radiation of the dipole magnetic field in accordance with the no-hair theorem. Figure by K. Thorne [58]. 10

2.1 Snapshots of the magnetic field evolution for Model A (Table 2.1), shown at $t = 0$, 20 kyr, 200 kyr, and 2 Myr. The black curves are 10 contour lines of the poloidal flux function Ψ (i.e. the polodial magnetic field lines), equally spaced between $\Psi = 0$ and the maximum value $\Psi_{\rm max}$, at $t = 0$. The toroidal field is represented by the colour scale, which varies logarithmically, with a linear region around zero. . . 35

2.2 Snapshots of the evolution for Model A (Table 2.1), shown at $t = 0$ kyr, and 1 Myr. The plotting scheme is the same as Figure 2.1 but here colour shows $\Omega_{\rm e}$ (the angular velocity of the electron fluid), the result of Hall drift in the crust. The thickness of the crust has been magnified by a factor of 2.5. 36

2.3 Snapshots of the magnetic field evolution for Model B (Table 2.1), shown at $t =$ 0 kyr, 40 kyr, 400 kyr, and 2 Myr. The plotting scheme is the same as Figure 2.1. . 37

2.4 Snapshots of the magnetic field evolution for Model C (Table 2.1), shown at $t =$ 0 Myr, 10 Myr, 20 Myr, and 45 Myr. The plotting scheme is the same as Figure 2.1. The toroidal field is everywhere zero. 41

2.5 Decay of the dipole field for the magnetic field evolution shown in Figure 2.4. . . . 42

2.6 Plane parallel slab (grey), with length l. Field lines (blue) move to the right consistent with the rate set by Ohmic diffusion. 43

2.7 Snapshots of the magnetic field evolution for Model D1 (Table 2.1), shown at $t = 0$ kyr, 5 kyr, 100 kyr, 1 Myr, 2 Myr, and 4 Myr. The plotting scheme is the same as Figure 2.1. This simulation begins 300 yr after the neutron star birth, with surface field strength $\sim 5 \times 10^{12}$ G, and spin period 10.9 ms. 44

2.8 Snapshots of the magnetic field evolution for Model D2 (Table 2.1), shown at $t = 0$ kyr, 5 kyr, 50 kyr, 250 kyr, 1 Myr, and 3 Myr. The plotting scheme is the same as Figure 2.1. This simulation begins 300 yr after the neutron star birth, with surface field strength $\sim 10^{13}$ G, and spin period 21.8 ms. 45

2.9 Snapshots of the magnetic field evolution for Model D3 (Table 2.1), shown at $t = 0$ kyr, 5 kyr, 50 kyr, 150 kyr, 1 Myr, and 3 Myr. The plotting scheme is the same as Figure 2.1. This simulation begins 300 yr after the neutron star birth, with surface field strength $\sim 2 \times 10^{13}$ G, and spin period 43.5 ms. 46

2.10 Snapshots of the magnetic field evolution for Model E (Table 2.1), shown at $t = 0$ kyr, 3 kyr, 6 kyr, and 9 kyr. Top row: The plotting scheme is the same as Figure 2.1. Bottom row: Lagrangian displacement of the crust is shown on the colour scale which varies logarithmically, with a linear region around zero. The thickness of the crust has been magnified by a factor or 2.5 in both rows. 50

3.1 Schematic picture of the neutron star and its magnetosphere, indicating relevant length scales and characteristic densities. The gray shaded region represents the closed magnetosphere. 62

3.2 Wave speed $\tilde{v}_s(\rho)$ in the magnetosphere, ocean, crust, and core (thick black line). The dashed line shows the Alfén speed $v_A(\rho)$, and the dotted line shows the elastic wave speed $v_s(\rho)$. 65

3.3 Top: initial conditions used for models A1 and A2. Bottom: initial conditions used for models B1 and B2. Color shows the amplitude of the azimuthal displacement ξ_ϕ. The amplitude is scaled so that each initial condition has the initial energy $E = 10^{38}$ erg. The gray dashed lines show the boundaries of the crust. 87

3.4 Model A1 at $t = 2$ ms. Top left: displacement ξ_ϕ of the crust near the epicenter of the quake. The dashed lines show the boundaries of the crust. Top right: toroidal perturbation of the magnetic field B_ϕ/B (left), and the ratio $|j_{\|}/c\rho_{GJ}|$ (right). The green curves show the poloidal magnetic field. The two field lines closest to the axis of symmetry are the boundary of the open field-line bundle. The gray dashed circle is the surface of the neutron star. Bottom: displacement $\xi_\phi(r,\theta)$ in the entire crust, plotted on the r-θ plane. 88

3.5 Same as Figure 3.4 but at time $t = 50\,\mathrm{ms}$. 88

3.6 Model B1 at $t = 2$ ms. Top left: displacement ξ_ϕ of the crust near the epicenter of the quake. The epicenter is at $\theta = 45\,^\circ$, and we have rotated the figure by $-45\,^\circ$ ($\tilde{x} = x - z$ and $\tilde{z} = x + z$). The dashed lines show the boundaries of the crust. Top right: toroidal perturbation of the magnetic field B_ϕ/B (left), and the ratio $|j_{\|}/c\rho_{GJ}|$ (right). The green curves show the poloidal magnetic field. The two field lines closest to the axis of symmetry are the boundary of the open field-line bundle. The gray dashed circle is the surface of the neutron star. Bottom: displacement $\xi_\phi(r,\theta)$ in the entire crust, plotted on the r-θ plane. 89

3.7 Same as Figure 3.6 but at time $t = 50\,\mathrm{ms}$. 89

3.8 Luminosity of Alfvén waves emitted into the magnetosphere, L_A. The luminosity has been averaged into 20 ms bins to remove the noise from fast oscillations. Left: models A1 and A2 (initial quake under the polar cap). Right: models B1 and B2 (initial quake at $\theta \sim \pi/4$). Red is used for models with no crust-core coupling (A1 and B1), and blue for models with strong crust-core coupling (A2 and B2). For each model, we show L_A from the entire stellar surface (solid curve), and the contributions from the north (dashed) and south (dotted) polar caps. 90

3.9 Evolution of the quake energy. The four panels show the results for models A1, A2, B1 and B2. The energy retained by the crustal oscillations E_crust (dashed curve) is reduced by the transmission into the magnetosphere (dotted) and (in models A2, B2) transmission into the core (dotted-dashed). As required by energy conservation, the sum of the retained and transmitted energies remains equal to $E_Q = 10^{38}$ erg (horizontal solid line). The blue dashed line shows the analytical approximation to $E_\mathrm{crust}(t)$ (Equation 3.77) with $\tau_\mathrm{core} = 86$ ms. 91

4.1 Plasma density n (color bar) in the quasi-steady state. The vertical axis shows distance along the spin axis. Green curves show poloidal magnetic field lines. The dense clouds of plasma above the polar cap form in $e^\pm$ discharge episodes. The absence of plasma (dark zone) above the separatrix shows the return-current gaps in the unscreened state; it fills with plasma every $\sim 2R_\mathrm{LC}/c$ when the return-current discharges ignite. 96

4.2 Excitation of plasma waves in the pulsar magnetosphere. The vertical axis shows distance along the spin axis, and the color bar shows components of the electromagnetic field multiplied by $(r/r_\star)^2$. Top : $E_{||}$ in the quasi-steady state. The dashed white curve shows the null-surface $\rho_\mathrm{GJ} = 0$ (the null-surface breathes outside r_LC due to plasmoid motion). Insets (i)-(iii): Electromagnetic modes excited during $e^\pm$ discharges at the polar-cap, inner return-current, and outer return-current gaps. Inset (iv): Waves excited by a streaming instability. For insets (i) and (ii), $\delta E_\perp$ lies in the poloidal plane. 98

4.3 Streaming instabilities in the outer magnetosphere. Left: Parallel momentum ($p_{||}$) distributions of $e^\pm$ (grey) and gamma-rays (cyan) in regions (a) and (b) in the right panel. For gamma-rays we show distributions of $p_{||}/2$ (their momentum is split between the created e^+ and e^-). (a): Gamma-rays from the current-sheet (cyan peak) inject $e^\pm$ (grey peak). (b): Gamma-rays from the separatrix (thin cyan peak) and the current-sheet (wider cyan peak) inject different $e^\pm$ beams. Right: Charge density ρ and charge bunch formation. 101

5.1 Reconnecting magnetosphere in the FIDO frame (GRPIC1) at $t = 100\, r_g/c$. Green curves show poloidal magnetic flux surfaces, and white curves show the boundary of the ergosphere. The black circle is the interior of the BH event horizon. Left: Color shows radial and θ components of the bulk plasma 3-velocity in the orthonormal tetrad basis. The grey dashed curve indicates the stagnation surface defined by $\langle v^r \rangle = 0$. Right: Azimuthal component of the auxiliary field $\boldsymbol{H}$. 108

5.2 Different realizations of the reconnecting magnetosphere in the FIDO frame. Color shows the cold plasma magnetization σ. Top: GRPIC1 at $t = 100\ r_g/c$, $\sigma = B^2/(4\pi mnc^2)$. Bottom: GRRMHD1 at $t = 311\ r_g/c$, $\sigma = B^2/(4\pi\rho c^2)$. The GRPIC simulation (top) displays larger plasmoids than GRRMHD (bottom) due to the faster reconnection rate. 110
5.3 Flux on the event horizon vs time for vacuum (power law decay), collisional MHD plasma (exponential decay), and collisionless plasma (faster exponential decay). . . 111
5.4 Reconnecting magnetosphere in 3D (GRRMHD2) at $t = 118\ r_g/c$. Left: Volume rendering shows $\sigma = B^2/(4\pi\rho c^2)$, green tubes are magnetic field-lines which penetrate the event horizon, red tubes are magnetic field-lines which are reconnecting in the current-sheet. Right: 2D slice of GRRMHD2 in the $\phi = 0$ half-plane. Color shows σ, green curves are magnetic field-lines in the $\phi = 0$ half-plane. The picture highlights the non-axisymmetric nature of reconnection in 3D, yet still displays similar fundamental structures — X-points (inset 1), and helical winding of magnetic field-lines in plasmoids (flux ropes) (inset 2). 112

F.1 Left: initial energy spectrum of waves in this test problem. Right: transmission coefficient of waves into the magnetosphere $\mathcal{T}_m(\omega)$. The thick black line shows the transmission coefficient found by solving the analytic reflection conditions (Section 3.3), and the gray dots show the numerical transmission coefficient measured using our code for an $l = 0$ radial wave. The dotted lines show the powe-law scalings in each frequency range. 147

J.1 Convergence study for each simulation. Left: Flux on the event horizon vs time at 2 resolutions for each of the simulations GRPIC1, GRPIC2, and GRPIC3. Right: Flux on the event horizon vs time at 3 resolutions for simulation GRRMHD1 and GRRMHD2. 155
J.2 AMR blocks used in the simulation GRRMHD1, with inset zoomed on the current sheet near the event horizon. Color shows magnetization $\sigma = B^2/(4\pi\rho c^2)$, and the red curve shows the ergosphere boundary. 156

K.1 Elementary current-sheet width w and plasma skin depth λ_p vs magnetic field strength in the upstream, B. 158

M.1 Flux of conserved energy through spherical shells of radius r, as seen by an observer at infinity in units of L_{BZ}. Left panel: GRPIC1 at $t = 100\ r_g/c$. Right panel: GRRMHD1 at $t = 311\ r_g/c$. 161

List of Tables

2.1 Summary of the models we discuss in Section 2.3. Here HME (relaxation) implies hydromagnetic equilibrium enforced by the relaxation method in Section 2.2.4. HME (trivial) is for symmetric configurations where the toroidal field remains zero in the core according to hydromagnetic equilibrium. 31

3.1 Sample models. 85

5.1 Summary of the simulation parameters. For all GRRMHD runs the diffusivity is $\eta = 10^{-5}$. For MHD runs $N_r \times N_\theta \times N_\phi$ refers to the effective resolution. Runs with $N_\phi = 1$ are axisymmetric, while those with $N_\phi > 1$ refer to 3D simulations. All models have spin $a = 0.99$ except VAC0, which has $a = 0$. 106

B.1 The grid resolution used in the crust and core for each of the Models A-E. 135

Acknowledgements

First and foremost I would like to thank my thesis advisors Andrei Beloborodov and Yuri Levin. I will be forever grateful for their patience, support, and the freedom they gave me to pursue my research interests. It is difficult to overstate the profound impact they have had on my development as a scientist and my life as a whole.

I give my deepest thanks to Sasha Philippov and Bart Ripperda for their friendship, mentorship, and for introducing me to black holes. They helped me immensely during postdoc applications and throughout my PhD. Both have been steady sources of high quality advice; scientific and otherwise. Chapter 5 of this dissertation would not exist without them.

I thank Mal Ruderman for his mentorship, friendship, and for the many times he invited me to his home. I will always treasure the time we spent inside a neutron star.

I thank Rui Hu for the infinite patience he displayed when teaching me how to use his Pigeon code. I also thank Andrei Gruzinov, Xinyu Li, Daniel Price, Chris Matzner, Alex Chen, and Yajie Yuan for useful discussions. I thank Kostas Gourgouliatos and Andrew Cumming for sharing data to test my Hall drift code, and Paul Lasky and Greg Ashton for enlightening discussions about the 2016 Vela glitch. I thank my friends at Columbia for their company: Bhavya, Ben, Rocco, Simon, Daniel, Sebastian, and all the others.

Lastly I thank my family for their love and support, and my beautiful wife Arzoo, for waiting.

Preface

Magnetic fields are familiar in the laboratory, and indeed the household, where their properties are well known; they are easily controlled, and they serve at our beck and call. In the large dimensions of the astronomical universe, however, the magnetic field takes on a role of its own, quite unlike anything in the laboratory. The magnetic field exists in the universe as an 'organism', feeding on the general energy flow from stars and galaxies ... Over astronomical dimensions the magnetic field takes on qualitative characteristics that are unknown in the terrestrial laboratory. The cosmos becomes the laboratory, then, in which to discover and understand the magnetic field and apprehend its consequences.

— E. N. Parker (1979)

Chapter 1: Introduction

Neutron stars and black holes are the most exotic objects in the universe. They are the graveyard of stellar evolution; formed when normal stars run out of fuel to support themselves against gravitational collapse. Isolated neutron stars and black holes are cold dead objects which are devoid of chemical and nuclear reactions to heat their interiors. It is somewhat surprising then, that they are prolific sources of electromagnetic activity. The origin of the activity can be traced to the magnetic field. Although these objects have depleted all fuel, they are magnetically alive. Neutron star interiors are threaded by ultra-strong magnetic fields, and they are surrounded by active plasma magnetospheres. Black holes may be born with plasma magnetospheres, or acquire them later in life by accreting magnetized matter. From the theoretical perspective, the magnetic activity of neutron stars and black holes is poorly understood.

1.1 Neutron Stars

Since the discovery of the first pulsar more than fifty years ago theorists have been trying to understand the puzzling behavior of neutron stars. The abundance of rich observations has made neutron stars objects of intense interest, however understanding their dynamics has proved difficult. In the last decade numerical plasma simulations have made substantial progress in modeling emission from pulsar magnetospheres. The internal dynamics of neutron stars has proved considerably more challenging, with much unknown, and few firm theoretical results. This dissertation attempts to address several aspects of neutron star internal dynamics and magnetospheric emission including (i) magnetic field evolution (Chapter 2), (ii) glitches and star quakes (Chapter 3), and (iii) radio emission, gaps, and instabilities in pulsar magnetospheres (Chapter 4).

1.1.1 Magnetic Field Evolution

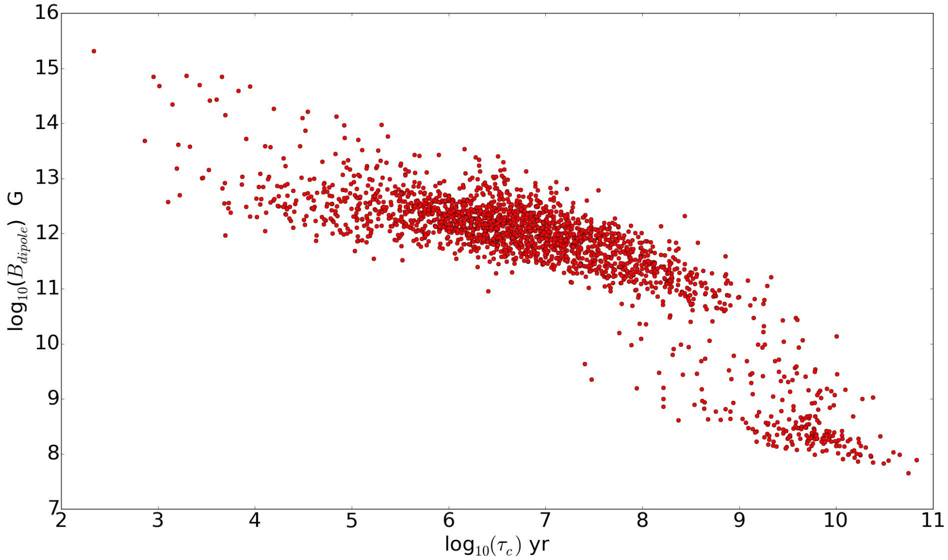

Figure 1.1: Dipole magnetic field strength vs. characteristic spin-down age of known galactic neutron stars. Data is from the ATNF pulsar catalogue [1].

Pulsars are rapidly rotating, magnetized neutron stars, which emit powerful beams of coherent radio emission. Young pulsars have spin periods of tens of milliseconds to seconds, and magnetic field strength of order $10^{11} - 10^{12}$ G (eg. [2]), inferred from dipole braking spin-down (Fig. 1.1). Millisecond pulsars are a subclass of radio pulsars which have spin periods 1.4 ms to $\sim$ 10 ms, characteristic ages $\sim 10^9 - 10^{10}$ years, and far weaker magnetic fields ($\sim 10^8 - 10^{10}$ G, Fig. 1.1). Approximately 60% of millisecond pulsars exist in binary systems [1]. This leads to the hypothesis that many millisecond pulsars were once regular pulsars, which spin-down below the radio death-line by magnetic braking, and then spin-up by accretion from a companion star. These are the so-called recycled pulsars. The depletion of pulsar magnetic fields during this process is not well understood. One possibility is the burial of the surface field by the accretion flow (see eg. [3–5], [6]). Another is expulsion of magnetic flux from the core ([7, 8]).

The most extreme class of neutron stars is magnetars. Canonical magnetars are persistent X-ray sources which are powered by dissipation of free energy stored in ultra-strong magnetic

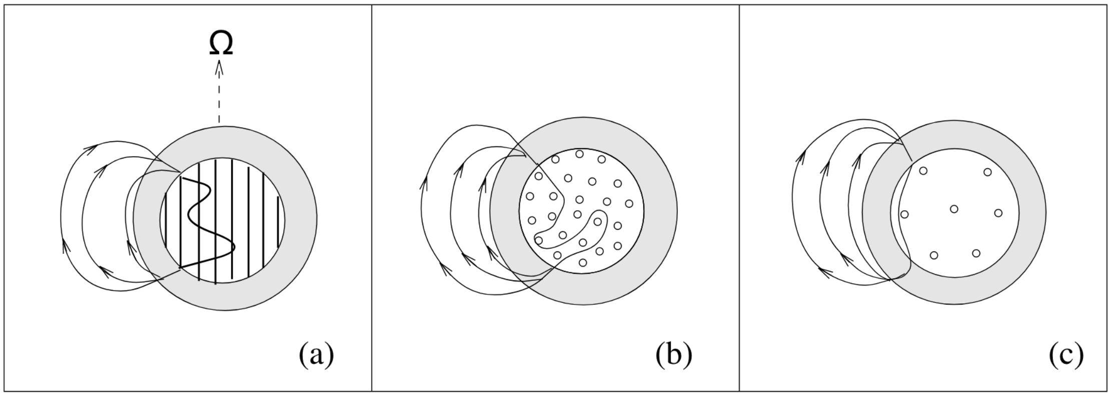

Figure 1.2: A superconducting flux tube (black curve) is pushed out of the core by the expanding neutron vortex array (vertical lines aligned with the angular velocity vector $\boldsymbol{\Omega}$): (a) Side view and (b) top view before expulsion, (c) top view after expulsion. Figure by M. Ruderman [7].

fields ($10^{14} - 10^{15}$ G) in their interiors ([9], see also [10] for a review). Magnetars also display several types of extreme transient emission, including the months-long ‘outbursts’ during which their X-ray flux increases up to a factor of ~ 1000 compared to the quiescent emission [10]. They also emit short hard X-ray bursts [11] and fast radio bursts (FRBs) [12]. The most spectacular radiative phenomena are the magnetar giant flares which peak in the soft γ-ray band, and reach luminosities up to 10^{47} erg s^{-1}. The magnetar activity is believed to be due to the evolution of super-critical magnetic fields which shear the crust, and strongly disturb the magnetosphere ([13–15], [16]). However, the transport of magnetic stress and energy from the neutron star interior into the magnetosphere is not well understood.

Neutron star crusts consist of a solid ion lattice immersed in a sea of relativistic electrons. Free neutrons are present at densities greater than neutron drip $\rho_{\rm drip} \approx 4.3 \times 10^{11}$ g cm^{-3} [17]. The core is a soup of neutrons, protons, and electrons. The neutron star matter is highly degenerate, and scattering of charged particles is strongly suppressed except for those near the fermi surface. Therefore, electrical currents (and magnetic fields $\nabla \times \boldsymbol{B} = [4\pi/c]\boldsymbol{j}$) in neutron star interiors are generally expected to persist for a very long time.

Magnetic field evolution in the crust is due to Hall drift (advection of magnetic field lines by electron currents), and ohmic diffusion (dissipation of electron currents due to finite resistivity of the crustal matter) [18, 19]. When neutron stars are young and hot the main channel for magnetic field evolution in the core is ambipolar diffusion [19, 20] — drift of magnetic field lines (and proton-electron plasma) relative to the neutron liquid. Friction on the plasma is due to strong nuclear collisions of protons and neutrons. Hall drift, ohmic diffusion, and ambipolar diffusion are generally well understood effects in plasma astrophysics, however little work has been done on global self-consistent neutron star models which include crust-core coupling. Several works have considered magnetic evolution in the crust and the core as separate components [21–25].

When a neutron star has cooled sufficiently nucleons in the core form Cooper pair condensates which are described by macroscopic wavefunctions [26]. The critical temperatures of the phase transitions are uncertain, but higher than the observed temperatures of all but the youngest neutron stars [27]. The protons are expected to form a type-II superconductor with the magnetic flux quantized in an array of microscopic flux tubes [28]. Similarly, the neutrons are expected to become superfluid, with the macroscopic rotation of the star manifested in an array of microscopic quantum vortices [29]. As the star spins down due to magnetospheric torques, the neutron vortex array expands outward. The neutron vortices are magnetized (due to the entrainment effect), and their outward motion may push flux tubes out of the core (Fig. 1.2) [7, 30, 31]. However there is considerable controversy over the flux tube friction and the flux tube equation of motion [8, 32]. Magnetic field evolution of superconducting neutron stars is therefore less certain than the normal case.

Chapter 2 of this dissertation explores the evolution of magnetic fields inside strongly magnetized neutron stars in axisymmetry. We present models which include the Hall drift and Ohmic effects in the crust, and the drift of superconducting flux tubes and vortices inside the core. We also include the elastic deformation of the crust and it's feedback on the magnetic field evolution. We find that including the crust-core coupling results in a dramatically different evolution than models which consider the crust and the core as separate components.

1.1.2 Glitches

Pulsars are highly stable rotators which slowly spin down due to magnetospheric torques. However they show two types of rotational irregularity dubbed timing noise and glitches. Timing noise is the slow stochastic deviation from regular spin-down, most prominent in young pulsars [33, 34]. A glitch is a sudden increase in the spin frequency ν, sometimes accompanied by a change in the spin-down rate $\dot{\nu}$. The first pulsar glitch was observed in the Vela pulsar [35], and by now there are more than 520 recorded glitches in 180 pulsars [36] with glitch magnitude (relative frequency change) ranging from $\Delta\nu/\nu \approx 10^{-12}$ to $\Delta\nu/\nu \approx 10^{-5}$ [37]. The so-called 'Crab-like' pulsars feature strong jumps in spin-down rate with $\Delta\dot{\nu}/\dot{\nu} \gg \Delta\nu/\nu$, power-law glitch-size distributions, and exponential wait-time distributions [38]. The so-called 'Vela-like' pulsars glitch quasi-periodically, with consistently large magnitude [37].

The standard theoretical picture of a pulsar glitch involves a sudden transfer of angular momentum to the crust due to the catastrophic unpinning of superfluid vorticity [39]. In this picture, the crust (ion lattice) spins down due to external torques while the rotation of the crustal neutron superfluid remains unchanged as long as its vorticity (quantized vortices) is pinned to the lattice. When the rotation mismatch builds up to some threshold, many vortices are unpinned simultaneously and migrate away from the axis of rotation, spinning down the superfluid and spinning up the crust, thus bringing the two components closer to corotation. The mechanism which causes the nearly simultaneous unpinning of billions of superfluid vortices remains a mystery.

The origin of pulsar glitches has been difficult to probe observationally because they occur in the neutron star interior, and electromagnetic counterparts (if they exist) are challenging to detect. In Chapter 3 of this dissertation we discuss the recent first ever observation of a radiative change associated with a glitch in a canonical radio pulsar [40]. We present a star quake model which can explain the coincidence of the glitch and the major magnetospheric transient which switched off the pulsar radio emission.

1.1.3 Magnetospheres and Radio Emission

Although pulsar radio emission constitutes a very small fraction of the available spin-down power ($L_{\mathrm{radio}}/L_{\mathrm{sd}} \sim 10^{-6}$), theorists have been fascinated by it's rich phenomenology for decades. The emission is coherent and broadband, and has been observed from 10's of MHz to ~ 350 GHz [41]. The radio emission from most normal (non-recycled) pulsars occupies a small extent of the rotational phase, which is consistent with an emission site on the narrow open field lines above the pulsar polar cap. While individual pulses are highly variable, integrating (averaging) over hundreds or thousands of pulses yields a stable profile which is unique to a given pulsar. The integrated profiles often contain multiple components. The emission is mostly linearly polarized with some pulsars displaying a considerable fraction of circular polarization. Individual pulses often display 'microstructure' (short quasi-periodic pulses superimposed on the broader pulse envelope), which may be a signature of the underlying emission mechanism (for a recent review see [42]).

The problem of pulsar radio emission is well defined and simple to formulate. One must understand the mechanism which generates radio frequency waves in the highly magnetized plasma near the neutron star surface. The physical ingredients which enter the problem are as follows: On the short light-crossing timescales of interest, the star is a perfect conductor with the magnetic field frozen-in. Rotation of the magnetized conductor induces a voltage which lifts electrons and ions from the stellar surface [43]. Particles are confined to move along the field lines like beads on a wire. Electrons emit gamma-rays by curvature emission as they move along the curved field lines. Near the star the gamma-rays convert to $e^{\pm}$ off the ultra-strong magnetic field [44]. Further away from the star, the magnetic field is weaker, and the dominant channel for $e^{\pm}$ creation is photon collisions. The created $e^{\pm}$ plasma is collisionless and very highly conducting because the mean-free path for Coulomb collisions is larger than the system size. The $e^{\pm}$ plasma supports only three propagating eigenmodes: the Alfvén mode, the superluminal ordinary (O) mode, and the extraordinary (X) mode [45]. Any theory of pulsar radio emission must account for (i) the production of $e^{\pm}$ pair plasma which occurs on the open magnetic field lines, and (ii) the excitation of one of the eigenmodes of the plasma. The propagation of the excited mode through the magnetosphere and its escape as observable radiation is also an important (but non-trivial) problem [45–48].

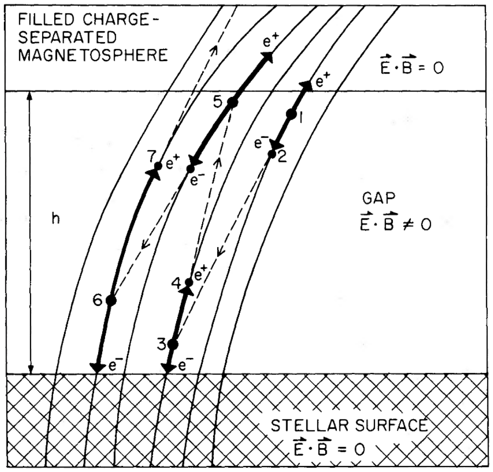
FILLED CHARGE-
SEPARATED
MAGNETOSPHERE
$\vec{E}\cdot\vec{B} = 0$
h
GAP
$\vec{E}\cdot\vec{B} \neq 0$
STELLAR SURFACE
$\vec{E}\cdot\vec{B} = 0$
e^+
e^-
1
2
3
4
5
6
7

Figure 1.3: An $e^{\pm}$ discharge in a gap (region of unscreened electric field $\boldsymbol{E} \cdot \boldsymbol{B} \neq 0$). An e^- (1) is accelerated along the magnetic field and emits a curvature photon (2) which converts to a secondary $e^{\pm}$ (3). The created $e^{\pm}$ creates further generations of pairs (4-7). Figure by M. Ruderman [44].

Early models of the radio emission mechanism invoked masers and beam plasma instabilities. However maser models were not widely accepted, and the growth rate of streaming instabilities in relativistic pair plasma is strongly suppressed by the ultra-high Lorentz factor of the particles (for a detailed discussion see [42]). More recently it was proposed that the $e^{\pm}$ discharge in a gap (Fig 1.3) could directly excite electromagnetic waves [49–51]. The problem is difficult because plasma currents in the gap are determined by the physics of $e^{\pm}$ discharge (Fig. 1.3) which is highly time dependent. On the other hand, the current must be consistent with $\nabla\times\boldsymbol{B}$ required by the global magnetosphere. A self-consistent solution is required, and it is provided by modern numerical simulations.

The particle-in-cell (PIC) method solves kinetic plasma dynamics on a computer [52–56]. Plasma particles are moved by the electromagnetic field, and the evolution of the field (on a discrete grid) is in turn determined by the particle motion, forming a well-defined non-linear dynamical system. Local one dimensional (1D) PIC simulations demonstrated the direct excitation of plasma waves during a polar cap $e^{\pm}$ discharge [49, 57]. However, due to symmetries of the simplified 1D setup, the waves were purely electrostatic in nature, and did not propagate in the plasma rest-frame.

The seminal work by [50] showed that pulsar radio emission can be generated directly by the time-dependent $e^{\pm}$ discharge above the polar-cap. The authors performed local 2D PIC simulations of a polar cap gap in cartesian geometry, and showed that electromagnetic (O-mode) waves are generically excited in powerful discharges. The location of the $e^{\pm}$ discharge and wave excitation depends on the large-scale currents and non-local plasma supply in the global magnetosphere.

Global PIC simulations with self-consistent $e^{\pm}$ creation are essential to determine the geometry of radio emitting regions in pulsar magnetospheres, but so far they have been unable to achieve sufficient spatial resolution due to the prohibitive computational cost. In Chapter 4 of this dissertation we present the largest ever global kinetic plasma simulation of a pulsar magnetosphere. For the first time we achieve sufficient spatial resolution to resolve wave excitation by electric discharges and plasma streaming instabilities in a global magnetosphere.

1.2 Black Holes

The study of black holes began as a purely theoretical endeavor. However, with the development of X-ray telescopes in the 1960's and the recent horizon scale observations by EHT (event horizon telescope), it is now essential to understand their emission. This dissertation explores the evolution of plasma-filled magnetospheres on Kerr black holes (Chapter 5).

1.2.1 Magnetospheres

The no-hair theorem states that the global spacetime metric of isolated black holes is completely described by three parameters: the mass, spin, and electric charge [59]. All other fields (hair) are radiated away or swallowed by the black hole on a light crossing timescale in order to reach this asymptotic state. The classical example is a black hole which formed by the collapse of a magnetized star (Fig. 1.4). The star is assumed to be highly conducting so that the magnetic field lines are frozen-in, and the magnetosphere is assumed to be vacuum (no plasma). When the star collapses, the in-falling matter pulls magnetic field lines through the newly formed event horizon. The magnetic field which remains outside the event horizon is then radiated away as vac-

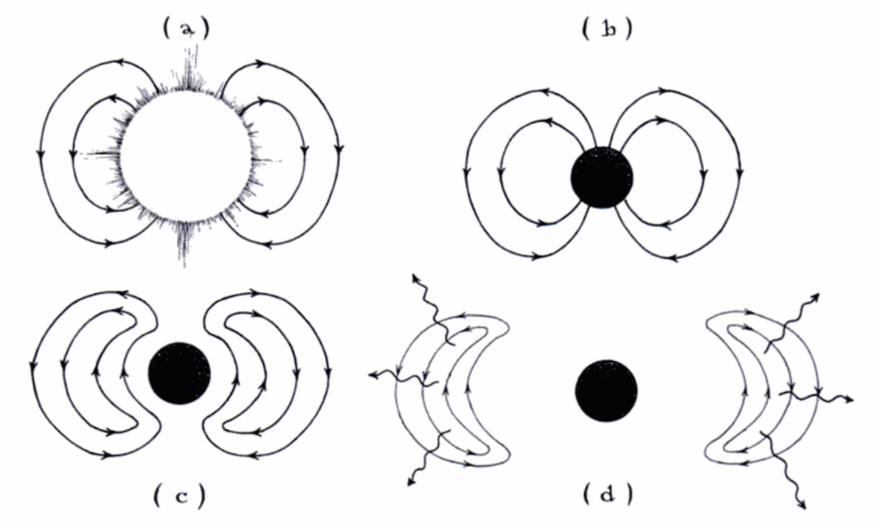

Figure 1.4: Collapse of a magnetized star into a black hole. The star is surrounded by a vacuum dipole magnetosphere. The panels display (a) a star with a dipolar magnetic field, and (b) the black hole formed immediately after collapse. Panels (c) and (d) show the radiation of the dipole magnetic field in accordance with the no-hair theorem. Figure by K. Thorne [58].

uum waves. The problem as formulated in this way is well studied but unrealistic. Plasma will inevitably exist in the magnetosphere around the newly formed event horizon. Furthermore, black holes can generate a self-regulated plasma supply through electron-positron discharges near the event horizon [60–62]. The discharges can fill the magnetosphere with plasma in a light crossing timescale.

The presence of highly conducting plasma dramatically changes the vacuum electrodynamics assumed in the classical no-hair theorem (Fig. 1.4). In the limit of vanishing resistivity, the flux on the event horizon is perfectly conserved, and the magnetic field cannot slide off the event horizon [63]. The only way for the black hole to lose its magnetic field is for the field to change its topology (reconnect). Fast magnetic reconnection occurs through the tearing instability [64]. A chain of plasmoids (magnetic loops containing plasma) forms along the reconnection layer which are ejected at relativistic velocities. For highly magnetized collisionless plasma (as expected in a black hole magnetosphere), the reconnection rate $v_{\rm rec} \sim 0.1c$ is independent of the magnetization [65–67]. The lifetime of the magnetic flux on the event horizon should be determined in part by this universal reconnection rate.

Previous work in an ideal fluid approximation correctly established the qualitative evolution of a dipole magnetic field on the event horizon [63]. However, it neglected collisionless physics, and was performed at low numerical resolution such that the magnetic reconnection was not in the correct asymptotic regime of high Lundquist number [63, 68]. This lead to the incorrect conclusion of an extremely long lifetime of the magnetic flux on the event horizon, dictated by the resistive timescale of the plasma [63].

In Chapter 5 of this dissertation we present GRPIC (general-relativistic particle-in-cell) and GRRMHD (general-relativistic resistive magnetohydrodynamics) simulations which are converged and produce the correct reconnection physics. We show that the no-hair theorem is satisfied, in the sense that all components of the stress-energy tensor decay exponentially in time, and we measure the decay time of magnetic flux on the event horizon.

Chapter 2: Magnetic Field Evolution of Neutron Stars

2.1 Introduction

There is a rich variety of neutron stars with magnetic field strengths which differ by several orders of magnitude, and vastly different behaviors. The evolution of neutron star magnetic fields can provide insight into the origin, behavior, and populations of neutron stars [eg. [69]].

There are several well defined classes of neutron stars, with a number of transient objects displaying behavior somewhere between these classifications, which suggests that the galactic population of neutron stars may be explained by different ages and birth field strengths. The discovery of radio emission from magnetars [70], and X-ray bursts from so-called “high-B pulsars" [71] adds evidence to this argument. While observations point to a unification of neutron star classes [72], further theoretical work is required to complete this picture. Recent discussion of a unification was based on the models of magnetic field and thermal evolution [73]. It is likely that any such unification would see a given neutron star traverse a variety of classes over the course of its life, with its classification at any time having a strong dependence on magnetic field strength, and configuration. Indeed studying the evolution of neutron star magnetic fields is key to understanding how a neutron star may transition from one class of object to another.

The evolution of magnetic fields in neutron star crusts is due to Hall drift and Ohmic diffusion. It was studied by [18], and more definitively by [19]. Hall drift is the non-linear advection of magnetic fields, by the electron currents supporting $\nabla \times \boldsymbol{B} = 4\pi/c\boldsymbol{j}$. The Hall effect can generate large magnetic shear stresses, countered by the solid stress of the crust. In reality the crust yields elastically to Hall-induced stresses up to a point, beyond which it deforms in the plastic regime [see eg. [14, 16, 74]]. Ohmic diffusion is caused by the finite resistivity of the crustal material due to electron scattering by the ion lattice. This process converts magnetic energy to heat, in contrast to Hall drift which conserves magnetic energy. In neutron stars with magnetic fields $B \gtrsim 10^{13}$ G, the Hall timescale is shorter than the Ohmic timescale, making Hall drift the dominant channel of evolution for the crustal magnetic field.

Advances in numerical techniques have allowed Hall drift and Ohmic diffusion of 2D axisymmetric magnetic fields to be studied in numerical simulations, with a variety of pseudo-spectral and grid based methods [[75], [22], [23]]. The basic finding was that Hall drift could enhance the transfer of magnetic energy to smaller scales, where Ohmic diffusion proceeds more efficiently. [24] found that Hall drift drives itself toward a configuration with uniform electron angular velocity along poloidal field lines. This “Hall attractor" is analogous to Ferraro’s Law in ideal MHD, in which twisted field lines in a cylindrical configuration will evolve to a state with constant angular velocity along field lines [76]. The Hall attractor has interesting implications for the active periods of magnetars and other transients. Most recently Hall drift has been simulated numerically in 3D [77]. [78] found that Hall drift can generate localized patches of high magnetic field strength in a magnetar crust, where significant heat can be generated through Ohmic diffusion.

The majority of numerical studies of magnetic field evolution in neutron star crusts do not include the coupled evolution of the core magnetic field. Considerable work has gone into modeling fields which are confined to the crust, however there is no reason why this should be so. Only one numerical study of the coupled crust-core evolution has been published [79]. This paper presents our first step in building detailed numerical models for the B-field evolution in neutron stars that include the field in both the crust and the core, with important differences from [79]. Namely, 1. We enforce the correct hydromagnetic equilibrium in the core, 2. We model the twist exchange between the crust and the core, 3. We consider much faster evolutionary timescales for the core magnetic field, and 4. We model the elastic back-reaction on the magnetic field evolution in the crust.

There are a number of proposed channels of evolution for the core magnetic field. Most well known is the ambipolar diffusion [19], which is the evolution induced by the drift of the charged component through the neutral one, ie. the drift of the proton-electron plasma through the neutrons. Ambipolar diffusion is limited by two factors. Firstly, there is friction between protons and the background neutron fluid. Secondly, departures from chemical equilibrium create pressure gradients which choke the flow of charge currents. Gradients in chemical potential can be erased by weak nuclear interactions. Recently ambipolar diffusion was modeled in 2D by [25].

Neutron stars cool as they age and their cores are expected to become superconducting and superfluid (unless the magnetic field is ultra-strong, $B > 10^{16}$ G, and quenches superconductivity). This results in the quantization of vorticity into vortex lines and magnetic flux – into flux tubes. An important magnetic flux transport mechanism is the drift of superconducting flux tubes. [8] shows that flux tubes in a superconducting core can move with viscous dissipation through the core fluid, under their own self tension. The drift of flux tubes has a typical velocity $v \approx 4 \times 10^{-7}$ cm s^{-1} for typical pulsars [see section 3 of [8]], making this effect relevant to the depletion of pulsar magnetic fields. We note straight out that this result is controversial, and there is no consensus about it in the theoretical literature; we discuss it below. Furthermore, [29] pointed out that the spin-down of superfluid neutron stars must be associated with the outward motion of superfluid neutron vortices. [30], and [7] showed that due to entrainment of superfluid protons the neutron vortices have spontaneous magnetization and that as consequence, there is a strong interaction between superfluid vortices and superconducting flux tubes. In this picture, the flux tubes may be pulled along with neutron vortices during spin-down.

Axisymmetric magnetic configurations satisfy an MHD equilibrium condition in the core, which we formulate and implement in our simulations. We find that with this equilibrium, the magnetic field in the crust and the core asymptotically settles into the Hall Attractor of [24], which was established for crust-confined fields. We explore the evolution of the core magnetic field under Jones' flux tube drift. Our simulations suggest that a combination of Jones' flux tube drift in the core, and Ohmic diffusion in the crust can deplete pulsar magnetic fields on a timescale of 150 Myr, if the crust is hot ($T \sim 2 \times 10^{8}$ K). We also consider the hypothesis that a weak-field magnetar can be produced by a neutron star with initially rapid spin and dipole field smaller than the conventional magnetar field. In this scenario, the field is pushed out by the neutron vortices into the crust and thus some of the rotational energy is transformed into magnetic energy. We show that for magnetic fields $B \gtrsim 2 \times 10^{13}$ G, the combination of a strong magnetic field, and large spin period means the core field cannot be expelled by the vortices. When $B \lesssim 10^{13}$ G, the magnetic field is partially expelled from the core, which launches large scale Hall waves from the crust-core interface. However, these Hall waves are not strong enough to break the crust.

An outline of the paper is as follows. In Section 2.2 we present the evolution equations for the magnetic field in the crust, for magnetically induced elastic back-reaction of the crust, and for the magnetic field evolution in the core. In Section 2.3 we present our results, and in Section 2.4 we discuss observational implications. Numerical details and derivations of key equations are given in the Appendices.

2.2 Equations and Formalism

2.2.1 Magnetic Field Evolution in the Crust

The evolution of the magnetic field in the crust is governed by the equation

$$\frac{\partial \boldsymbol{B}}{\partial t} = \nabla \times (\boldsymbol{v} \times \boldsymbol{B}) - \nabla \times (\eta \nabla \times \boldsymbol{B}), \tag{2.1}$$

[[18], [19]] where the first term here represents advection of the field by the electron fluid with velocity field $\boldsymbol{v}$, and the second term represents Ohmic diffusion with diffusivity $\eta = c^2/4\pi\sigma$. Here σ is the electrical conductivity of the crust. In contrast to previous work, our model takes into account the velocity of the ion lattice, $\dot{\boldsymbol{\xi}}$. The velocity of the electron fluid is then given by

$$\boldsymbol{v} = \boldsymbol{v}_{\text{hall}} + \dot{\boldsymbol{\xi}}, \tag{2.2}$$

where $\boldsymbol{v}_{\text{hall}}$ is the Hall drift velocity,

$$\boldsymbol{v}_{\text{hall}} = -\frac{c}{4\pi n_e e} \nabla \times \boldsymbol{B}. \tag{2.3}$$

There are two contributions to $\dot{\boldsymbol{\xi}}$,

$$\dot{\boldsymbol{\xi}} = \dot{\boldsymbol{\xi}}_{\rm el} + \dot{\boldsymbol{\xi}}_{\rm pl}. \tag{2.4}$$

Here $\dot{\boldsymbol{\xi}}_{\rm el}$ is the elastic deformation, and $\dot{\boldsymbol{\xi}}_{\rm pl}$ is the plastic deformation. For now we neglect the plastic response of the crust, and content ourselves with the elastic deformation.

We now follow closely the formalism of [24]. In axisymmetry the magnetic field can decomposed into poloidal and toroidal components, and expressed in terms of the scalar functions Ψ and I. The magnetic field is written as a sum of poloidal ($\boldsymbol{B}_{\rm p}$) and toroidal ($\boldsymbol{B}_{\rm T}$) components

$$\boldsymbol{B} = \boldsymbol{B}_{\rm p} + \boldsymbol{B}_{\rm T} = \nabla\Psi \times \nabla\phi + I\nabla\phi, \tag{2.5}$$

where we work in spherical coordinates (r, θ, ϕ), and define $\nabla\phi \equiv \hat{e}_\phi / r \sin\theta$. The function Ψ is known as the flux function (identical in form to the Stokes stream function), since $2\pi\Psi(r, \theta)$ is the poloidal magnetic flux passing through the polar cap with radius r and opening angle θ. The function I has the interpretation that $cI(r, \theta)/2$ is the poloidal current passing through the same polar cap, and hence is often called the poloidal current function.

We now express the evolution Equation (2.1) in terms of the scalar functions Ψ and I as defined in Equation (2.5). Evolving fields in this formalism has the advantage of automatically preserving $\nabla \cdot \boldsymbol{B} = 0$ at all times, provided the scalar functions Ψ and I are differentiable. We begin by defining the quantity

$$\chi = \frac{c}{4\pi e n_e r^2 \sin^2\theta}, \tag{2.6}$$

as in [24]. We also write the toroidal current as

$$\boldsymbol{j}_T = \frac{c}{4\pi} \nabla \times \boldsymbol{B}_p = -\frac{c}{4\pi} \Delta^* \Psi \nabla\phi, \tag{2.7}$$

and the electron angular velocity as

$$\Omega_{\rm e} = \Omega_{\rm hall} + \Omega_{\rm el} = -\frac{j_T}{r_\perp n_e e} + \frac{v^\phi_{\rm el}}{r_\perp} = \chi \Delta^* \Psi + \frac{v^\phi_{\rm el}}{r_\perp}, \tag{2.8}$$

with $r_\perp \equiv r\sin\theta$ the cylindrical radius, and we have used the Grad-Shafranov operator,

$$\Delta^* = \frac{\partial^2}{\partial r^2} + \frac{\sin\theta}{r^2}\frac{\partial}{\partial\theta}\left(\frac{1}{\sin\theta}\frac{\partial}{\partial\theta}\right). \tag{2.9}$$

Using the above definitions, the Hall evolution equation reduces to the following two scalar equations, in terms of the poloidal and toroidal scalar functions

$$\frac{\partial\Psi}{\partial t} - r^2\sin^2\theta\chi(\nabla I\times\nabla\phi)\cdot\nabla\Psi = \frac{c^2}{4\pi\sigma}\Delta^*\Psi, \tag{2.10}$$

$$\frac{\partial I}{\partial t} + r^2\sin^2\theta[(\nabla\Omega_\mathrm{e}\times\nabla\phi)\cdot\nabla\Psi + I(\nabla\chi\times\nabla\phi)\cdot\nabla I] = \frac{c^2}{4\pi\sigma}\left(\Delta^* I - \frac{1}{\sigma}\nabla I\cdot\nabla\sigma\right). \tag{2.11}$$

These evolution equations are the same as those in [24], except for the addition of the elastic back-reaction velocity of the crust. We assume a neutron star radius of $r_* = 10$ km, and a crust thickness of 1 km, so that the crust-core interface is at radius $r_c = 9$ km. We use the electron density profile and electrical conductivity provided by [24] who take $n_e \propto z^4$, with z the depth into the crust, and $\sigma \propto n_e^{2/3}$, which is somewhere between the density scalings expected for phonon scattering and impurity scattering. The electron number density at the base of the crust is given as $n_e = 2.5\times10^{36}\mathrm{cm}^{-3}$. We do not include the upper crust with density $\rho < 10^{11}$ g cm^{-3} to avoid time step issues in the low density regions where the evolution is very fast. The electrical conductivity varies from $\sigma = 3.6\times10^{24}$ s^{-1} at the base of the crust, to $\sigma = 1.8\times10^{23}$ s^{-1} at the surface, which is appropriate for phonon scattering at $T \approx 2\times10^8$ K [24]. We can determine the characteristic timescales of evolution of the Hall and Ohmic terms, with L a characteristic length scale, taken to be the thickness of the crust (1 km) and n_e and σ evaluated at the base of the crust,

$$t_\mathrm{ohm} \sim \frac{4\pi\sigma L^2}{c^2} = 13.5\left(\frac{L}{1\mathrm{km}}\right)^2\left(\frac{\sigma}{3.6\times10^{24}\ \mathrm{s}^{-1}}\right)\mathrm{Myr}, \tag{2.12}$$

$$t_\mathrm{hall} \sim \frac{4\pi e L^2 n_e}{cB} = \frac{1.6}{B_{14}}\left(\frac{L}{1\mathrm{km}}\right)^2\left(\frac{n_e}{2.5\times10^{36}\ \mathrm{cm}^{-3}}\right)\mathrm{Myr} \tag{2.13}$$

where B_{14} is the magnetic field strength in units of 10^{14}G.

2.2.2 Matching the Crust Field to the Magnetosphere

In order to solve the evolution Equations (2.10) and (2.11) we need two boundary conditions, for I and Ψ at r_*, which may also be formulated as conditions on $\boldsymbol{B}(r_*, \theta)$. In this work we are considering a slow evolution of magnetic fields on timescales over which any episodic magnetospheric twists (magnetar activity) must be erased [80]. It is therefore reasonable to assume a vacuum magnetic field as the boundary condition at the surface, as was previously shown by [81], [82], and [25]. Demanding zero current means that $\nabla \times \boldsymbol{B} = 0$ outside the star. So we can write the vacuum field as

$$\boldsymbol{B} = \nabla V, \tag{2.14}$$

where V is a scalar function. We also assume that there is no surface current at r_* due to the finite electrical conductivity of the outer crust. Thus, the two boundary conditions express the continuity of the tangential components of the magnetic field B_ϕ, B_θ, at the surface, so that they match a vacuum solution outside the star:

(i) The continuity of B_ϕ implies for the crustal field $B_\phi(r_*, \theta) = 0$, since in any axisymmetric vacuum magnetosphere $B_\phi = (r \sin\theta)^{-1} \partial V / \partial \phi = 0$. This gives $I(r_*, \theta) = 0$.

(ii) The continuity of B_θ gives a condition on $\partial \Psi / \partial r = -r \sin\theta B_\theta$ — This boundary condition is formulated below (no boundary condition is imposed on the values of $\Psi(r_*, \theta)$ – its evolution is calculated from Equation (2.10) in the crust).

The constraint $\nabla \cdot \boldsymbol{B} = 0$, gives the Laplace equation for V, $\nabla^2 V = 0$. B_θ is determined by this Laplace equation outside the star for given surface values of B_r. Because $V \longrightarrow 0$ as $r \longrightarrow \infty$, we can write the solution as a multipolar expansion. For axisymmetric magnetic fields V is given by

$$V(r, \theta) = \sum_{l=1}^{\infty} \frac{a_l}{r^{l+1}} P_l(\cos\theta), \tag{2.15}$$

where $P_l(\cos\theta)$ are the Legendre polynomials. The sum starts at $l = 1$ because there are no magnetic monopoles, and a_l are expansion coefficients to be determined. Now using the definition of the magnetic field in Equation (2.14), we can write

$$B_r(r,\theta) = \frac{\partial V}{\partial r} = -\sum_{l=1}^{\infty}(l+1)\frac{a_l}{r^{l+2}}P_l(\cos\theta). \tag{2.16}$$

We can invert this expression to solve for the expansion coefficients, and evaluate it at r_* which gives

$$a_l = -r_*^{l+2}\frac{2l+1}{2l+2}\int_0^{\pi} P_l(\cos\theta)B_r(r_*,\theta)\sin\theta d\theta. \tag{2.17}$$

Using these expansion coefficients, we can calculate B_θ using Equation (2.5),

$$B_\theta(r,\theta) = \frac{1}{r}\frac{\partial V}{\partial\theta} = \sum_{l=1}^{\infty}\frac{a_l}{r^{l+2}}\frac{dP_l(\cos\theta)}{d\theta} = -\frac{1}{r\sin\theta}\frac{\partial\Psi}{\partial r}. \tag{2.18}$$

This gives the boundary condition for Ψ on the surface of the star as

$$\left.\frac{\partial\Psi}{\partial r}\right|_{r_*} = -\sin\theta\sum_{l=1}^{\infty}\frac{a_l}{r_*^{l+1}}\frac{dP_l(\cos\theta)}{d\theta}. \tag{2.19}$$

2.2.3 Magneto-elastic Evolution of the Crust

The elastic response of the neutron star crust to magnetic stress is governed by the elastodynamic wave equation, with an external Lorentz driving force. We begin by defining the Lagrangian displacement field of the neutron star crust as

$$\boldsymbol{\xi}(\boldsymbol{r},t) \equiv \boldsymbol{r'} - \boldsymbol{r}, \tag{2.20}$$

where $\boldsymbol{r}$ is the position of a point in the crust before deformation, and $\boldsymbol{r'}$ is the position of that point after the deformation. The elastodynamic wave equation can be derived from Newton's second law. We restrict ourselves to the regime of linear elastodynamics and only consider small, reversible deformations of the crust. In this framework the stress depends linearly on the displacement, and we may express the stress as the sum of elastic stress tensor using Hooke's Law, and the magnetic stress using the magnetic part of the Maxwell tensor. It has been shown that the speed at which shear waves propagate in a neutron star crust is remarkably constant over its depth [83]. We work in the approximation that shear waves propagate at constant speed [$v_{\rm sh} \approx 10^8$ cm s^{-1}, [83], [84]] throughout the crust, and also that they propagate at the same speed in all directions (isotropic). We estimate the shear modulus as

$$\mu = \rho v_{\rm sh}^2 \approx 10^{28} \rho_{12} \text{ erg cm}^{-3}, \tag{2.21}$$

where we assume the mass density scaling $\rho \propto z^8$. Specifically, we chose $\rho_{12} = 0.5[(1.1 r_* - r)/0.1 r_*]^8$, which varies from $\rho = 1.3 \times 10^{14}$ g cm^{-3} at the base of the crust, to $\rho = 5 \times 10^{11}$ g cm^{-3}, our chosen surface cutoff. Additionally, assuming an incompressible crust ($\nabla \cdot \boldsymbol{\xi} = 0$), and a spherically symmetric unevolving shear modulus $\mu(r)$ yields the elastodynamic wave equation

$$\rho \frac{\partial^2 \boldsymbol{\xi}}{\partial t^2} = (\nabla \mu \cdot \nabla) \boldsymbol{\xi} - (\boldsymbol{\xi} \cdot \nabla) \nabla \mu + \mu \nabla^2 \boldsymbol{\xi} + \frac{1}{4\pi} (\nabla \times \boldsymbol{B}) \times \boldsymbol{B}. \tag{2.22}$$

The term on the left-hand side (LHS) of Equation (2.22) is due to the inertia of the crust. Since Hall drift occurs on timescales much longer than the elastic wave crossing time, we may neglect the inertial term in these models. The first three terms on the right-hand side (RHS) of Equation (2.22) are due to the elastic restoring forces of the solid crust, and the last term is due to Maxwell stresses. With the neglect of the inertial term, magneto-elastic equilibrium is given by

$$\frac{1}{4\pi} (\nabla \times \boldsymbol{B}) \times \boldsymbol{B} = -(\nabla \mu \cdot \nabla) \boldsymbol{\xi} + (\boldsymbol{\xi} \cdot \nabla) \nabla \mu - \mu \nabla^2 \boldsymbol{\xi}. \tag{2.23}$$

We, however, prefer to deal with an evolution (rather than the above constraint) equation for ξ and therefore introduce a small non-zero velocity

$$\boldsymbol{v}_{\rm el} \equiv \frac{\partial \boldsymbol{\xi}}{\partial t}. \tag{2.24}$$

It corresponds to a small deviation from the force balance that we write in a relaxation/damping form $\boldsymbol{f}_{\rm damp} = -\gamma\rho\boldsymbol{v}_{\rm el}$. The value of γ is not important as long as it is small enough, so that the system evolves very close to the force balance. Effectively, this is a dynamic way of implementing the constraint on ξ required by the force balance. This yields the evolution equation,

$$\frac{\partial \boldsymbol{\xi}}{\partial t} = \frac{1}{\gamma\rho}\left[(\nabla\mu\cdot\nabla)\boldsymbol{\xi} - (\boldsymbol{\xi}\cdot\nabla)\nabla\mu + \mu\nabla^2\boldsymbol{\xi}\right] + \frac{1}{4\pi\gamma\rho}(\nabla\times\boldsymbol{B})\times\boldsymbol{B}, \tag{2.25}$$

which when evolved in the limit of small γ will tend toward the adiabatic solution. This relaxation method is equivalent to solving a matrix problem to find ξ, but avoids the difficulty of equations which are implicit in the evolution of $\boldsymbol{B}$. The challenge in choosing the value of γ is on the one hand to ensure the relaxation is fast enough so that the crust is in equilibrium between the magnetic and elastic forces, but on the other hand is slow enough so that the numerical computations do not become too costly. It is helpful to consider the characteristic relaxation timescale

$$t_{\rm re} = \gamma\frac{L^2}{v_{\rm sh}^2}, \tag{2.26}$$

and require $t_{\rm re} \ll t_{\rm hall}$. This gives the criterion

$$\gamma \ll \frac{4\pi n_e e}{B}v_{\rm sh}^2. \tag{2.27}$$

The back reaction of the crustal motion on the evolution of the magnetic field occurs through the equation

$$\frac{\partial \boldsymbol{B}}{\partial t} = \nabla\times[(\boldsymbol{v}_{\rm hall}+\boldsymbol{v}_{\rm el})\times\boldsymbol{B}] - \nabla\times(\eta\nabla\times\boldsymbol{B}), \tag{2.28}$$

as shown in the previous section.

2.2.4 Magnetic Field Evolution in the Core

There are a number of proposed mechanisms which can transport magnetic flux in neutron star cores, and may lead to an understanding of numerous observable phenomena. Below we outline each of the effects we implement in our numerical scheme, motivate the equations of motion, and discuss the relevant timescales of evolution. We assume a simplified model for the core consisting of protons, neutrons and electrons. We also assume that the neutrons are superfluid, and the protons exist in a type-II superconducting state [85]. Observations of the Cas A remnant indicate that the core is likely to be superfluid and superconducting ≈ 300 yr after birth, and at a temperature $7 - 9 \times 10^8$ K (greater than the temperatures we consider in our models) [86, 87]. Hence, the physics of the phase transition itself may be safely neglected in this work.

Hydromagnetic equilibrium

In this section we outline two methods for studying the evolution of neutron star core magnetic fields on long (Hall) timescales, while maintaining stability on dynamical (MHD) timescales, and taking into account fluid degrees of freedom. The core has a very high conductivity and we treat it as an ideal conductor, so that the field is perfectly coupled to the fluid. It is then instructive to consider displacements of the fluid, since these correspond directly to degrees of freedom of the field. Firstly we assume there is no bulk fluid displacement in the radial direction $\xi_r = 0$ on the Alfvén timescale, and that the core is incompressible, which in axisymmetry implies $\xi_\theta = 0$. In this axisymmetric model, the core fluid can only be displaced in the azimuthal direction, which corresponds to the motion of fluid elements on spherical shells, at fixed cylindrical radius. Such displacements in the ϕ direction do not perturb the local pressure or chemical potential, and are only limited by the viscosity of the fluid which is negligible. Thus, it is a good approximation to assume that any toroidal flux injected into the core, readily distributes itself according to a tension equilibrium along poloidal field lines. In axisymmetry this corresponds to $f_\phi = \boldsymbol{j}_p \times \boldsymbol{B}_p / c = 0$, but in general it is the vanishing of the solenoidal part of the Lorentz force. In terms of the scalar functions I and Ψ, this condition is equivalent to

$$I = I(\Psi), \tag{2.29}$$

which means that I is constant along poloidal field lines in the core. We present two methods enforcing this condition. We briefly outline the first method here, leaving the details for Appendix A. The second method is more general, and we discuss it in more detail.

Firstly, it is possible to determine the value of I along a given poloidal field line in the core by calculating the advection flux of B_ϕ into the core by Hall drift. The advection flux of B_ϕ is defined by writing the Hall evolution equation for B_ϕ in the crust in conservative form, and identifying the advection flux. In this method it is convenient to work in the so-called flux-coordinates (Ψ, λ, ϕ), where Ψ labels surfaces of constant poloidal flux, and λ is the length along a given poloidal field line in the $\phi = const$ plane [e.g. [88]]. It can be shown (Appendix A), that the twist angle ζ of a given poloidal field line in the core evolves according to the equation

$$\frac{\partial \zeta(\Psi)}{\partial t} = -[J(\Psi, \lambda_2, t) - J(\Psi, \lambda_1, t)], \tag{2.30}$$

where we have identified the twist angle

$$\zeta(\Psi) = \int_{\lambda_1}^{\lambda_2} d\lambda \left(\frac{B_\phi}{r_\perp B_\lambda} \right), \tag{2.31}$$

with the integral taken along the magnetic field line ($\Psi = \text{const}$). J is related to the “flux of twist" into the core through

$$F = r_\perp B_\lambda J = v_\lambda B_\phi - v_\phi B_\lambda. \tag{2.32}$$

The RHS of Equation (2.30) represents the difference between flux of twist at each footpoint of a field line threading the core at its boundary. There are two contributions to the flux of twist J. The first term can be attributed to Hall drift advecting B_ϕ into the core with poloidal drift currents, and the second term is the azimuthal winding of poloidal field lines by Hall drift. Equation (2.30) may be rearranged to obtain the following equation for the evolution of $I(\Psi)$,

$$\frac{\partial I(\Psi, t)}{\partial t} = -\varpi(\Psi)[J(\Psi, \lambda_2, t) - J(\Psi, \lambda_1, t)], \tag{2.33}$$

with

$$\varpi(\Psi) = \left(\int_{\lambda_1}^{\lambda_2} \frac{d\lambda}{r_\perp^2 B_\lambda}\right)^{-1}. \tag{2.34}$$

If the toroidal field displays equatorial plane reflection symmetry, and the poloidal field displays equatorial symmetry, $J(\Psi, \lambda_1, t) = J(\Psi, \lambda_2, t)$, and there will be no magnetic twist injected into the core.

The procedure outlined above is efficient in tracing the crust-core evolution of the field, so long as the poloidal magnetic field lines in the core are fixed in time. However, in our studies we would like to have the freedom to evolve the core poloidal field. In such situations, it is more practical to use the second method outlined below.

The second method of enforcing hydromagnetic equilibrium, is to treat it as a relaxation problem. This method has the advantage of not requiring the integral in Equation (2.34) to be evaluated. The principle of the method is similar to that used in Section 2.2.3 for computing the elastic response of the crust. Suppose there is a poloidal field threading the core. Hall drift in the crust will slowly displace the magnetic field lines in the azimuthal direction, and in response to this, the core field will adjust, quickly returning to hydromagnetic equilibrium. The evolution of the core field can be written

$$\frac{\partial \boldsymbol{B}_{\mathbf{T}}}{\partial t} = \nabla \times (\boldsymbol{v}_{\mathrm{T}} \times \boldsymbol{B}_{\mathrm{p}} + \boldsymbol{v}_{\mathrm{p}} \times \boldsymbol{B}_{\mathrm{T}}), \tag{2.35}$$

with $\boldsymbol{v}_{\mathrm{T}}$ the toroidal (azimuthal) velocity which returns the core field to hydromagnetic equilibrium. The second term on the RHS is the advection of the toroidal field with the poloidal drift velocity $\boldsymbol{v}_{\mathrm{p}}$, of flux surfaces. This term ensures that each poloidal field line maintains its own twist angle when the flux surfaces are evolving. For a given (fixed) poloidal field configuration, equilibrium is satisfied when

$$\frac{\partial \boldsymbol{B}_{\mathbf{T}}}{\partial t} = 0 \quad \text{(equilibrium)}. \tag{2.36}$$

Thus all that is required, is to choose a convenient form of $\boldsymbol{v}_{\mathrm{T}}$ which drives the field towards equilibrium faster than the other channels of evolution, such as Hall drift. First though, we write Equation (2.35) in a more convenient form. It can be shown that Equation (2.35) may be written as

$$\frac{\partial B_\phi}{\partial t} + \nabla_{\mathrm{p}} \cdot (\boldsymbol{v}_{\mathrm{p}} B_\phi) = \nabla_{\mathrm{p}} \cdot (v_\phi \boldsymbol{B}_{\mathrm{p}}), \tag{2.37}$$

where we have defined the poloidal differential operator

$$\nabla_{\mathrm{p}} \equiv \left(\frac{\partial}{\partial r_\perp}, \frac{\partial}{\partial z} \right), \tag{2.38}$$

which acts in the 2D plane. Equation (2.37) is easily interpreted as a continuity equation, with the second term on the LHS the divergence of a transport flux of B_ϕ due to drift of the poloidal field. The term on the RHS is a source term, which injects or extracts B_ϕ (and magnetic twist) from the magnetic field lines which enter the crust. When using this method $\boldsymbol{v}_{\mathrm{p}}$ must be the same as the poloidal drift velocity of flux surfaces in the core. While in this paper we only use this method for the case of fixed poloidal field lines in the core ($\boldsymbol{v}_{\mathrm{p}} = 0$), the method is also applicable to the case of non-zero $\boldsymbol{v}_{\mathrm{p}}$, which we discuss later. For the simplified case of $\boldsymbol{v}_{\mathrm{p}} = 0$ though, the second term on the LHS of Equation (2.37) vanishes. Then, all that remains is to choose a convenient form of v_ϕ which will drive the field toward equilibrium. We find that such a form is

$$v_\phi = \frac{k}{|\boldsymbol{B}_{\mathrm{p}}|} (\nabla I \cdot \hat{\boldsymbol{e}}_\lambda), \tag{2.39}$$

which obviously tends to zero as the field is driven toward equilibrium. Here k is a relaxation parameter to be be tuned. For the case of static poloidal fields in the core ($\boldsymbol{v}_{\mathrm{p}} = 0$), Equation (2.37) becomes

$$\frac{\partial I}{\partial t} = r_\perp \nabla_{\mathrm{p}} \cdot [k(\nabla I \cdot \hat{\boldsymbol{e}}_\lambda) \hat{\boldsymbol{e}}_\lambda], \tag{2.40}$$

which has the form of a modified diffusion equation. It is convenient to work with this form of the equation, since diffusion equations are less problematic to solve numerically. Equation (2.40) with a large k ensures that the magnetic field in the core evolves through a sequence of MHD equilibria, and that these equilibria are stable.

In the more general case, poloidal magnetic field lines are not fixed in the core, but can drift with Ambipolar diffusion, or Jones drift for example.

For illustrative purposes we determine the Ohmic drift velocity of poloidal field lines by noting that the electric field determines $\partial \boldsymbol{B}/\partial t = -c\nabla \times \boldsymbol{E}$. If we assume that $\boldsymbol{v}$ is perpendicular to $\boldsymbol{B}$, one may rewrite the evolution equation as $\partial \boldsymbol{B}/\partial t = \nabla \times (\boldsymbol{v} \times \boldsymbol{B})$ with $\boldsymbol{v}$ defined by $\boldsymbol{E} = -\boldsymbol{v} \times \boldsymbol{B}/c$. Using Ohm's law, for the case of poloidal fields this becomes

$$\frac{\boldsymbol{J}_{\mathrm{T}}}{\sigma} = \frac{c}{4\pi\sigma}\nabla \times \boldsymbol{B}_{\mathrm{p}} = -\frac{1}{c}\boldsymbol{v}_{\mathrm{p}} \times \boldsymbol{B}_{\mathrm{p}}, \tag{2.41}$$

with $\boldsymbol{v}_{\mathrm{p}}$ the poloidal velocity. Taking the cross product of both sides with $\boldsymbol{B}_{\mathrm{p}}$ allows us to solve for $\boldsymbol{v}_{\mathrm{p}}$. This is the velocity at which poloidal magnetic field lines drift due to Ohmic diffusion, and we call it $\boldsymbol{v}_{\mathrm{ohm}}$,

$$\boldsymbol{v}_{\mathrm{ohm}} = \frac{c^2}{4\pi\sigma}\frac{[(\nabla \times \boldsymbol{B}_{\mathrm{p}}) \times \boldsymbol{B}_{\mathrm{p}}]}{(\boldsymbol{B}_{\mathrm{p}} \cdot \boldsymbol{B}_{\mathrm{p}})}. \tag{2.42}$$

When this velocity is inserted into an induction equation it is exactly equivalent to the Ohmic diffusion equation, so this is indeed the correct Ohmic diffusion velocity.

We note here that a number of previous works fail to include the correct hydromagnetic equilibrium in the core, rendering their boundary condition on the crust-core interface unphysical. [89] violate equatorial plane reflection symmetry, and therefore effectively must be injecting magnetic twist into the core within the timescale of their simulation. The simulations of [79] include strong toroidal fields in the core, which in general do not satisfy $f_\phi = 0$. These stresses cannot be supported by the fluid, and therefore these simulations violate hydromagnetic equilibrium. This error in [79] is due to their lack of the terms which advect magnetic field by an azimuthal fluid motion; in other words, the background in which their flux tubes move is assumed to be static.

Jones flux tube drift

In newborn neutron stars the magnetic field undergoes a period of dynamically unstable evolution before settling into a stable configuration in which the stresses of the field, given by the Maxwell stress tensor, are balanced by the fluid degrees of freedom. Many Alfvén crossing times later, the crust solidifies, and cooling of the core below $T_{\rm crit} \approx 10^8 - 10^9$ K is accompanied by Cooper pairing of protons to form a ${}^1S_0$ superfluid (eg., [27]). The phase transition to superconductivity is associated with the quantization of magnetic flux on microscopic scales, with the quantum of flux $\phi_0 = hc/2e$. The flux is localised within proton supercurrent vortices, and drops off exponentially on the penetration-depth scale $\lambda \lesssim 10^{-11}$ cm. The mean intervortex spacing is $d = 5 \times 10^{-10}\, B_{12}^{-1/2}$cm, greater than the penetration depth λ, so that the flux tubes are very weakly interacting. [90] realized that the anisotropic component of the magnetic stress tensor in type-II superconductors can be significantly larger than $B^2/4\pi$. [91] showed that in the limit of $B < H_{c1}$, with $H_{c1} \approx 10^{15}$ G the lower critical limit, the stress tensor is given as

$$\sigma_{ij} = P_{\rm matter}\delta_{ij} + \frac{H_i B_j}{4\pi}, \tag{2.43}$$

where H_i are the components of vector $\mathbf{H}$. Matter contributes the isotropic component of σ_{ij}, and accounts for the buoyancy of flux tubes; it will be neglected below. As expected the magnetic contribution to the isotropic component is suppressed, due to the lack of magnetic pressure between neighbouring flux tubes. Taking the divergence of this stress tensor gives the volume force

$$\boldsymbol{f}_B = \frac{1}{4\pi}(\boldsymbol{B} \cdot \nabla)\boldsymbol{H}_{\rm c1}, \tag{2.44}$$

where we have assumed $H \approx H_{c1}$. Note that $\boldsymbol{H}_{c1}$ and $\boldsymbol{B}$ are locally parallel vectors, and $\boldsymbol{B}$ is the spatial average of the microscopic magnetic field. The flux tubes drift with velocity $\boldsymbol{v}_L$ through the core fluid, driven by the tension force of the flux localised within the tubes $\boldsymbol{f}_B$. A simple estimate of the buoyancy force discussed by [92] indicates that it is often smaller than the tension force

Equation (2.44) for typical configurations. Therefore, in this work we do not consider magnetic buoyancy, and neglect the term $P_{\rm matter}\delta_{ij}$ in Equation (2.43). The drift velocity is defined by considering the balance of forces on the fluid in the vicinity of a flux tube. We follow [8], who writes the force balance as

$$\boldsymbol{f}_B - \frac{(n_e e)^2}{\tilde{\sigma}}(\boldsymbol{v}_L - \boldsymbol{v}_e) - \frac{n_e e}{c}(\boldsymbol{v}_L - \boldsymbol{v}_e) \times \boldsymbol{B} - \frac{n_p e}{c}(\boldsymbol{v}_{p0} - \boldsymbol{v}_L) \times \boldsymbol{B} = 0, \tag{2.45}$$

with n_e and n_p the electron and proton density, $\tilde{\sigma}$ an effective electron conductivity in the superconductor[1] and $\boldsymbol{v}_e$ and $\boldsymbol{v}_{p0}$ the macroscopic electron and proton drift velocities respectively. [28] derives each of the terms in Equation (2.45). The second term on the LHS of Equation (2.45) is due to drag from scattering of electrons on quasi-particles localised in the flux tube core, the third term is the Lorentz force on the electrons, and the fourth term is the Magnus force, due to motion of the flux tube through the superfluid protons.

In a multifluid type-II superconductor, macroscopic currents due to relative motion between charged species are suppressed, and the electrons and protons are co-moving on large scales. This can be expressed with the charge current screening condition of [28],

$$\boldsymbol{J}^e + \boldsymbol{J}^p = 0, \tag{2.46}$$

where $\boldsymbol{J}^e$ is the electron current density, and $\boldsymbol{J}^p$ the proton supercurrent density. This ensures satisfaction of Amperes law, and the London equation throughout the superconductor. For the purposes of this work we neglect entrainment, and using $\boldsymbol{J}^e = -n_e e \boldsymbol{v}_e$, and $\boldsymbol{J}^p = n_p e \boldsymbol{v}_{p0}$, it is easy to see that

$$n_e \boldsymbol{v}_e = n_p \boldsymbol{v}_{p0}. \tag{2.47}$$

Implementing this screening condition, and assuming charge neutrality ($n_e = n_p$) leads to cancellation of the Magnus and Lorentz forces, and the drift velocity of flux tubes is given by the expression

---

[1] Note that $\tilde{\sigma}$ has the same mathematical form as σ [e.g. [85]]. The key difference as noted by [28], is that the electron transport relaxation time is modified when the scattering sites are localised within flux tubes [confusingly, [28] denotes $\tilde{\sigma}$ by σ]. Therefore $\tilde{\sigma}$ is a different quantity to σ in normal matter.

$$\boldsymbol{v}_L = \boldsymbol{v}_e + \frac{\tilde{\sigma}}{n_e^2 e^2} \boldsymbol{f}_B. \tag{2.48}$$

The flux tube velocity has two contributions – the motion of flux tubes with the charged fluid, and the motion of flux tubes through the charged fluid. Here $\boldsymbol{v}_e$, represents motion of flux tubes with the charged plasma (what is usually referred to as ambipolar diffusion). Motion of the flux tubes faster than the background charged plasma occurs with the Jones velocity

$$\boldsymbol{v}_\mathrm{J} = \frac{\alpha}{4\pi} (\boldsymbol{B} \cdot \nabla) \boldsymbol{H}_\mathrm{c1}, \quad \alpha = \tilde{\sigma} / n_e^2 e^2, \tag{2.49}$$

and is accompanied by dissipation at the rate $\boldsymbol{v}_\mathrm{J} \cdot \boldsymbol{f}_B$ – here α is an effective drag coefficient. It is important to note that the transport velocity of flux can be significantly larger than the plasma drift velocity (ambipolar velocity), which tends to be slowed by the formation of sharp pressure gradients in typical cases. In this work we neglect the velocity $\boldsymbol{v}_e$ (ambipolar diffusion), and consider only the Jones drift velocity (ie. we set $\boldsymbol{v}_L = \boldsymbol{v}_\mathrm{J}$). It was recently shown by [93] that ambipolar diffusion in superfluid neutron stars can be significant for solenoidal flows at low temperatures ($T < 10^9$ K). The detailed consideration of ambipolar diffusion is outside of the scope of this work.

It is important to note that this drift velocity is very different to that of [94], [95], and [79]. This can be traced to differences in the calculation of forces acting on a flux tube by [94] (private communication). Clarifying this difference requires a separate investigation and is outside of the scope of this work. It should be noted that the force balance (2.45) is non-trivial, and careful calculation is required to determine these forces (see [96] and [28]).

In a type-II superconductor the motion of flux tubes with velocity $\boldsymbol{v}_L$ induces an electric field localized within the vortex cores (see eg. [8, 96, 97]). The spatial average of this electric field is

$$\boldsymbol{E} = -\frac{1}{c} \boldsymbol{v}_L \times \boldsymbol{B}, \tag{2.50}$$

which upon substitution into Faraday's law, leads to the following evolution equation for the poloidal part of the spatially averaged field,

$$\frac{\partial \boldsymbol{B}_{\rm p}}{\partial t} = \nabla \times (\boldsymbol{v}_L \times \boldsymbol{B}_{\rm p}), \tag{2.51}$$

while the evolution of the toroidal field on comparable timescales is such that it satisfies hydromagnetic equilibrium at all times. Equation (2.51) is very different from the evolution equation used by [79] (see their equation 16). Firstly, as pointed out by [92], the magnetic field is locked into flux tubes, and therefore, the evolution of the magnetic field must be governed by an advection equation of the form Equation (2.51), where the field is advected at the same velocity as the flux tubes, $\boldsymbol{v}_L$. However the evolution equation of [79] does not advect the magnetic field at the velocity $\boldsymbol{v}_L$.

As in Section 2.2.1 we write the evolution equation in terms of the scalar functions Ψ and I,

$$\frac{\partial \Psi}{\partial t} + \boldsymbol{v}_{\rm J} \cdot \nabla \Psi = 0, \tag{2.52}$$

while I satisfies Equation (2.33). [8] estimates $\tilde{\sigma} \approx 10^{29} - 10^{32} B_{12}^{-1}$ s^{-1}, depending on the composition of the core. We use in our simulations $\tilde{\sigma} = 10^{29} B_{12}^{-1}$ s^{-1}. For a $1.4 M_{\odot}$ neutron star, a typical baryon density at the centre of the core is $n_B \approx 3.5 \times 10^{38}$ cm^{-3} [98]. We take a central electron fraction $Y_e = 0.1$, which gives $n_e = Y_e n_B = 3.5 \times 10^{37}$ cm^{-3}. Rather than adopt a particular equation of state we use these conservative values to calculate α throughout the core, which will cause the field evolution to be slower in the outer core in our simulations. But for our purposes we want to understand the dynamics of flux tubes on long timescales, and this will not affect the end state of our simulations.

Flux transport by neutron vortices

In conventional neutron star models, neutrons in the core form cooper pairs, and exist in a $^3P_2$ superfluid state [27]. The vorticity of the bulk fluid must be zero, and circulation is quantized

Table 2.1: Summary of the models we discuss in Section 2.3. Here HME (relaxation) implies hydromagnetic equilibrium enforced by the relaxation method in Section 2.2.4. HME (trivial) is for symmetric configurations where the toroidal field remains zero in the core according to hydromagnetic equilibrium.

Model	Crust Evolution	Core Poloidal Evolution	Core Toroidal Evolution	$\lvert\boldsymbol{B}\rvert_{\max}$ (initial)	Section
A	Hall + Ohmic	Fixed	HME (Relaxation)	2.2×10^{14} G	Section 2.3.1
B	Hall + Ohmic	Jones drift only	HME (Trivial)	2.2×10^{14} G	Section 2.3.2
C	Ohmic	Jones drift only	HME (Trivial)	2×10^{12} G	Section 2.3.2
D1	Hall + Ohmic	Jones drift + Vortex-transport	HME (Trivial)	6.9×10^{12} G	Section 2.3.3
D2	Hall + Ohmic	Jones drift + Vortex-transport	HME (Trivial)	1.4×10^{13} G	Section 2.3.3
D3	Hall + Ohmic	Jones drift + Vortex-transport	HME (Trivial)	2.7×10^{13} G	Section 2.3.3
E	Hall + Ohmic + Elastic	Fixed	HME (Trivial)	2×10^{14} G	Section 2.3.4

on microscopic scales with the formation of superfluid vortices. The vortices each possess the quantum of circulation $\kappa = h/2m_n$, where h is the Planck constant and $2m_n$ is the effective mass of a cooper pair. The mean number density of vortices is

$$n_v = \frac{2\Omega_n}{\kappa}, \tag{2.53}$$

where Ω_n is the superfluid rotational frequency. The neutron vortices are not necessarily straight, though the absence of a firm detection of free precession seems to indicate that the vortex configuration is not radically different from a linear array.

Stellar spin-down must be accompanied by motion of these vortices outward, in order to conserve angular momentum [29]. Likewise spinning up the star must be accompanied by motion of the neutron vortices inward. The neutron vortices move in the radial direction with velocity

$$\boldsymbol{v}_\perp = -\frac{r_\perp \dot{\Omega}_n}{2\Omega_n}\hat{\boldsymbol{e}}_{r_\perp}. \tag{2.54}$$

As a consequence of the neutron superfluid coupling to the proton superfluid, protons also circulate around the neutron vortices, which produces a magnetization localized within the penetration depth $\lambda \lesssim 10^{-11}$ cm of the neutron vortex core [see eg. [28]]. Outward moving neutron vortices interact strongly with flux tubes, and thus the spin-down of neutron stars can result in the transport of magnetic flux tubes [30]. According to [7], force builds up on the flux tubes, which are either carried along with the neutron vortices, or are cut through by them. [8] states that in order for straight flux tubes to be pushed along by neutron vortices (with velocity $\boldsymbol{v}_\perp$), the maximum velocity of the flux tubes (due to viscous drag) must be greater than or equal to the velocity of the neutron vortices, $|\boldsymbol{v}_F| \geq |\boldsymbol{v}_\perp|$. If this inequality is not satisfied, the neutron vortices will cut through the flux tubes. [8] gives the maximum velocity of flux tubes being pushed on by neutron vortices as

$$\boldsymbol{v}_F = \alpha n_v \tilde{f}_v \hat{\boldsymbol{e}}_{r_\perp}, \tag{2.55}$$

where α is the drag coefficient defined in Equation (2.49), and $\tilde{f}_v$ is the maximum force per unit length a neutron vortex can exert on a flux tube without cutting through. We estimate $\tilde{f}_v$ by using the vortex-flux tube interaction energy of [99][2]. Following [7] we assume that as a vortex moves along and collects flux tubes, the separation between flux tubes approaches 2λ. This gives

$$\tilde{f}_v = \frac{\phi_0 \phi_0^*}{8\pi^2 \lambda^3} \ln\left(\frac{\lambda}{\xi_p}\right) \approx 3.8 \times 10^{17} \text{ dyne/cm}, \tag{2.56}$$

with ϕ_0^* the flux quantum of a neutron vortex (we approximate $\phi_0 \approx \phi_0^*$), and ξ_p the proton coherence length.

We extend the treatment of [8] and [7] to the case of curved flux tubes, by including the self-tension force $\boldsymbol{f}_B$, and also discuss the transport of flux tubes in the cut-through regime. We say that cut-through occurs when

$$\left| -\frac{\boldsymbol{v}_\perp}{\alpha} \cdot \hat{\boldsymbol{e}}_{r_\perp} + \boldsymbol{f}_{\boldsymbol{B}} \cdot \hat{\boldsymbol{e}}_{r_\perp} \right| \geq n_v \tilde{f}_v, \tag{2.57}$$

with $-\boldsymbol{v}_\perp \cdot \hat{\boldsymbol{e}}_{r_\perp}/\alpha$ the drag force the flux tubes exert on the neutron vortices (assuming a stationary background fluid), $\boldsymbol{f}_{\boldsymbol{B}} \cdot \hat{\boldsymbol{e}}_{r_\perp}$ the tension force flux tubes exert on the vertical vortices, and $n_v \tilde{f}_v$ the maximum force per unit volume the neutron vortices can exert on the flux tubes. We call satisfaction of the above inequality “cut-through", and dissatisfaction of the inequality “vortex-transport".

In the transport regime, the flux tubes are carried along with velocity $\boldsymbol{v}_\perp$. But the flux tubes also have the freedom to slide along the neutron vortices, with the projected Jones drift velocity $(\boldsymbol{v}_\mathrm{J} \cdot \hat{\boldsymbol{e}}_n)\hat{\boldsymbol{e}}_n$. Here $\hat{\boldsymbol{e}}_n$ is a unit vector which points along the local direction of a vortex.

In the cut-through regime, we assume that the flux tubes are still carried along by the neutron vortices, but only at the terminal velocity $\boldsymbol{v}_F$. Since the vortices cannot prevent the motion of flux tubes in the cut-through regime, the flux tubes can also drift in accordance with their own self tension (the Jones drift velocity $\boldsymbol{v}_\mathrm{J}$). To summarize the flux tubes are advected with the velocity field

---

[2] These authors have corrected a typo in the interaction energy of [7] which erroneously leads to a factor of π^2 larger pinning energies.

$$\boldsymbol{v}_{\mathbf{sd}} = \begin{cases} \boldsymbol{v}_{\perp} + (\boldsymbol{v}_{\mathrm{J}} \cdot \hat{\boldsymbol{e}}_n)\hat{\boldsymbol{e}}_n, & \text{(vortex-transport)} \\ \boldsymbol{v}_F + \boldsymbol{v}_{\mathrm{J}}, & \text{(cut-through)} \end{cases} \tag{2.58}$$

while the neutron vortices move with velocity $\boldsymbol{v}_{\perp}$. We note here that the velocity field given by Equation (2.58) is in fact a piece-wise continuous function. This can be understood by noting that if the LHS of Equation (2.57) is slightly greater than the RHS, then the velocity there is set to $\boldsymbol{v}_F + \boldsymbol{v}_{\mathrm{J}}$, so that a discontinuity never develops. See [7] for a similar model of vortex transport in 1D for the case of straight flux tubes.

We assume that the neutron vortex array is not significantly deformed by the flux tubes. This is true for high spin frequencies, when the neutron magnus force is larger than the critical cut-through force

$$\Omega > \frac{\tilde{f}_v}{r_{\perp}\rho_n\kappa}. \tag{2.59}$$

The evolution of the magnetic field due to motion of neutron vortices is given by

$$\frac{\partial \boldsymbol{B}_{\mathrm{p}}}{\partial t} = \nabla \times (\boldsymbol{v}_{\mathrm{sd}} \times \boldsymbol{B}_{\mathrm{p}}). \tag{2.60}$$

In terms of the scalar function Ψ, the evolution is

$$\frac{\partial \Psi}{\partial t} + \boldsymbol{v}_{\mathrm{sd}} \cdot \nabla\Psi = 0, \tag{2.61}$$

while the toroidal field evolves according to hydromagnetic equilibrium.

2.3 Results

The equations describing the magnetic field evolution in the star, i.e. the evolution equations for functions $\Psi(r,\theta)$ and $I(r,\theta)$, are discretized on a grid and solved numerically as described in Appendix B.

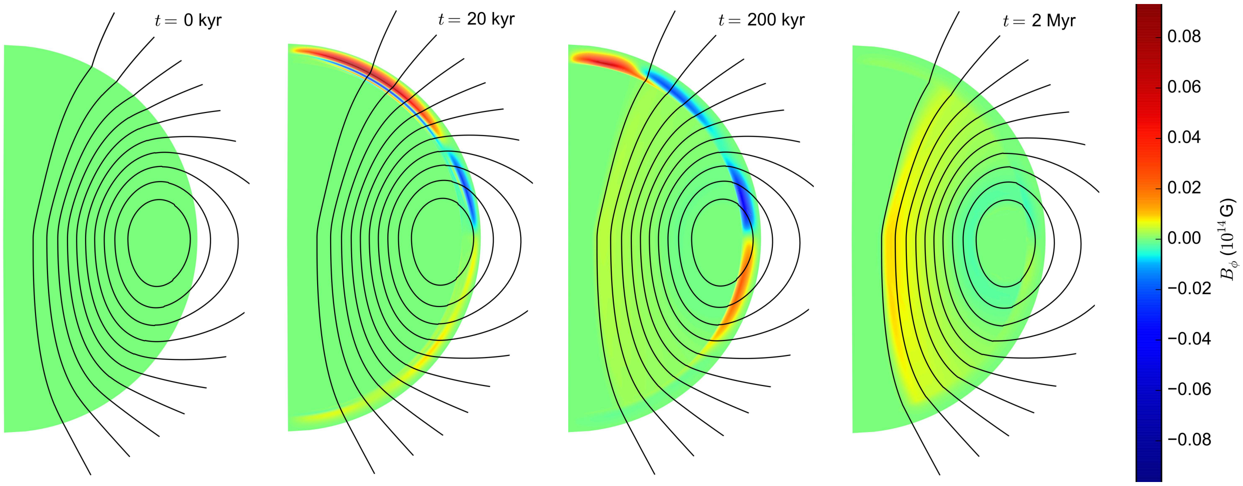

Figure 2.1: Snapshots of the magnetic field evolution for Model A (Table 2.1), shown at $t = 0$, 20 kyr, 200 kyr, and 2 Myr. The black curves are 10 contour lines of the poloidal flux function Ψ (i.e. the polodial magnetic field lines), equally spaced between $\Psi = 0$ and the maximum value $\Psi_{\max}$, at $t = 0$. The toroidal field is represented by the colour scale, which varies logarithmically, with a linear region around zero.

2.3.1 Hydromagnetic Core

First we consider Model A in which the effects of stellar spin-down, and Jones flux tube drift, and ambipolar diffusion are neglected (ie. the poloidal field is static in the core). The purpose of this section is to demonstrate clearly the hydromagnetic equilibrium described in Section 2.2.4. The drift of poloidal field lines in the core will be studied in Sections 2.3.2 and 2.3.3.

We note first that a significant twist angle can be associated with toroidal fields which have comparable strength to the poloidal field. For a field line in the core of length L, we estimate the twist angle to be of order

$$\zeta \sim \frac{LB_\phi}{r_\perp B_\lambda} \sim \left(\frac{L}{10^6\ \mathrm{cm}}\right)\left(\frac{10^6\ \mathrm{cm}}{r_\perp}\right)\frac{B_\phi}{B_\lambda} \sim 1\ \mathrm{rad}, \tag{2.62}$$

when $B_\phi \approx B_\lambda$. Changing the twist angle of a field line in the core requires differential rotation of its two ends where it is attached to the crust. Equatorial symmetry of the magnetic field implies no differential rotation – the two ends must move with the same speed. The same fact is seen formally from the equations. For the case of equatorial symmetry, the net flux of twist into the core vanishes

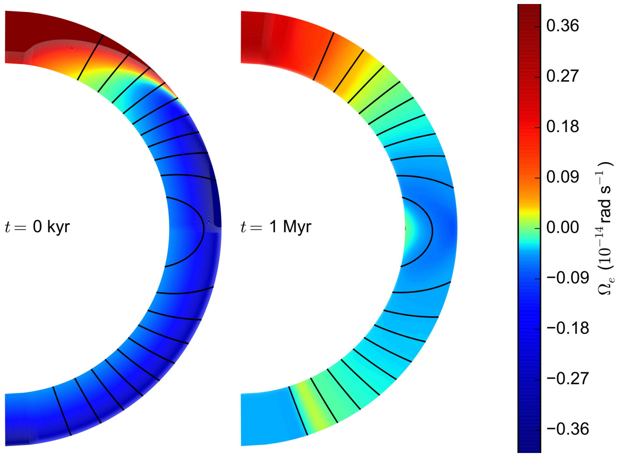

Figure 2.2: Snapshots of the evolution for Model A (Table 2.1), shown at $t = 0$ kyr, and 1 Myr. The plotting scheme is the same as Figure 2.1 but here colour shows Ω_e (the angular velocity of the electron fluid), the result of Hall drift in the crust. The thickness of the crust has been magnified by a factor of 2.5.

for each field line, as

$$J(\Psi, \lambda_2, t) - J(\Psi, \lambda_1, t) = 0, \tag{2.63}$$

(see Section 2.2.4). If the initial field has plane reflection symmetry about the equator, it will maintain this symmetry throughout the evolution. Then, by Equation (2.33), we see that

$$\partial_t I_{\text{core}}(\Psi, t) = 0 \quad \text{(if symmetric)}, \tag{2.64}$$

for all time. In reality it is likely that young neutron stars will have some toroidal field in order to stabilize the poloidal field. However in some of our simulations we consider a number of initial fields which display equatorial reflection symmetry, and have purely poloidal fields in the core. In this special case the evolution of the core toroidal field is trivial - it remains zero according to hydromagnetic equilibrium.

Poloidal fields which violate equatorial plane reflection symmetry give a non-zero net flux of twist into the core,

$$J(\Psi, \lambda_2, t) - J(\Psi, \lambda_1, t) \neq 0, \tag{2.65}$$

and we may see evolution of the toroidal field in the core. With this in mind we choose the initial

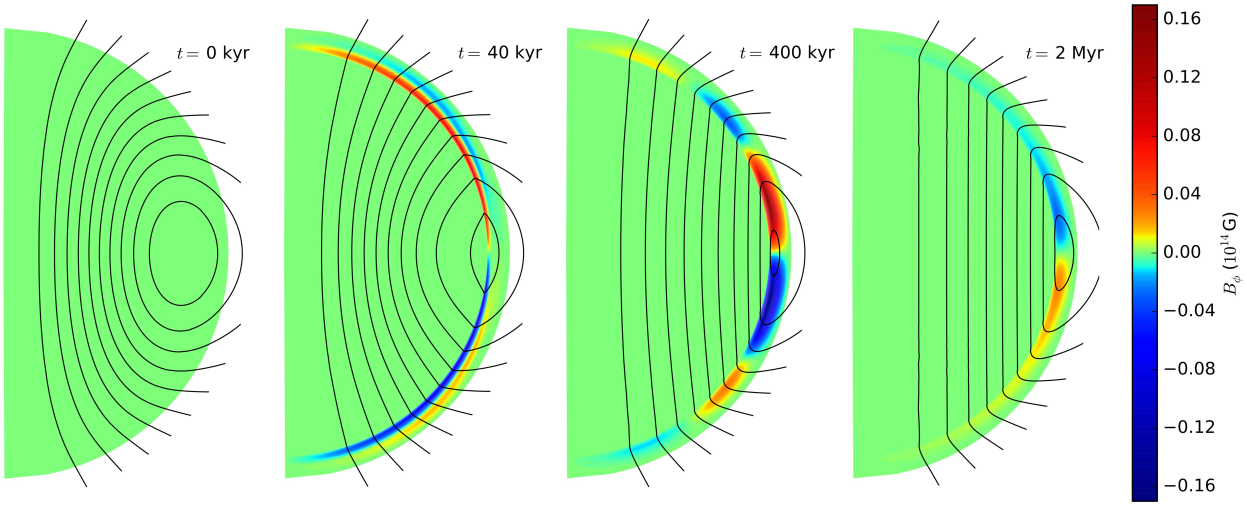

Figure 2.3: Snapshots of the magnetic field evolution for Model B (Table 2.1), shown at $t = 0$ kyr, 40 kyr, 400 kyr, and 2 Myr. The plotting scheme is the same as Figure 2.1.

poloidal field in Figure 2.1 to violate equatorial reflection symmetry. We enforce hydromagnetic equilibrium in Model A with the relaxation method outlined in Section 2.2.4.

The simulation shown in Figure 2.1 starts with a current sheet on the surface of the star in the northern hemisphere (see Figure 2.2). The current sheet shears poloidal field lines near the surface, and generates toroidal field with positive polarity in the northern hemisphere, and negative in the south. Hall drift in the crust slowly winds the core magnetic field in the azimuthal direction. At $t = 200$ kyr there is a weak toroidal field in the core, and several patches of toroidal field in the crust with alternating polarity. After $t \sim 600$ kyr the toroidal field reaches a steady state, with two patches near the equator in opposite hemispheres, which are damped by Ohmic diffusion from this point on. By this time the poloidal field has settled into the Hall attractor state, corresponding to constant electron angular drift velocity along poloidal field lines in the crust ($\Omega_\mathrm{e} = \Omega_\mathrm{e}(\Psi)$). Hall drift in the crust continues to wind the core field in the azimuthal direction, though more slowly as Ohmic diffusion dissipates the crustal currents. At $t = 2$ Myr the core supports a toroidal field of strength $B \sim 10^{12}$ G, and similar in the crust. The twist angle of a typical field line in the core is of order 10^{-2} rad, so Hall drift has only weakly twisted the core magnetic field in this model. It is possible that for different initial conditions, stronger azimuthal currents could inject a larger twist into the core. This model has confirmed the Hall attractor of [24] for core penetrating B-fields, with the correct hydromagnetic equilibrium enforced.

2.3.2 Jones Flux Tube Drift

Dissipative straightening of flux tubes

In a more realistic model the poloidal field lines in the core are not fixed, and are expected to drift as outlined in Section 2.2.4. Jones drift allows flux tubes to straighten by slipping with some viscous dissipation through the core electron fluid. As the flux tubes straighten, free energy stored in the curvature of the flux tubes is dissipated. The characteristic timescale of this straightening is

$$t_{\mathrm{diss}} \sim \frac{s}{v_{\mathrm{J}}} \tag{2.66}$$

with s the deviation from straight flux tubes. We approximate a curved flux tube as a circular arc, with $s \approx r_c^2/2R_c$, and radius of curvature R_c. The Jones drift velocity is approximated as

$$v_{\mathrm{J}} \sim \frac{\tilde{\sigma}}{4\pi n_e^2 e^2}\frac{BH_{\mathrm{c1}}}{R_c} = 2.8\times 10^{-8}\left(\frac{3.5\times 10^{37}\ \mathrm{cm}^{-3}}{n_e}\right)^2\left(\frac{\tilde{\sigma}}{10^{29}\ \mathrm{s}^{-1}}\right)\mathrm{cm\ s}^{-1}. \tag{2.67}$$

The timescale for flux tubes to straighten is then

$$t_{\mathrm{diss}} \sim \frac{2\pi n_e^2 e^2}{\tilde{\sigma}}\frac{r_c^2}{BH_{\mathrm{c1}}} = 450\left(\frac{n_e}{3.5\times 10^{37}\ \mathrm{cm}^{-3}}\right)^2\left(\frac{10^{29}\ \mathrm{s}^{-1}}{\tilde{\sigma}}\right)\ \mathrm{kyr}, \tag{2.68}$$

where we have taken the estimate of [8] $\tilde{\sigma} = 10^{29}B_{12}^{-1}\mathrm{s}^{-1}$. Note that the timescale is independent of the field strength B. The timescale for straightening can also be significantly shorter than the above estimate, depending on $\tilde{\sigma}$, which can be larger for cores with high muon densities [8]. Our advection velocity in Equation (2.67), illustrates the discrepency in the timescales of [79] and [8]. The advection velocity of [79], is typically $\sim 10^{-11}\mathrm{cm\ s}^{-1}$ [[79], Figures 5, 8, and 11 therein].

The Jones drift velocity acts perpendicular to poloidal field lines, in order to minimize the curvature. Thus, Jones drift becomes inactive when the flux tubes are straightened. However, when the field is straightened in the core, a sharp cusp forms on the crust-core interface, supported by strong toroidal currents at the base of the crust. This cusp will therefore be site to rapid Ohmic diffusion, which smooths the cusp, generating curvature in the field lines inside the core, and reactivating the Jones effect, which proceeds to straighten them again. So we see that the coupled crust-core system continuously evolves under the combined effects of Jones flux tube drift in the core, and Ohmic diffusion in the crust.

In this section we explore the evolution in two scenarios. Firstly, we consider the drift of flux tubes in a strongly magnetized neutron star, with Hall drift and Ohmic diffusion active in the crust. Secondly, we study the long timescale evolution of a moderately magnetized neutron star, and determine the decay timescale.

Flux tube drift and Hall drift (strong B)

For strong magnetic fields, Hall drift can interfere with the flux tube drift in the core (when t_{Hall} is comparable to t_{diss}). Figure 2.3 shows the evolution of a highly magnetized neutron star (Model B) with an initially poloidal field, evolving by Jones' flux tube drift in the core, coupled to a crust evolving with Hall drift and Ohmic diffusion. For this simulation we use $\tilde{\sigma} = 10^{29} B_{12}^{-1} \mathrm{s}^{-1}$. The initial field has maximum strength $B \approx 3 \times 10^{14}$ G in the core. The initial field displays equatorial symmetry, and thus Hall drift will not inject any magnetic twist into the core, meaning that the toroidal field remains zero there.

There are two main stages to the evolution of the core magnetic field in Model B. The first stage lasts for t_{diss}, and involves a rapid straightening of the flux tubes in order to relieve magnetic stresses. During this stage the core field dissipates its initial free energy, on viscous slippage through the fluid. The straightening of flux tubes in the core is associated with the formation of a sharp cusp in the poloidal field at the crust-core interface, supported by a toroidal current sheet at the base of the crust. This current sheet generates toroidal field deep in the crust through the Hall effect. The current sheet is also site to enhanced Ohmic dissipation. The regions of toroidal field in the crust are advected toward the equator, and much weaker higher order multipole structure forms in the toroidal field which is efficiently damped. The toroidal field is sufficiently weak, that it does not cause any large scale rearrangement of the poloidal field. Eventually activity due to Hall drift declines, as the Hall attractor drives the poloidal field in the crust to a state of rigid rotation of the electron fluid.

The second stage begins at $t \sim 1$ Myr. During this stage, Ohmic diffusion controls the evolution, which becomes a self-similar decay of the global magnetic field. Jones drift allows the core magnetic field to adjust on a timescale which is faster than Ohmic diffusion at the base of the crust, so that they effectively remain straight for the remainder of the evolution. Flux tubes in the core gradually drift outward, consistent with the rate of Ohmic diffusion at the base of crust. Analytic estimates describing this “Ohmic drift" of straight field lines will be given in Section 2.3.2, where we consider this drift in isolation, in the absence of any Hall drift. Flux in the core converges toward the null point in the field, which is located at the equator, on the crust-core interface, for this particular configuration. At the null point, the field lines close and annihilate. The evolution of the field into this state of self similar decay is not unique to these initial conditions, and we observe the same final state for a number of approximately dipole initial magnetic fields. We note that the Jones drift timescale does not scale with field strength, and likewise with Ohmic diffusion. This implies that timescales relating to the evolution of poloidal fields in Model B could be applied to initial fields with a variety of strengths.

Flux tube drift and no Hall drift (moderate B)

The second scenario of interest is the evolution of pulsar strength magnetic fields due to Jones flux tube drift in the core, in the case where crustal Hall drift is not important. This regime occurs for typical pulsar fields of $B \sim 10^{12}$ G or lower. With this in mind, in Model C we consider the crust evolving under Ohmic diffusion only so that long timescale simulations are less computationally expensive. We also avoid evolving the flux tubes in the core directly [Equation (2.52)], and instead enforce the boundary condition at the base of the crust that field lines remain vertical in the core ($B_\theta = B_r \tan\theta$ at $r = r_c$) as a result of Jones drift. This is a good approximation because the flux tubes can always straighten faster than Ohmic diffusion at the base of the crust, as seen in

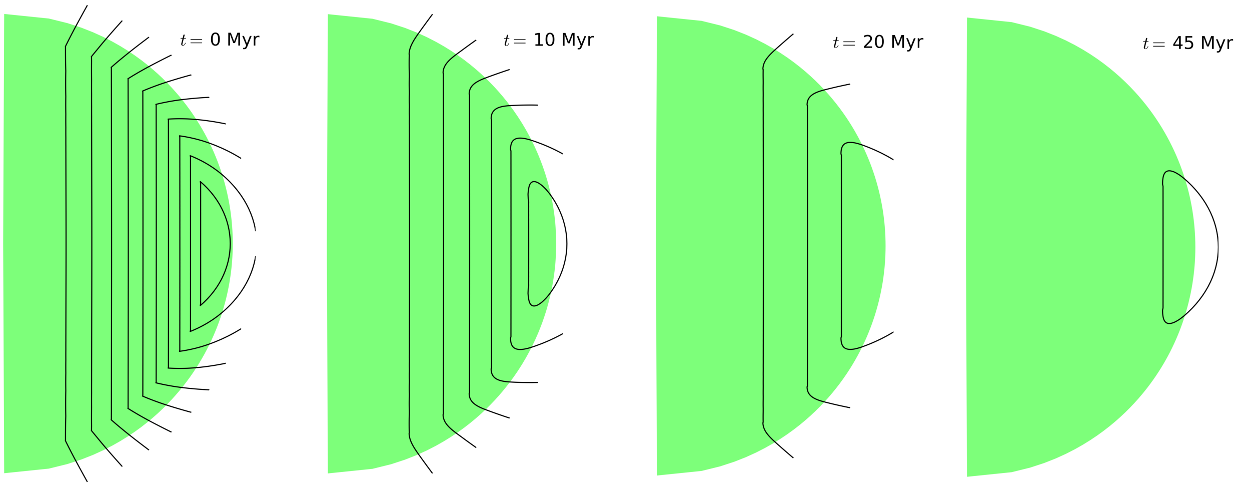

Figure 2.4: Snapshots of the magnetic field evolution for Model C (Table 2.1), shown at $t = 0$ Myr, 10 Myr, 20 Myr, and 45 Myr. The plotting scheme is the same as Figure 2.1. The toroidal field is everywhere zero.

Figure 2.3.

Figure 2.4 shows the long timescale evolution of Model C, with Jones flux tube drift in the core, coupled to a crust with Ohmic diffusion. The field in the core is pure B_z (In particular $\Psi \propto r_\perp^2$), and the initial crustal field is a dipole potential field matched on to the core. The field has typical strength $B \approx 10^{12}$ G. In the first ~ 1 Myr, diffusion at the base of the crust smooths the kink in the poloidal field, and the crustal field relaxes into an Ohmic eigenmode. From this point on the evolution of the global field can be likened to self similar decay. Tension in the magnetosphere ensures that poloidal field lines in the crust converge toward the null point at the equator. The field lines in the core are pulled along at the rate set by Ohmic diffusion, also toward the null point at the base of the crust, where they close and annihilate. For the remainder of the evolution the structure of the magnetic field remains unchanged, as it gradually grows weaker. The evolution of the dipole field strength is plotted in Figure 2.5. After ~ 150 Myr, the dipole field strength has decreased from $B \approx 10^{12}$ G to $B \approx 10^9$ G.

The timescale for magnetic flux to diffuse through the crust in the above scenario is very different from the Ohmic timescale of [19]. As an approximation, consider the cartesian configuration shown in Figure 2.6, and assume a constant diffusivity η throughout the crust. Curvature of the

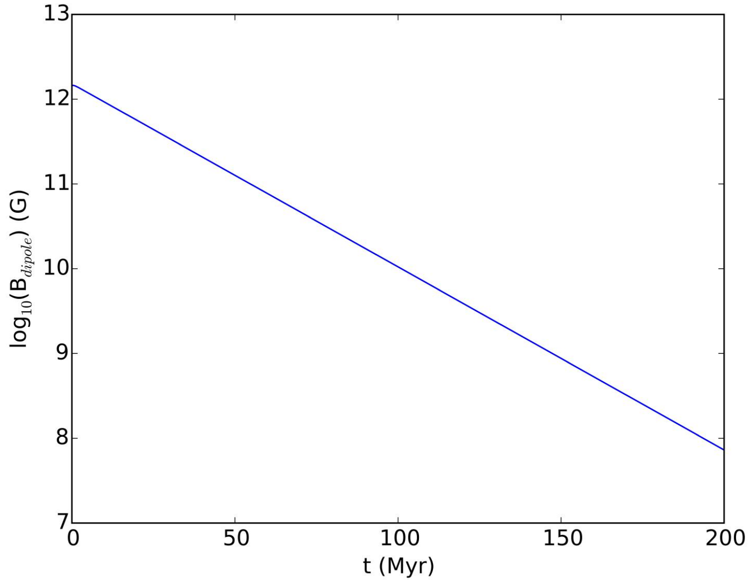

Figure 2.5: Decay of the dipole field for the magnetic field evolution shown in Figure 2.4.

field lines at the base of the crust generates a current sheet of thickness h, given by Ampere's law as

$$j \sim -\frac{c}{4\pi}\frac{B_x}{h}, \tag{2.69}$$

using Ohm's law this gives the electric field

$$E \sim -\frac{c}{4\pi\sigma}\frac{B_x}{h}. \tag{2.70}$$

As in Section 2.2.4, we use this electric field to estimate the velocity of magnetic field lines due to Ohmic diffusion through $\boldsymbol{E} = -\boldsymbol{v} \times \boldsymbol{B}/c$. The resulting velocity of field lines in the x-direction is

$$v_{\rm ohm} \sim \frac{\eta}{h}\frac{B_x}{B_z}, \tag{2.71}$$

with B_z and B_x the vertical and horizontal components of the field. For this configuration a quasi-steady drift is established with the current sheet occupying the region of the crust with highest conductivity, i.e. the deep crust. Its thickness h is a few hundred meters. The quasi-steady drift is established on the timescale h^2/η, and the drift is associated with the transport of magnetic field

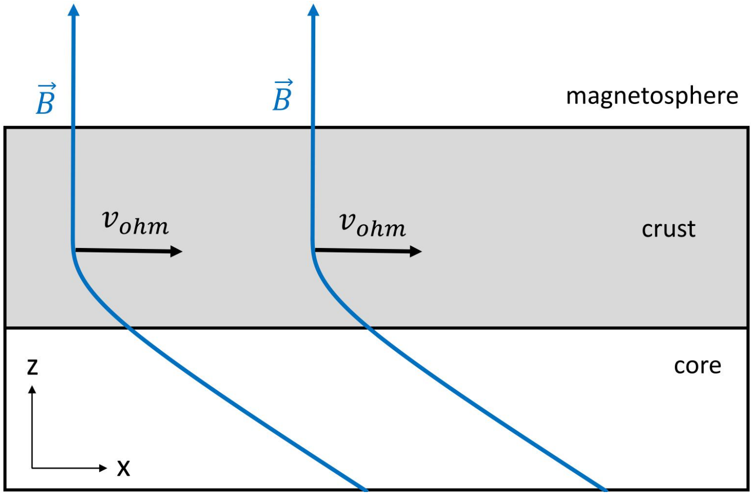

Figure 2.6: Plane parallel slab (grey), with length l. Field lines (blue) move to the right consistent with the rate set by Ohmic diffusion.

lines with characteristic time

$$\tilde{t}_{\rm ohm} \sim \frac{hl}{\eta}\frac{B_z}{B_x} = 150 \left(\frac{h}{3 \times 10^4 \text{ cm}}\right)\left(\frac{l}{\pi r_*}\right)\left(\frac{\sigma}{3.6 \times 10^{24} \text{ s}^{-1}}\right) \text{Myr}, \tag{2.72}$$

where we have assumed $B_z \approx B_x$, and the current sheet thickness $h \approx 3 \times 10^4$ cm corresponding to the highly conducting region of the deep crust. We have used $\sigma = 3.6 \times 10^{24}$ s^{-1}, corresponding to phonon scattering at $T \approx 2 \times 10^8$ K [24]. This timescale can be greater by an order of magnitude compared to the Ohmic timescale of [19], depending on the thickness of the crust and the geometric factor B_z/B_x. The timescale given by Equation (2.72) corresponds to the time taken for the dipole field strength to decay by approximately 3 orders of magnitude for the numerical simulation seen in Figure 2.4.

2.3.3 Rapidly Rotating Newborn Neutron Stars

The origin of strong magnetic fields in neutron stars is not well understood. Some models suggest a fossil field, left behind by the progenitor [100], while others invoke dynamo mechanisms requiring the neutron star to be born with millisecond spin periods [101]. Here we assume that a highly magnetized neutron star can be born with a 1 millisecond spin period, and consider the

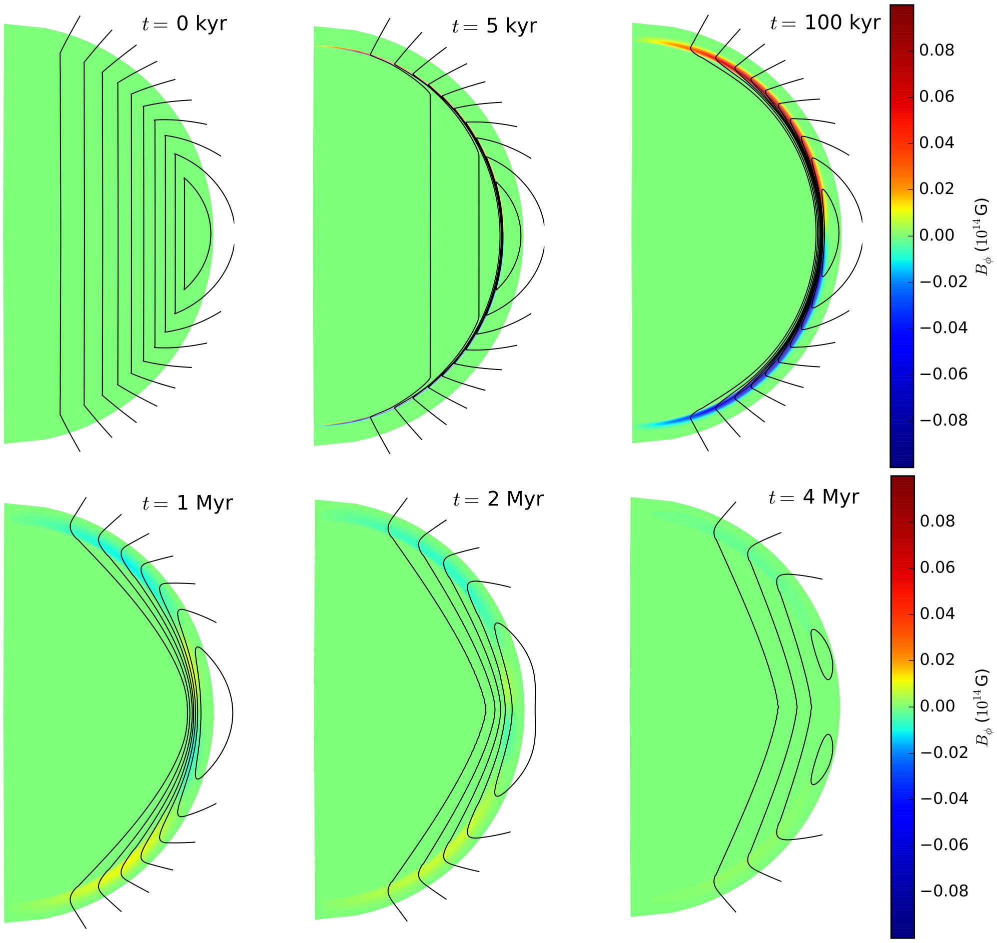

Figure 2.7: Snapshots of the magnetic field evolution for Model D1 (Table 2.1), shown at $t = 0$ kyr, 5 kyr, 100 kyr, 1 Myr, 2 Myr, and 4 Myr. The plotting scheme is the same as Figure 2.1. This simulation begins 300 yr after the neutron star birth, with surface field strength $\sim 5 \times 10^{12}$ G, and spin period 10.9 ms.

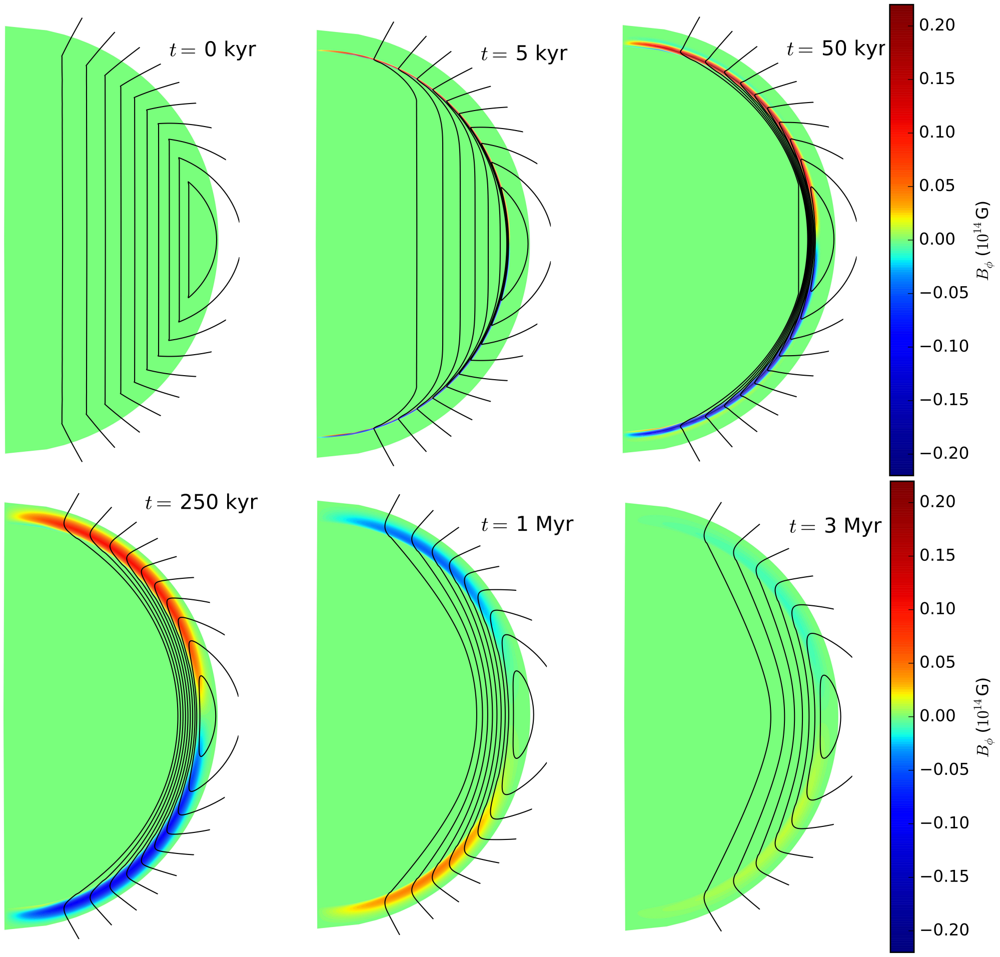

Figure 2.8: Snapshots of the magnetic field evolution for Model D2 (Table 2.1), shown at $t = 0$ kyr, 5 kyr, 50 kyr, 250 kyr, 1 Myr, and 3 Myr. The plotting scheme is the same as Figure 2.1. This simulation begins 300 yr after the neutron star birth, with surface field strength $\sim 10^{13}$ G, and spin period 21.8 ms.

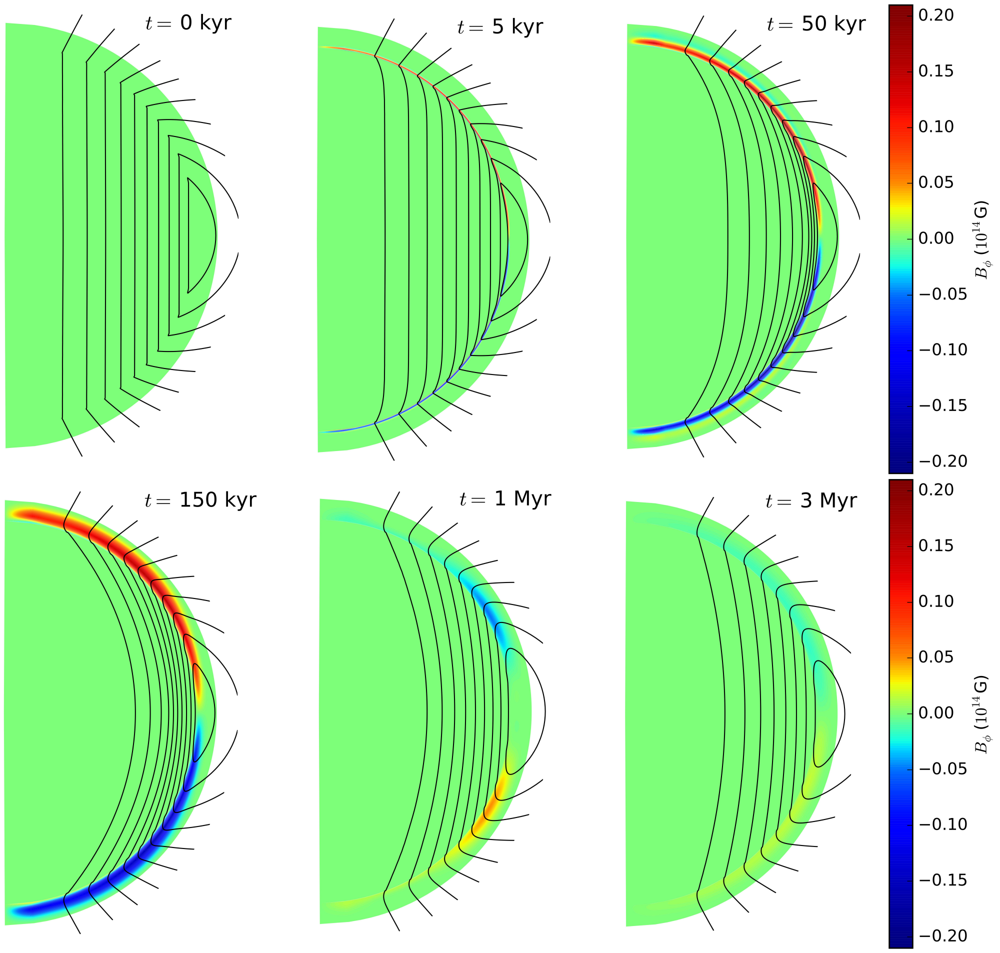

Figure 2.9: Snapshots of the magnetic field evolution for Model D3 (Table 2.1), shown at $t = 0$ kyr, 5 kyr, 50 kyr, 150 kyr, 1 Myr, and 3 Myr. The plotting scheme is the same as Figure 2.1. This simulation begins 300 yr after the neutron star birth, with surface field strength $\sim 2 \times 10^{13}$ G, and spin period 43.5 ms.

implications for the evolution of the magnetic field. In particular, we are interested in the interaction of superfluid neutron vortices with flux tubes, as a means for the rotational energy of the star to rearrange the core magnetic field. Importantly the cooling curves of the Cas A remnant suggest that the transition to superfluidity in the core takes place after $t \sim 300$ years [86, 87]. As was pointed out by [16], by this time a typical magnetar ($B \sim 10^{15}$ G) will have a spin period > 1 s. It is simple to show that the ratio of rotational to magnetic energy is very small, and it is difficult to envisage how the core field could be significantly rearranged by a transfer of rotational energy. However, for neutron stars born with weaker magnetic fields, corresponding to a so-called weak-field magnetar (or high-B pulsar), this is not the case. Specifically, if a neutron star is born with initial spin period 1 ms, and $B \sim 10^{13}$ G, then after 300 years, the spin period will be 21.8 ms. Then the ratio of rotational to magnetic energy is large, and will remain so for an extended period after the transition to neutron superfluidity.

In Models D1, D2 and D3 we model neutron stars, with a range of initial magnetic field strengths, assuming a birth spin period 1 ms. Our simulations begin 300 yr after the neutron star birth, corresponding to the time of phase transition to neutron superfluidity. We model the spin evolution of the star self consistently according to $\dot{\Omega} = -\beta\Omega^3$, where $\beta = 2a_1^2/3c^3 I$. Here a_1 is the dipole moment of the surface magnetic field, and we take $I = 10^{45}$ g cm^2 as a typical moment of inertia. The spin evolution of the star determines the velocity of the neutron vortices, according to

$$\boldsymbol{v}_\perp = -\frac{r_\perp \dot{\Omega}_n}{2\Omega_n}\hat{\boldsymbol{e}}_{r_\perp}. \qquad (2.73)$$

In Model D1 we use an initial field of strength $\sim 5 \times 10^{12}$ G at the surface, and 6.9×10^{12} G in the core. We set the initial (here initial refers to the beginning of the simulation–300 yr after the neutron star birth) spin period accordingly to 10.9 ms. We show the results of this simulation in Figure 2.7. In the first 100 kyr the flux is rapidly pushed out of the core at the velocity $\boldsymbol{v}_\perp$. In the outer core the flux tubes are severely deformed, and the tension force $\boldsymbol{f}_B$ becomes large enough to cause cut-through in a thin layer beneath the crust. The sharp curvature of poloidal field lines at the base of the crust is site to a strong toroidal current sheet, which generates a quadrupolar toroidal field through Hall drift, and rapid Ohmic dissipation of the poloidal field. The expulsion of flux tubes can result in an order of magnitude increase in the poloidal field strength in the outer core.

From this point on, the flux tubes slide vertically along the neutron vortices toward the equator (away from the crust-core interface) with the projected Jones velocity $(\boldsymbol{v}_\mathrm{J} \cdot \hat{\boldsymbol{e}}_n)\hat{\boldsymbol{e}}_n$. The flux tubes form a “>" shape, with the cusp located along the equator in the outer core. The cusp becomes sharper, until the tension force $\boldsymbol{f}_B$ is large enough to cut through the vortices, and begins to minimize it at ~ 880 kyr. After ~ 1 Myr, flux tubes are advected by the moving vortex lines throughout the core, except for a small region around the cusp where the tension force $\boldsymbol{f}_B$ is large. The toroidal field deforms into an octupole configuration, which is severely damped by Ohmic diffusion. After 2 Myr the crustal poloidal field begins to develop an octupole component, due to the magnetic pressures and tensions communicated from the base of the crust through Ohmic diffusion. This is clearly evident at 4 Myr in Figure 2.7. Throughout this simulation Hall drift does not play a major role in the redistribution of the magnetic field, because the field strength is weak, and Ohmic diffusion is the dominant effect ($t_\mathrm{ohm} < t_\mathrm{hall}$). The spin period after 4 Myr in this simulation is 0.85 s.

In Model D2 the initial field has strength ~ 10^{13} G at the surface, and 1.4×10^{13} G in the core. We set the initial (300 yr after neutron star birth) spin period accordingly to 21.8 ms, and show the results of this simulation in Figure 2.8. In the first 5 kyr vortices cut through flux tubes throughout the core, except for a thin cylinder around the axis of rotation where the vortices move slowly. In the cut-through regime the flux tubes are allowed to bend, and as a result they curve away from the axis of rotation due to the collective drag of outward moving vortices cutting through them. After 10 kyr the vortices are moving slowly enough that they advect flux tubes throughout the core, except for a thin layer beneath the crust where the flux tube tension is large. In this thin layer the vortices cut through, and the terminal velocity of flux tubes gets very small due to the high density of flux tubes. The sharp curvature of flux tubes at the crust-core interface results in the development of a strong current sheet in the deep crust, which is site to enhanced Ohmic dissipation, and the development of a quadrupole toroidal field through Hall drift.

As the star spins down the number density of vortices decreases along with the critical force $n_v \tilde{f}_v$. As a result, after $\sim$ 100 kyr the region of cut-through in the outer core begins to grow, allowing the flux tubes to drift once again back into the core, with the Jones drift velocity $\boldsymbol{v}_{\rm J}$. The thickness of the cut-through layer increases as the star continues to spin down. After 3 Myr the toroidal field is significantly damped by Ohmic diffusion, and the flux tubes in the core remain curved outward in the outer regions of the core, a result of the collective drag by the vortex lines cutting through the flux tubes. The spin period after 3 Myr in this simulation is 1.87 s.

In Model D3 we use an initial field of strength $\sim 2 \times 10^{13}$ G at the surface, and $\sim 2.7 \times 10^{13}$ G in the core. This field is stronger than previous models, so the star spins down faster, and we set the initial (300 yr after neutron star birth) spin period accordingly to 43.5 ms. The results of this simulation are shown in Figure 2.9. In the beginning the vortices cut through in the entire core, except for a thin cylinder around the spin-axis where they are slowly moving. As a result of the drag from the cutting-through vortices, the flux tubes bend away from the axis of rotation, and bunch in the outer core. The sharp curvature of poloidal field lines at the crust-core interface is supported by a strong toroidal current sheet. A toroidal field with quadrupole structure grows in the deep crust, which is site to enhanced Ohmic dissipation. As the star spins down the force of vortices pushing on flux tubes becomes smaller while the tension force grows larger. This continues until $\sim$ 250 kyr, when the flux tubes stop moving away from the spin-axis, and begin moving back toward. From this point on, the core mostly operates in the cut-through regime, and the combination of the slow spin period, and strong magnetic field means that the flux cannot be expelled from the core. The flux tubes remain bent away from the spin-axis due to the drag of cutting-through vortices for the remainder of the simulation, while the crustal field decays primarily due to Ohmic diffusion. The spin period after 3 Myr is 4.01 s. The spin periods we observe in this simulations are not unlike the spin periods of known low-B magnetars. However, it seems unlikely that the toroidal field in these models is strong enough to break the crust and power classical magnetar activity.

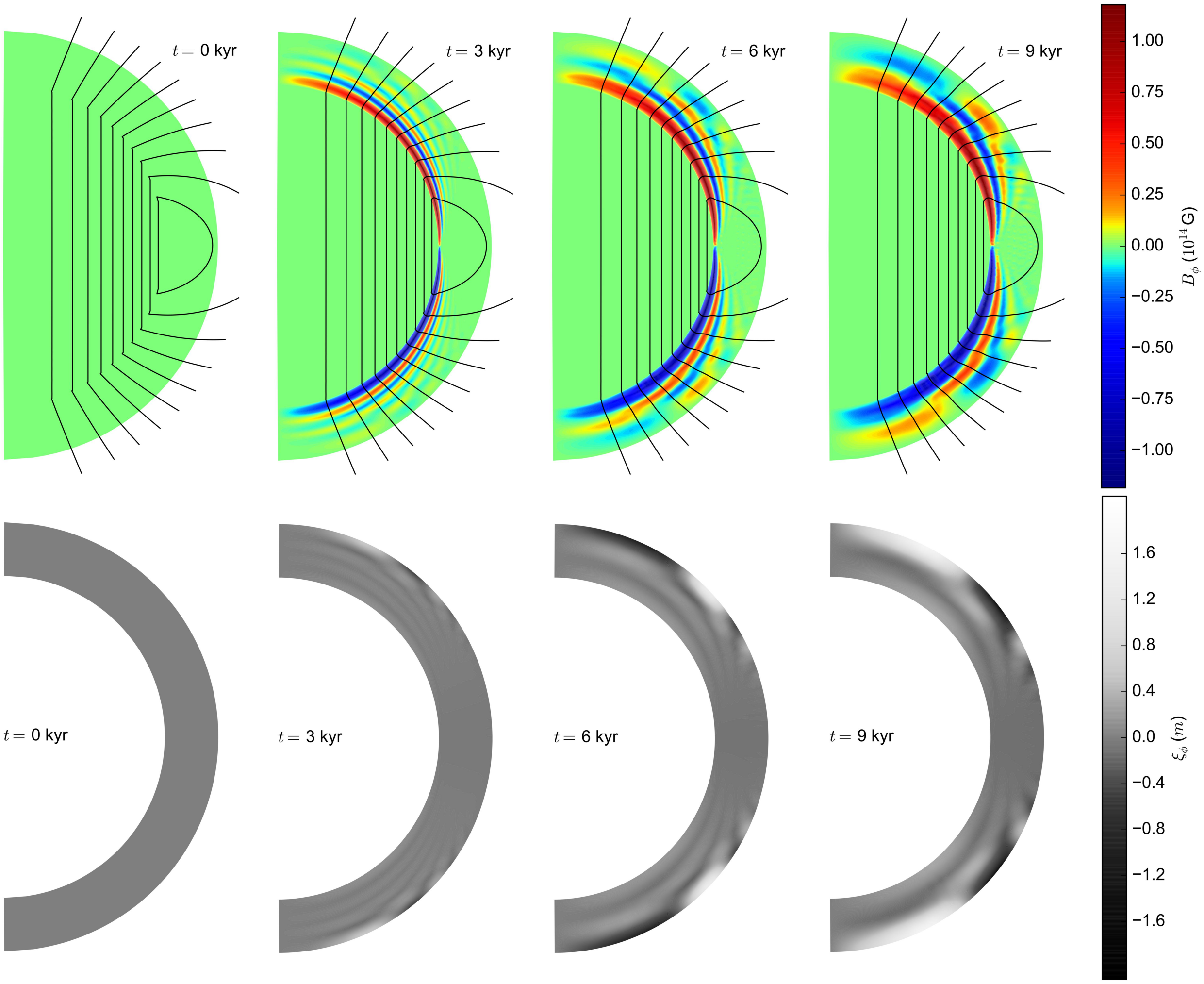

Figure 2.10: Snapshots of the magnetic field evolution for Model E (Table 2.1), shown at $t = 0$ kyr, 3 kyr, 6 kyr, and 9 kyr. Top row: The plotting scheme is the same as Figure 2.1. Bottom row: Lagrangian displacement of the crust is shown on the colour scale which varies logarithmically, with a linear region around zero. The thickness of the crust has been magnified by a factor or 2.5 in both rows.

2.3.4 Elastic Back-Reaction

In this section we present the coupled evolution of the elastic crustal deformation, and the magnetic field under Hall drift and Ohmic diffusion. The initial magnetic field is chosen such that there is a sharp cusp in the field on the crust-core interface. [19] showed that such a disturbance will launch circularly polarized “Hall waves", which can propagate from the crust-core interface, and transport magnetic energy toward the surface of a neutron star. [14] showed that Hall waves in strong magnetic fields can trigger a thermoplastic instability in the crust, which can generate X-ray activity associated with magnetars. The elastic deformation of the crust can be significant in the upper layers, where the magnetic energy density $\mu_{\mathrm{B}} = B_z^2/8\pi$ is comparable to the crustal shear modulus μ. Here the crust cannot balance arbitrary stresses generated by Hall drift, so it yields, thus nullifying the Hall effect. In their 1D plane parallel model, [102] show that the Hall term in the Hall-elastic evolution equation is suppressed by a factor $(1 + \mu_{\mathrm{B}}/\mu)^{-1}$, so that when $\mu_{\mathrm{B}} \gg \mu$, Hall drift is significantly suppressed. Unfortunately in this regime ($\mu_{\mathrm{B}} \gg \mu$), we encounter severe numerical instabilities due to our explicit time integrator. Thus, for now we are restricted to work in the limit $\mu_{\mathrm{B}} \leq \mu$, where we may still demonstrate the effectiveness of the relaxation method outlined in Section 2.2.1.

In Model E we chose the initial field to be purely poloidal, with vertical field lines (pure B_z) in the core (in particular $\Psi \propto r_\perp^2$), and a dipole potential field in the crust. The initial field has strength $B \approx 2 \times 10^{14}$ G. There are several physical processes which could cause such a cusp at the crust-core interface in a highly magnetized neutron star, and these motivate our choice of initial field. As demonstrated in Section 2.3.3, if the magnetic field is sufficiently weak, superfluid neutron vortices will be present for a significant period during the spin down of a rapidly rotating neutron star, while the ratio of rotational to magnetic energy is high. Transport of flux tubes by outward moving vortices can result in a cusp in the field at the base of the crust, though this will not result in vertical field lines in the core as shown above. Jones flux tube drift in a young magnetar can result in a cusp in the field, and could launch Hall waves, depending on the composition of the core and the subsequent value of the drag coefficient α. The launching of short wavelength Hall waves depends on Jones drift being significantly faster than the Hall timescale. There may be other effects which could drive a fast change of the core magnetic field, and thus launch the Hall waves. [20] found that in young magnetars with hot cores ($T_{\text{core}} \approx 10^9$ K) and ultra-strong magnetic fields ($B \gtrsim 10^{16}$ G), ambipolar diffusion operates in the friction dominated regime, and may cause a fast rearrangment of the core magnetic field. Additionally there may by hydromagnetic instabilities in young magnetars which can result in a rapid rearrangement of the core magnetic field.

The magneto-elastic evolution in Model E is shown in Figure 2.10. Initially, the cusp in the poloidal field generates strong toroidal currents which in turn generate toroidal field. The result is a burst of Hall waves which propagate away from the core. These waves are the 2D analogue of the Hall waves shown in [15]. At 3 kyr the small amplitude, short wavelength Hall waves, have traveled the furthest toward the stellar surface. The long wavelength Hall waves near the core evolve much more slowly. This can be understood if we consider our system as a constant background field, with an oscillating perturbation which is linear in the field. This is valid for the small amplitude Hall waves early in the evolution, which are sufficiently weak such that evolution equation for the poloidal field is weakly coupled to the toroidal field. This means the structure of the poloidal field is effectively constant. Here we understand the background field to be poloidal, and the perturbation is the Hall waves, early in the evolution before non-linearity becomes significant. The dispersion relation is

$$\omega = \frac{ck|\boldsymbol{k} \cdot \boldsymbol{B_0}|}{4\pi n_e e}, \tag{2.74}$$

[19] where $\boldsymbol{k}$ is the wave vector, $k := |\boldsymbol{k}|$, and B_0 a uniform background magnetic field. The waves are seen to fan out from the crust-core interface over the next few kyr, traveling furthest near the poles. This is due to the geometry of the existing background field. The group velocity of Hall waves in the linear regime follows from the dispersion relation [19] as

$$v_{\text{gp}} = \pm \frac{ck[\boldsymbol{B_0} + (\hat{\boldsymbol{k}} \cdot \boldsymbol{B_0})\hat{\boldsymbol{k}}]}{4\pi n_e e}, \tag{2.75}$$

where $\hat{\boldsymbol{k}} := \boldsymbol{k}/k$. Near the poles, the background field is almost pure B_r, so the waves travel radially there. However, near the equator, the background field is almost entirely B_θ, so there is less radial propagation. After the first 6 kyr the waves begin to evolve non-linearly. Hall drift sets in and advects the wave fronts toward the equator of the star. But due to the gradient in electron density, and the fanning of the wave fronts, they are advected non-uniformly, and start to break apart. Diffusion also smears the wave fronts, and decreases the amplitude. The evolution of the crustal displacement is shown in lower panel of Figure 2.10. The displacement is largest near the surface, where the shear modulus is smallest and the crust yields easily. The crustal displacement reaches a maximum amplitude of $\sim$ 2 m.

2.4 Discussion

In this paper we have modeled the coupled magnetic field evolution of neutron stars in the crust and the core. In the crust we include evolution due to Hall drift and Ohmic diffusion [19], as well as the elastic response of the solid crust. We enforce the correct hydromagnetic equilibrium in the fluid core. We also explore the effects of the Jones flux tube drift [8], and expulsion by superfluid neutron vortices during spin-down [7, 29, 30]. In this section we discuss the preliminary implications of these results, in the context of the galactic population of neutron stars, and their observable behavior.

In Section 2.3.1 we modeled the evolution of an initial poloidal field with broken equatorial symmetry. We evolved the crustal magnetic field through Hall drift and Ohmic diffusion, while the core field evolved according to the hydromagnetic equilibrium we formulate in Section 2.2.4. We confirm the Hall attractor of [24] for B-fields which penetrate the core, while satisfying the correct hydromagnetic equilibrium.

In Section 2.3.2, we presented simulations of Jones flux tube drift, which show that the B-field in the core can straighten under the enhanced self tension possessed by the quantized flux tubes. The straightening of flux tubes is associated with the dissipation of free energy stored in the curvature of the field. This straightening occurs on a timescale

$$t_{\text{diss}} \sim 450 \left(\frac{n_e}{3.5 \times 10^{37}\ \text{cm}^{-3}} \right)^2 \left(\frac{10^{29}\ \text{s}^{-1}}{\tilde{\sigma}} \right)\ \text{kyr}, \tag{2.76}$$

but can occur significantly faster depending on the value of $\tilde{\sigma}$. Interestingly, this can generate a burst of activity in highly magnetized neutron stars which were previously in the Hall attractor state. Importantly, we show that for the range of values of $\tilde{\sigma}$ estimated by [8], t_{diss} is always much smaller than the modified Ohmic timescale $\tilde{t}_{\text{ohm}}$ [Equation (2.72)], so that the Ohmic timescale governs the rate of depletion of the global magnetic field. However this timescale is greater by an order of magnitude than the Ohmic timescale of [19].

The timescale for depleting the pulsar magnetic fields in these simulations is very sensitive to the choice of electrical conductivity, and it is worthwhile to discuss the implications of this. Phonon scattering, and impurity scattering are the main ways currents can be diffused in a neutron star crust. Phonon scattering is exponentially suppressed when $T < T_U = 8.7 \times 10^7$ K $\rho_{14}(Y_e/0.05)(Z/30)^{1/3}$[102], and the Umklapp processes freeze out. Impurity scattering is dominant at low temperatures ($T < T_U$), or high impurity levels. Estimates of the impurity levels in the deep crust range from $Q_{\text{imp}} \approx 10^{-3}$ [103], to $Q_{\text{imp}} \approx 10$ [104]. For young or accreting pulsars, with temperatures $T \gtrsim 10^8$ K, $T > T_U$, and typical impurity levels, phonon scattering will be dominant in the deep crust. Then the timescale for magnetic diffusion in the crust, using the electrical conductivity in Section 2.2.1 (phonon scattering at $T \approx 2 \times 10^8$ K), is given by the modified Ohmic timescale (2.72) $\tilde{t}_{\text{ohm}} \sim 150$ Myr. A full treatment would include the effects of accretion onto the neutron star surface, and burial of the magnetic field. The consequences of this are not clear, but it should be noted that burial of the field (see e.g. [5] and the field configurations therein) could result in suppression of the ratio B_z/B_x, leading to an even shorter timescale for the depletion of the global field. [105] found that Ohmic dissipation proceeds faster when thermal feedback on the crustal conductivity is included. This could further shorten the timescale of 150 Myr we observe in our simulations.

After a young pulsar has cooled, or accretion has subsided, the neutron star crust will cool. For $T \sim 10^6$ K, $T < T_U$, and impurity scattering will dominate. Then [102] give the electrical conductivity in the deep crust as

$$\sigma_Q = 4.4 \times 10^{25}\ \mathrm{s}^{-1} (\rho_{14}^{1/3}/Q_{\mathrm{imp}})(Y_e/0.05)^{1/3}(Z/30). \tag{2.77}$$

In the impurity dominated regime, the timescale for flux to diffuse through the crust is

$$\tilde{t}_{\mathrm{ohm}} \sim hl \frac{4\pi\sigma_Q}{c^2}\frac{B_z}{B_x} = \frac{1.8\ \mathrm{Gyr}}{Q_{\mathrm{imp}}}, \tag{2.78}$$

meaning that flux is effectively frozen into the crust, and the dipole surface field of the pulsar will no longer decay. For any impurity parameter which yields a decay time comparable to the Hubble time ($Q_{\mathrm{imp}} \lesssim 0.13$), the field will be approximately stable. This could explain the persistence of magnetic fields in millisecond pulsars, after periods of rapid depletion at higher temperatures. Alternatively, if impurity levels are much higher, as suggested by [104], then Ohmic diffusion can proceed rapidly in pulsars even after cooling, so that the crust cannot prevent decay of the dipole field. This would suggest that something elsewhere in the core was inhibiting the motion of flux.

In the core flux tubes may get caught on magnetized neutron vortices, and be forced to move outward at the same rate. The vortices move outward on a timescale equal to the spin-down time of the star, which is very long for millisecond pulsars. [8] also found that while the outer core is likely a type-II superconductor, protons in the inner core may be type-I. In type-I superconductors magnetic flux is confined to macroscopic filaments of normal matter. Due to the presence of muons in the inner core in some equations of state, motion of the filaments would be accompanied by the formation of large gradients in chemical potential, limiting the motion of flux to the rate set by weak nuclear interactions [8]. Additionally our simulations do not include a smooth transition from the solid crust to the liquid core. It is possible that some flux tubes get pinned in the pasta phases at the crust core interface, thus causing a remnant field to be left behind. Any of these could provide an explanation for the persistence of a magnetic field in millisecond pulsars despite the decay time we calculate.

In Section 2.3.3 we modeled the expulsion of flux from the core by the outward motion of neutron vortices during spin-down. We chose the initial spin period for our models by assuming the star was born with a 1 ms spin period, and allowed to spin down for 300 years before the phase transition to superfluidity, as suggested by the Cas A remnant [[86], [87]]. Models D1, D2, and D3 have typical magnetic field strengths of 5×10^{12} G, 10^{13} G, and 2×10^{13} G respectively.

While [7] argues that flux tube tension is small compared to the critical force $n_v \tilde{f}_v$, we find that it plays a crucial role in rearranging flux tubes in the core — even for weaker magnetic fields $\lesssim 5 \times 10^{12}$ G. This is because the transport of flux tubes by vortices results in the formation of sharp magnetic features, which possess enormous tension, particularly in the outer core, where flux tubes are anchored to the crust. Even in regions where the tension force $\boldsymbol{f}_B$ is small, it causes the flux tubes to slide along neutron vortices, and plays an important role in the large scale distribution of flux. We found that when $B \gtrsim 2 \times 10^{13}$ G, the combination of the strong magnetic field and the slower spin period, means that the magnetic field could not be expelled from the core. On the other hand, we found that for $B \lesssim 10^{13}$ G, the outward motion of vortices resulted in a partial expulsion of the core magnetic field, into the outer core and deep crust. We find that in all simulations, as the field is pushed away from the spin-axis a toroidal field grows in the deep crust.

When the flux is expelled into the outer core regions, a strong toroidal current sheet develops in the deep crust. These currents drive Ohmic dissipation at an enhanced rate, as compared to core-penetrating fields which vary on larger spatial scales. Additionally, the bunching of flux tubes in the outer core means the poloidal field can be an order of magnitude stronger there, compared to the spin-down inferred dipole field strength. At some stages in our simulations the field configurations loosely resemble the crust-confined fields of [22], so we may expect thermal emission similar to that in their crust-confined models. The crucial difference is that in our simulations the field penetrates the core. It seems unlikely that flux expulsion could power the magnetar activity of weak-field magnetars or high-B pulsars since the toroidal field in the crust is always $< 10^{14}$ G. However, it is possible that flux expulsion could power thermal emission in isolated neutron stars, due to enhanced Ohmic dissipation in the deep crust.

Recent observations of cyclotron emission from the weak-field magnetars SGR 0418+5729 and SWIFT J1822.3-1606 suggest the presence of small-scale magnetic loops near the stellar surface, which can be up to two orders of magnitude stronger than the spin-down inferred dipole field strength [106, 107]. Such strong high-order magnetic multipoles may drive Hall drift on short timescales, and produce X-ray activity normally associated with classical magnetars.

The main shortcoming of our work is that we have not resolved the controversy in the literature between the timescales of [8] and [94], and this is left for future work. We used the drift timescales derived by Jones, as they lead to interesting dynamical effects at the crust-core interface that are well-modeled in our numerical experiments. Future papers in this series will include the effects of field burial by accretion, and a study of the galactic population of pulsars.

Chapter 3: Pulsar Glitches and Star Quakes

3.1 Introduction

On 2016 December 12 a glitch of magnitude $\Delta\nu/\nu = 1.431 \times 10^{-6}$ was observed in the Vela pulsar (PSR J0835-4510) with the 26 m telescope at Mount Pleasant, Tasmania, and the 30 m telescope at Ceduna, South Australia [40]. For the first time, each single radio pulse was recorded during the glitch, and the pulse shape was seen to change dramatically. First, a broad pulse was detected, followed by a single null (missing) pulse. The following two pulses showed an unusually low linear polarization. [108] constrained the rise time of the glitch to be less than 12.6 s. Additionally they found evidence for a slow-down of the pulsar immediately before the spin-up glitch.

Detection of the radiative feature accompanying the 2016 Vela glitch was challenging because of its very short duration (two pulses, ~0.2 s) and no subsequent long-term change in the pulse shape. This is different from the known behavior of high-B pulsars, such as PSR J1119-6127 which showed persistent abnormal radio pulsations in the months following its 2007 glitch [109]. Note also that no significant radiative change had been associated with a glitch in a canonical radio pulsar until the dedicated observation of Vela in 2016 by [40].

This observation shows for the first time that the magnetosphere can be affected by a glitch – an event considered to originate from the interior of the neutron star. We see no plausible mechanism for the coupling between the pulsar interior and the magnetosphere other than seismic motions of the crust (a quake). Excitation of seismic motions requires a sudden change of elastic stress on the timescale $\ll 1$ ms (the wave crossing time of the crust thickness). The quake is possible if the crust is stressed beyond its critical strain and "fails", launching shear waves. In this paper, we do not provide an argument for why a large stress should build up in Vela's crust. However, we argue that a quake is able to connect the 2016 glitch with the observed major magnetospheric disturbance coincident with the glitch.

The quake mechanism of exciting the magnetosphere of a neutron star was previously studied in several works [110–113]. The wave transmission coefficient at the crust-magnetosphere interface was calculated by [110], who considered quakes as possible triggers of gamma-ray bursts (GRBs). We consider much less energetic events, and thus we do not expect a bright GRB to accompany a glitch. Other key differences are that our model is two-dimensional (2D), time-dependent, and includes the self-consistent magnetic coupling to both the magnetosphere and the liquid core. These advances are essential for our model of the 2016 December event. We also include a liquid ocean, which was absent in the study of [110], but find that it has little effect on the phenomena that we study.

We find that the quake shear waves spread sideways and fill the whole crust. Therefore, seismic crustal oscillations populate the entire magnetosphere with Alfvén waves. The Alfvén waves bounce in the closed magnetosphere, become de-phased, and generate strong electric currents. De-phasing, in concert with growing wave amplitude in the outer magnetosphere leads to charge starvation, and $e^{\pm}$ discharge. The discharge can flood the magnetosphere with plasma, interrupting the observed radio emission. We also find that excitation of Alfvén waves in the liquid core efficiently drains energy from the crustal oscillations, and thus limits the quake duration. Assuming the mean magnetic field at the crust-core interface is comparable to the surface dipole field, and that the field in the core is bunched into flux tubes or domains (as is expected for type-II and type-I superconductors, respectively), we find that the quake amplitude is exponentially reduced on the timescale ~ 0.2 s, fast enough to cause a single null.

The paper is organized as follows. In Section 3.2 we present the relevant parameters of Vela, and other physics input required by our model. In Sections 3.3 and 3.4 we provide an analytic description of the proposed picture of the 2016 event. Section 3.5 outlines the formalism and numerical method for the full three-dimensional (3D) problem, although we only present results in 2D axisymmetry in this work. In Section 3.6 we show four sample numerical models, and the results are further discussed in Section 3.7.

3.2 Vela Model

3.2.1 Observed Parameters of the Vela pulsar

The pulsar has spin period $P = 2\pi/\Omega = 89$ ms [114], and the light cylinder radius

$$R_{\mathrm{LC}} = \frac{c}{\Omega} = 4.2 \times 10^{8}\,\mathrm{cm}. \tag{3.1}$$

Its spin-down rate $\dot{\Omega} = -9.8432 \times 10^{-11}$ rad s^{-2} gives a measurement of the magnetic dipole moment of the star $\mu_{\mathrm{dip}} = \sqrt{3c^3 I\dot{\Omega}/(2\Omega^3)} \approx 3.4 \times 10^{30}$ G cm^3, assuming $I \approx 10^{45}$ g cm^2 for the star's moment of inertia [1]. The corresponding dipole magnetic field is $B_d \equiv \mu_{\mathrm{dip}}/r_\star^3 = 3.4 \times 10^{12}(r_\star/10\,\mathrm{km})^{-3}$ G, where $r_\star$ is the neutron star radius. The spin-down power of Vela is given by

$$L_{\mathrm{sd}} = I\Omega\dot{\Omega} \approx 7 \times 10^{36}\ \mathrm{erg\ s^{-1}}. \tag{3.2}$$

The pulsed radio emission at frequencies around 1.4 GHz has a much smaller luminosity [1],

$$L_{\mathrm{GHz}} \approx 10^{28}\ \mathrm{erg\ s^{-1}}. \tag{3.3}$$

The observed bolometric luminosity of the pulsar is dominated by GeV gamma-rays from the outer magnetosphere [115],

$$L_{\mathrm{GeV}} \approx 8 \times 10^{34}\ \mathrm{erg\ s^{-1}}. \tag{3.4}$$

The apparent surface temperature of Vela (as measured by a distant observer) is $T_{\mathrm{s}}^{\infty} = (7.85 \pm 0.25) \times 10^5$ K [116]. It is related to the actual surface temperature T_{s} by $T_{\mathrm{s}}^{\infty} = T_{\mathrm{s}}\sqrt{1 - 2GM/r_\star c^2}$ [117]. We will use the approximate $T_{\mathrm{s}} \approx 10^6$ K.

3.2.2 Magnetosphere, Ocean, Crust, and Core

In the magnetosphere, the plasma mass density ρ satisfies $\rho c^2 \ll B^2/4\pi$, and so Alfvén waves propagate with almost the speed of light. This changes in the ocean where density $\rho > \rho_B \equiv B^2/4\pi c^2$,

$$\rho_B = 10^3 \left(\frac{B}{3.4 \times 10^{12}\,\mathrm{G}} \right)^2 \mathrm{~g~cm^{-3}}. \tag{3.5}$$

The ocean is an excellent thermal conductor, and is effectively isothermal in the deeper layers. According to the temperature profiles of [118] the ocean of a Vela-like pulsar with $T_\mathrm{s} = 10^6$ K has uniform temperature $T \sim 10^8$ K for densities $\rho \gtrsim 10^6$ g cm^{-3}, which is in agreement with the analytic formula of [119]. The solid-liquid phase transition, which defines the top of the crust, is set by the Coulomb parameter $\Gamma = Z^2e^2/ak_BT \approx 175$, where $a = (4\pi n_i/3)^{-1/3}$ is the mean inter-ion spacing [120]. This defines the crystallization density

$$\rho_\mathrm{crys} = 8 \times 10^7 \left(\frac{T}{10^8} \right)^3 \left(\frac{Z}{26} \right)^{-6} \left(\frac{A}{56} \right) \mathrm{~g~cm^{-3}}, \tag{3.6}$$

where A and Z are the ion mass and charge numbers. We adopt the value $\rho_\mathrm{crys} = 10^8$ g cm^{-3} for all of our numerical simulations.

The density profile of the neutron star $\rho(r)$ (where r is the radial coordinate) is obtained by integrating the equation of general relativistic hydrostatic equilibrium, using the SLy equation of state [121], with a central density $\rho = 10^{15}$ g cm^{-3}. We use the OPAL equation of state for the ocean with temperature $T = 10^8$ K [122]. We also make use of the analytical fitting formula in [123] for the crust and the ocean. This gives a neutron star with mass $M = 1.4 M_\odot$ and radius $r_\star = 11.69$ km.

For the SLy equation of state, there is a phase transition at the bottom of the crust that occurs at fixed pressure $P = 5.37 \times 10^{32}$ erg cm^{-3}. In our model, the crust-core boundary is located at

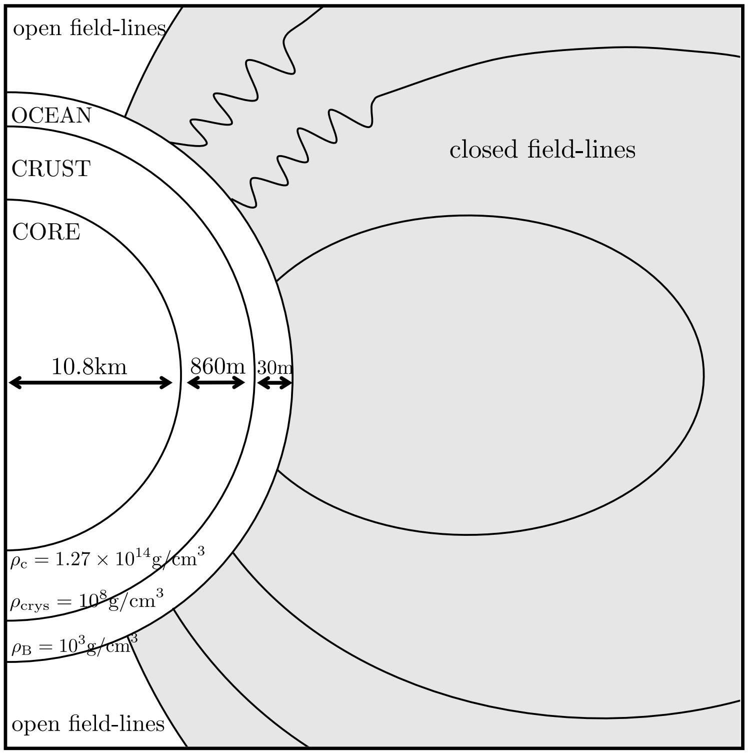
open field-lines
OCEAN
CRUST
CORE
closed field-lines
10.8km
860m
30m
$\rho_c = 1.27 \times 10^{14}$g/cm^3
$\rho_{crys} = 10^8$g/cm^3
$\rho_B = 10^3$g/cm^3
open field-lines

Figure 3.1: Schematic picture of the neutron star and its magnetosphere, indicating relevant length scales and characteristic densities. The gray shaded region represents the closed magnetosphere.

$r_c = 10.8$ km, with density

$$\rho_c = 1.27 \times 10^{14} \text{ g cm}^{-3}. \tag{3.7}$$

The neutron star structure is summarized in Figure 3.1. The crust-ocean boundary is located at radius $r_{\text{crys}} = 11.66$ km, and the thickness of the crust is $H \approx 860$ m. The mass of the crust is $M_c = 1.6 \times 10^{-2} M_\odot$. The ocean is ~ 30 m deep.

The speed of crustal shear waves is controlled by the shear modulus of the crustal lattice μ. At densities far above the crystallization density, μ is proportional to the Coulomb energy density of the lattice and is approximately given by $\mu \approx 0.12\, n_i (Ze)^2/a$ where $a \sim n_i^{-1/3}$ is the separation of the ion lattice with density n_i [124]. At densities ρ below the neutron drip density, $\rho_{\text{drip}} \approx 4 \times 10^{11}$ g cm^{-3}, it gives $\mu \propto \rho^{4/3}$. In the deeper crust μ scales almost linearly with ρ. The shear modulus has a sharp cutoff at density ρ_{crys}, so that $\mu = 0$ in the ocean.

The star's magnetic field is frozen in its core, crust, and ocean. In our axisymmetric numerical models, we assume that the magnetic field in the magnetosphere has a dipolar configuration aligned with the axis of rotation. We also need to include magnetic stresses inside the crust, when computing the transmission of the seismic waves into the magnetosphere. For computational simplicity we assume that the field inside the crust is that of a monopole, chosen so that the field at the surface equals 3×10^{12} G. The spherical symmetry of the background configuration dramatically speeds up the computation of crustal oscillations, because the vibrational eigenfunctions used in our spectral code are easily computed through the separation of angular and radial variables (see Section 5.2 for details).[1] An important feature of our model is that the magnetic field lines connecting the rotating star with the light cylinder are assumed to be open, and their footprints on the star form the two "polar caps." In the simplest case of a nearly aligned rotator, the angular size of the polar cap is $\theta_p \approx (r_\star/R_{\rm LC})^{1/2} \approx 0.05$.

3.3 Quake Excitation of Shear Waves

We model the quake as a sudden change in shear stress in the deep crust, which launches an elastic wave with an initial strain amplitude ϵ_0. The quake is triggered in a region of vertical thickness $\Delta\ell \sim 10^4$ cm (comparable to the hydrostatic pressure scale height) and horizontal area A_0. The energy of the quake is

$$E_Q \sim \frac{\mu\epsilon_0^2}{2}\,\Delta\ell A_0 \sim 10^{39}\left(\frac{\epsilon_0}{10^{-3}}\right)^2\left(\frac{A_0}{10^{11}\,\mathrm{cm}^2}\right)\ \mathrm{erg}. \tag{3.8}$$

The wave propagates toward the stellar surface with speed $v_s = (\mu/\rho)^{1/2} \approx 10^8$ cm s^{-1} and crosses the crust thickness $H \sim 10^5$ cm on the timescale

$$\tau \sim \frac{H}{v_s} \sim 1\ \mathrm{ms}. \tag{3.9}$$

---

[1] Replacing the dipole field with monopole below the stellar surface only slightly changes the crust dynamics and the calculated displacements of the magnetospheric footpoints. In the magnetosphere itself, the waves are followed in the correct dipole background. Had we kept the dipole field throughout, we would get similar results with a much greater computational effort.

The thickness of the shear layer sets the characteristic frequency of the generated waves. As a concrete example, consider the smooth deformation

$$\xi(z) = \frac{\xi_0}{2}\mathrm{erf}\left[\frac{\sqrt{2}(z - z_Q)}{\Delta\ell}\right], \tag{3.10}$$

where $z < 0$ is the distance below the stellar surface. It corresponds to a shear layer of thickness $\Delta\ell$ at depth z_Q. The characteristic length scale of the deformation is $\ell_0 \equiv \xi(d\xi/dz)^{-1} = \sqrt{\pi/8}\Delta\ell$. The characteristic angular frequency is

$$\omega \sim \frac{v_s}{\ell_0} \approx 2 \times 10^4 \left(\frac{\Delta\ell}{10^4\,\mathrm{cm}}\right)^{-1} \mathrm{rad\ s^{-1}}. \tag{3.11}$$

The quake can excite a broad spectrum of waves extending to frequencies well above this characteristic frequency.

3.3.1 One-dimensional Model of Waves

Much insight about the transmission of seismic waves into the magnetosphere and the core can be obtained from studying the propagation and transmission of radially directed seismic waves. A classic one-dimensional (1D) model of this type was developed by [110]. Following their approach, we approximated the crust as a 1D slab with the normal along the z-axis (which would be in the radial direction for a spherical crust). The shear displacement $\xi(z)$ is in the $\hat{y}$-direction. For the timescales of interest, the star is an ideal conductor, so the magnetic field is perturbed by the displacement along the y-axis, $B_y = B_z\partial\xi/\partial z$, as required by the flux-freezing condition. As a first approximation, the magnetosphere is also described by ideal MHD.

The magneto-elastic wave equation is given by

$$\tilde{\rho}\frac{\partial^2\xi}{\partial^2 t} = \frac{\partial}{\partial z}\left(\tilde{\mu}\frac{\partial\xi}{\partial z}\right), \tag{3.12}$$

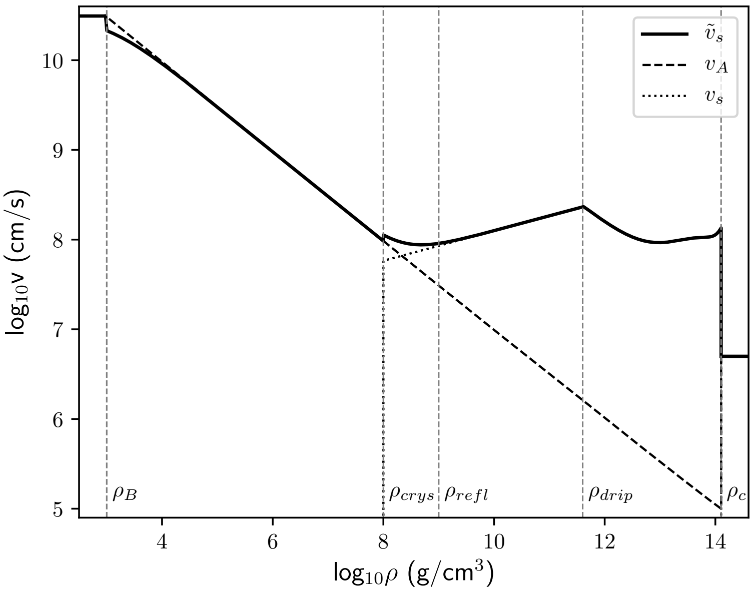

Figure 3.2: Wave speed $\tilde{v}_s(\rho)$ in the magnetosphere, ocean, crust, and core (thick black line). The dashed line shows the Alfén speed $v_A(\rho)$, and the dotted line shows the elastic wave speed $v_s(\rho)$.

where $\tilde{\rho}$ and $\tilde{\mu}$ are the effective mass density and shear modulus, respectively, such that

$$\tilde{\rho} = \rho + \frac{B_z^2}{4\pi c^2}, \qquad \tilde{\mu} = \mu + \frac{B_z^2}{4\pi}. \tag{3.13}$$

The wave speed is given by $\tilde{v}_s = (\tilde{\mu}/\tilde{\rho})^{1/2}$ and shown in Figure 3.2. It equals $v_s \approx 10^8$ cm s^{-1} in the deep crust and grows to the speed of light in the magnetosphere. The wave speed in the liquid core equals the Alfvén speed, which depends on B and the density of matter coupled to the Alfvén wave, as discussed in Section 3.3.3 below.

For a harmonic time dependence $\xi \propto e^{-i\omega t}$ with $\omega \gtrsim 10^4$ rad s^{-1} the wave propagation may be described in the WKB approximation. Then an upward propagating wave and its reflection from the low-density surface layers are given by [110]

$$\xi \propto \frac{1}{\sqrt{\rho \tilde{v}_s}} \left[e^{-i(u+\omega t)} + A_R e^{i(u-\omega t)} \right], \tag{3.14}$$

where

$$u \equiv -\int^z dz' \frac{\omega}{\tilde{v}_s}. \tag{3.15}$$

The first term in brackets in Equation (3.14) is the upward propagating wave, and the second term with the complex amplitude A_R is the reflected wave. The scaling of the overall amplitude $\xi \propto (\rho \tilde{v}_s)^{-1/2}$ comes from the conservation of energy flux in the wave $F \sim \rho v_s \omega^2 \xi^2$. In particular, using $\tilde{v}_s \propto \rho^{1/6}$ in the upper crust, one finds

$$\xi \propto \rho^{-7/12} \qquad (\rho < \rho_{\rm drip}), \tag{3.16}$$

and the strain in the shear wave is

$$\epsilon \equiv \frac{\partial \xi}{\partial z} = \frac{\xi \omega}{\tilde{v}_s} \propto \frac{1}{\rho^{1/2}\, \tilde{v}_s^{3/2}} \propto \rho^{-3/4}. \tag{3.17}$$

The strain can become large in the low-density regions and cause a secondary failure of the crust. However, in this work we choose to remain within the linear theory of elasticity, which is applicable in the limit of $\epsilon \ll 1$. In particular we assume that nowhere in the solid crust does the strain exceed the critical value $\epsilon_{\rm crit} \sim 0.1$ [125]. This condition is satisfied for a quake with a typical strain in the deep trigger region $\epsilon_0 < 2 \times 10^{-3}$. Our numerical models in Section 3.6 have the starquake area $A_0 \sim 3 \times 10^{11}$ cm^2, which gives the quake energy $E_Q \sim 10^{38}$ erg (Equation 3.8).

For waves excited on scales comparable to the hydrostatic scale height of the crust (as assumed in our quake scenario), the WKB approximation is not accurate, and the exact solution should be obtained numerically. More importantly, the 1D model is insufficient, as the quake waves propagate at different angles, and after reflection from the surface layers, they tend to spread sideways to fill the entire crust. The numerical simulations of this process are presented in Sections 3.5 and 3.6 below. Here we estimate the transmission coefficients analytically using the simple 1D model.

3.3.2 One-dimensional Wave Transmission into the Magnetosphere

The wave reflection occurs in the upper crust, which is defined by $\rho_{\rm drip} > \rho > \rho_{\rm crys}$. For a vertically propagating wave, the transmission coefficient (the ratio of transmitted to incident energy flux) is given by

$$\mathcal{T}_m = \frac{4Z_{\rm crust}Z_{\rm mag}}{(Z_{\rm crust}+Z_{\rm mag})^2} \approx \frac{4Z_{\rm mag}}{Z_{\rm crust}}, \tag{3.18}$$

where the impedance $Z = \tilde{v}_s\tilde{\rho}$ is evaluated in the upper crust at the transmission layer $\rho_{\rm refl}$, $Z_{\rm crust} \approx \rho_{\rm refl}\,\tilde{v}_s(\rho_{\rm refl})$, and in the magnetosphere, $Z_{\rm mag} \approx \rho_B c \ll Z_{\rm crust}$. In the relevant region, $\tilde{\rho} \approx \rho \gg \rho_B$, and the shear wave speed may be approximated as

$$\tilde{v}_s^2 \approx 10^{15}\left(7\rho_9^{1/3} + \frac{b^2}{\rho_9}\right)\frac{\rm cm^2}{\rm s^2}, \quad b = \frac{B}{3.4\times 10^{12}\,{\rm G}}, \tag{3.19}$$

where we normalized B to the characteristic dipole field of the Vela pulsar, and $\rho_9 = \rho/(10^9\ {\rm g\ cm^{-3}})$. Note that $\tilde{v}_s(\rho)$ is non-monotonic (see Figure 3.2). The wave speed first decreases from $v_s \approx 2\times 10^8$ cm s^{-1} in the deep crust to 9×10^7 cm s^{-1} at $\rho = 10^9$ g cm^{-3}. This decrease shortens the wavelength by a factor of ~ 2, so that it remains comparable to or shorter than the hydrostatic scale height. However, as ρ further decreases below 10^9 g cm^{-3}, the wave speed steeply grows, and the length scale of this change soon becomes shorter than the wavelength. Therefore, reflection mainly occurs at $\rho_{\rm refl}$ just below 10^9 g cm^{-3}. The reflection condition may be written as [110]

$$\left|\frac{d}{dz}\tilde{v}_s^2\right| \sim \omega\tilde{v}_s. \tag{3.20}$$

Pressure in the upper crust is dominated by relativistic degenerate electrons, and the hydrostatic balance gives the relation $|z| \approx 6 \times 10^3 \rho_9^{1/3}$ cm, where $z < 0$ is the depth below the stellar surface. Using this relation and Equation (3.19), we obtain the equation for $\rho_{\rm refl}$,

$$\left|1 - \frac{3b^2}{7\rho_9^{4/3}}\right| \sim \frac{\omega_4}{\sqrt{2}} \left(\rho_9^{1/3} + \frac{b^2}{7\rho_9}\right)^{1/2} . \tag{3.21}$$

At high frequencies one can keep only the second terms on both sides of the equation, which gives

$$\rho_{\rm refl} \approx 2 \times 10^9 \left(\frac{b}{\omega_4}\right)^{6/5} \frac{\rm g}{\rm cm^3} \qquad (\omega > \omega_{\rm eva}) . \tag{3.22}$$

One can show that the reflection condition (3.20) does not apply when $\omega < \omega_{\rm eva} \approx 2 \times 10^4$ rad s^{-1}. In that case, the reflection occurs deeper in the crust due to the appearance of an evanescent zone, and the transmission coefficient becomes suppressed as $(\omega/\omega_{\rm eva})^7$ (see [110]). Note also that at frequencies $\omega \lesssim v_s/H \approx 10^3$ rad s^{-1} the crust oscillates as a whole and directly moves the footprints of the magnetospheric field lines[2] .

Using Equation (3.22) for $\rho_{\rm refl}$ and the corresponding $\tilde{v}_s(\rho_{\rm refl}) \approx 3 \times 10^7\, b\, \rho_9^{-1/2}$ cm s^{-1}, we find[3]

$$\mathcal{T}_m \approx \begin{cases} 3 \times 10^{-3}\, b^{2/5}\, \omega_4^{3/5} & \left(\omega_{\rm eva} < \omega < \omega_{\rm crys}\right) \\ 10^{-2}\, b^2 & \left(\omega \geq \omega_{\rm crys}\right), \end{cases} \tag{3.23}$$

where $\omega_{\rm crys} \approx 10^5$ rad s^{-1} is the frequency at which the waves reflect near the crust-ocean interface, $\rho_{\rm refl}(\omega_{\rm crys}) = \rho_{\rm crys}$. All waves with frequency $\omega \geq \omega_{\rm crys}$ experience substantial reflection at the solid-liquid phase boundary (note the discontinuity in $\tilde{v}_s(\rho_{\rm crys})$ in Figure 3.2). The frequency independence of $\mathcal{T}_m$ at $\omega > \omega_{\rm crys}$ was not seen in [110] because they did not include the sharp phase transition at the top of the crust.

---

[2] The fundamental frequency of the liquid ocean is $\omega_{\rm ocean} = \tilde{v}_s/H_o \sim 3 \times 10^5$ rad s^{-1} where $H_o \sim 30$ m is the scale height of the ocean. For the characteristic frequency of the crustal oscillations $\omega \ll \omega_{\rm ocean}$, the ocean can be viewed as attached to the moving crust. Effectively, the waves are transmitted directly from the solid crust to the extended magnetosphere above the ocean.

[3] [110] obtained a different result $\mathcal{T}_m \propto B^{4/7}\omega^{3/7}$, because they considered neutron stars with lower $B = 10^{11}$ G. In that case, $\rho_{\rm refl}$ is much lower, and the hydrostatic stratification is different because the degenerate electrons are sub-relativistic.

A large fraction of the quake energy is deposited into waves with $\omega \gtrsim 2 \times 10^4$ rad s^{-1}, and these waves will leak into the magnetosphere with the above transmission coefficient.

3.3.3 Wave Transmission into the Core

The bottom of the crust is magnetically coupled to the liquid core. The core supports a multitude of MHD modes, which get excited while draining elastic wave energy from the crust [126]. The Alfvén crossing time of the core $\tau_A \sim r_\star/v_A \sim 1$ s is longer than the characteristic lifetime of crustal waves (estimated below). Effectively, the waves escape into the core as if it were an infinite reservoir. Under such conditions, the transmission coefficient for a vertically propagating shear wave at the crust-core interface can be estimated as

$$\mathcal{T}_c = \frac{4Z_{\rm crust}Z_{\rm core}}{(Z_{\rm crust} + Z_{\rm core})^2}, \tag{3.24}$$

where $Z_{\rm crust}$ and $Z_{\rm core}$ are the impedances of the crust and the outer core,

$$Z_{\rm crust} = \rho_> \tilde{v}_s, \qquad\qquad Z_{\rm core} = \rho_< v_A. \tag{3.25}$$

Here $\rho_>$ and $\rho_<$ are the mass densities of the matter that participate in the oscillations above and below the crust-core interface, respectively.

For typical pulsar parameters $Z_{\rm crust} \gg Z_{\rm core}$, and the transmission coefficient is

$$\mathcal{T}_c \simeq \frac{4Z_{\rm core}}{Z_{\rm crust}} = 4\frac{\rho_<}{\rho_>}\frac{v_A}{\tilde{v}_s}. \tag{3.26}$$

In the deep crust (below the neutron drip), a large fraction of mass is carried by free superfluid neutrons. However, entrainment is probably very strong, and we assume that free neutrons couple to shear waves, so that $\rho_>$ equals the total local density of the crust ρ [127].

By contrast, in the superfluid core neutrons become decoupled from the oscillations. Furthermore, as long as protons are superconducting, the magnetic flux is bunched into flux tubes with field $B_c \sim 10^{15}$ G. This causes two effects of superfluidity and superconductivity on wave transmission into the core:

i) The effective tension of magnetic field lines in the core is $BB_c/4\pi$. Therefore, bunching of the magnetic field into quantized flux tubes dramatically increases the magnetic tension, by a factor of $B_c/B \sim 300$. This enhances the transmission coefficient by a factor of ~ 20.

ii) Decoupling of protons from other species in the core reduces the effective mass density participating in the oscillation to the proton density, $\rho_< = \rho_p$.[4] This reduction of $\rho_<$ (by a factor of ~ 10) decreases the transmission coefficient by a factor ~ 3.

The net effect is an enhancement of the transmission coefficient $\mathcal{T}_c$, by a factor of ~ 6.

The Alfvén speed in the outer core is

$$v_A = \left(\frac{BB_c}{4\pi\rho_p}\right)^{1/2} \sim 5 \times 10^6 \,\mathrm{cm\ s^{-1}}, \tag{3.27}$$

and the resulting transmission coefficient is

$$\mathcal{T}_c \sim 2 \times 10^{-2}. \tag{3.28}$$

The transmitted waves are lost for the quake. Since $\mathcal{T}_c$ for the superconducting core is ~ 5 times greater than $\mathcal{T}_m$, the lifetime of crustal waves is controlled by their leakage to the core rather than to the magnetosphere. The characteristic lifetime is given by

$$\tau_{\mathrm{core}} = \frac{2\tau}{\mathcal{T}_c} \sim 100\,\mathrm{ms}. \tag{3.29}$$

---

[4] Even in the presence of strong vortex-flux-tube interactions, a negligible fraction of the neutron mass couples to the oscillations we are considering (see [128])

3.4 Magnetospheric Waves and Electric Discharge

3.4.1 Electric Current of Alfvén Waves

The magnetospheric disturbance may be described as ideal MHD Alfvén waves as long as there is enough plasma in the magnetosphere to support electric currents. The energy flux of the Alfvén waves into the magnetosphere is approximately given by

$$F_\star \sim \frac{E_Q \mathcal{T}_{\rm m}}{\tau A} \sim 4 \times 10^{26} \, \frac{E_{Q,38}}{A_{12}} \, \frac{\rm erg}{\rm s\,cm^2}, \tag{3.30}$$

where A is the area through which the crustal wave energy is leaking into the magnetosphere. Initially, at times comparable to $\tau = H/v_s \sim 1$ ms, the waves emerge from the quake area $A \approx A_0$. Later, A grows as the waves spread horizontally through the crust.

The Alfvén waves are ducted along the magnetic field lines, and their flux F changes proportionally to the local magnetic field B,

$$F = F_\star \, \frac{B}{B_\star}. \tag{3.31}$$

This fact follows from $F\,dS$ =const where $dS = d\psi/B$ is the cross-sectional area of a field-line bundle carrying infinitesimal magnetic flux $d\psi$. The flux F determines the wave amplitude δB,

$$\delta B \approx \left(\frac{8\pi F}{c}\right)^{1/2} \sim 3 \times 10^8 \, F_{26} \ {\rm G}. \tag{3.32}$$

The relative perturbation of the magnetic field is small near the star, $\delta B_\star / B_\star \approx 10^{-4} \, F_{\star,26}^{1/2}$. However, it grows for waves propagating to radii $r \gg r_\star$ in the outer magnetosphere as $\delta B/B \propto F^{1/2}/B \propto B^{-1/2}$. In particular, for a dipole magnetosphere, $B \propto r^{-3}$, and so

$$\frac{\delta B}{B} \approx 10^{-4} \, F_{\star,26}^{1/2} \left(\frac{r}{r_\star}\right)^{3/2}. \tag{3.33}$$

The emitted Alfvén waves bounce in the closed magnetosphere on the light-crossing timescale t_b and can accumulate energy and δB during the quake. This accumulation occurs on field lines that do not extend too far from the star, so that their t_b is shorter than the quake duration.

Alfvén waves can be thought of as the propagating shear of the magnetic field lines. They require electric current $j_{\|}$ along $\boldsymbol{B}$ as long as the wavevector $\boldsymbol{k}$ has a component perpendicular to $\boldsymbol{B}$, $k_\perp \neq 0$. This component is inevitably present, since the field lines are curved. The waves develop different phases on different field lines, and thus amplify the gradients of δB in the direction perpendicular to the field lines.

The electric current $j_{\|}$ may be estimated as [5]

$$j_{\|} \sim \frac{c}{4\pi} k_\perp \delta B \sim \frac{c}{4\pi} \frac{\delta B}{\ell_\perp}, \tag{3.34}$$

where $\ell_\perp \sim k_\perp^{-1}$ is the spatial scale of the wave variation perpendicular to $\boldsymbol{B}$. The length scale $\ell_\perp$ is initially determined by the elasto-dynamics of the crust. But once Alfvén waves on neighbouring field lines accumulate a difference in path length similar to the wavelength, they are effectively de-phased. Therefore, $\ell_\perp$ decreases, and so $j_{\|}$ grows as the Alfvén waves keep bouncing in the closed magnetosphere. The growth of $j_{\|}$ may be estimated as follows.

Let us consider a dipole magnetosphere and let θ be the polar angle measured from the dipole axis. It is convenient to label the field lines by the poloidal magnetic flux function,

$$\psi = \frac{\mu_{\rm dip} \sin^2\theta}{r}, \tag{3.35}$$

which is constant along a field line. In the axisymmetric magnetosphere, ψ =const on each flux surface formed by a field line rotated about the axis of symmetry. A closed field line with footprints on the star at $\theta_\star$ and $\pi - \theta_\star$ extends to radius $r_{\rm max} = r_\star/\sin^2\theta_\star$, and its length is $\sim 3r_{\rm max}$. The bounce cycle of Alfvén waves along a closed field line takes time $t_b \propto r_{\rm max} \propto \psi^{-1}$, so two field lines separated by a small $\Delta\psi$ have different t_b,

---

[5] In particular, in axisymmetry, $\delta\boldsymbol{B}$ is azimuthal, and its gradient is in the poloidal plane. This gradient has a component perpendicular to the background dipole field $\boldsymbol{B}$ and generates $\nabla \times \boldsymbol{\delta B} \parallel \boldsymbol{B}$.

$$\frac{\Delta t_b}{t_b} \approx -\frac{\Delta\psi}{\psi}. \tag{3.36}$$

After time t, the accumulated phase mismatch between waves on flux surfaces separated by $\Delta\psi$ is

$$\frac{\Delta\phi}{\omega t} \approx -\frac{\Delta\psi}{\psi}. \tag{3.37}$$

De-phasing on a given scale $\Delta\psi_{\rm de}$ occurs when $|\Delta\phi| \sim \pi$, and so $\Delta\psi_{\rm de}(t) \sim \pi\psi/\omega t$. At a radius $r > r_\star$, the distance $\ell_\perp$ between the poloidal field lines separated by $\Delta\psi_{\rm de}$ is

$$\ell_\perp(t) \approx r\,\frac{\Delta\psi_{\rm de}}{\partial\psi/\partial\theta} \sim \frac{\pi r\tan\theta}{2\omega t}. \tag{3.38}$$

This gives the current density (Equation 3.34)

$$j_{\|}(t) \sim \frac{c\,\delta B}{2\pi^2 r\tan\theta}\,\omega t. \tag{3.39}$$

3.4.2 $e^\pm$ Discharge

In the canonical pulsar picture, the rotating closed magnetosphere is filled with plasma that sustains the corotation electric field $\boldsymbol{E} = -\boldsymbol{v}\times\boldsymbol{B}/c$ (here $\boldsymbol{v} = \boldsymbol{\Omega}\times\boldsymbol{r}$). This implies the characteristic minimum plasma density [43],

$$n_{\rm GJ} = \frac{|\nabla\cdot\boldsymbol{E}|}{4\pi e} \approx \frac{|\boldsymbol{\Omega}\cdot\boldsymbol{B}|}{2\pi c e}. \tag{3.40}$$

The actual plasma density may be higher by a multiplicity factor $\mathcal{M}$, $n = \mathcal{M} n_{\rm GJ}$. This factor is believed to be large in the open field-line bundle, in some cases exceeding 10^3, because the open field lines are twisted and sustain continual $e^\pm$ discharge. The value of $\mathcal{M}$ in the closed magnetosphere is unknown and likely much lower, because this zone is not active and generates no discharge. It may, however contain $e^{\pm}$ pairs created by gamma-rays entering from the open field lines [52].

The existing plasma in the closed zone can sustain Alfvén waves with the maximal current

$$j_{\max} = ce\mathcal{M}n_{\mathrm{GJ}} = \frac{\mathcal{M}\,|\boldsymbol{\Omega}\cdot\boldsymbol{B}|}{2\pi}. \tag{3.41}$$

When $j_{\parallel}$ exceeds $j_{\max}$, the waves become charge starved, and the ideal MHD approximation must break [110]. From Equations (3.33), (3.39), and (3.41), we find

$$\frac{j_{\parallel}}{j_{\max}} \sim \frac{c\,(\delta B/B)\,\omega t}{4\pi^2\mathcal{M}\,\Omega\,r\tan\theta} \sim 10\,\frac{\omega_4}{\mathcal{M}\tan\theta}\left(\frac{\delta B_\star/B_\star}{10^{-4}}\right)\left(\frac{r}{r_\star}\right)^{1/2}\left(\frac{t}{0.1\,\mathrm{s}}\right). \tag{3.42}$$

One can see that the Alfvén waves generated by the quake can become charge-starved, especially when one takes into account the growth of $\delta B_\star$ due to the accumulation of waves trapped in the closed magnetosphere.

Once charge starvation is reached, a parallel electric field will be induced to support $\nabla\times\boldsymbol{B}$. The resulting parallel voltage may be estimated as

$$\Phi \sim \frac{4\pi j_{\parallel}}{c}\ell_{\perp}^2 \sim \delta B\,\ell_{\perp}. \tag{3.43}$$

The voltage is maximum for the largest $\ell_{\perp}$ at which starvation occurs. This scale $\ell_{\perp}$ is given by the condition

$$\frac{\delta B}{\ell_{\perp}} \sim 4\pi\mathcal{M}\rho_{\mathrm{GJ}}, \tag{3.44}$$

which yields

$$\Phi \sim \frac{c(\delta B)^2}{2\mathcal{M}\Omega B} = \frac{4\pi F}{\mathcal{M}\Omega B}. \tag{3.45}$$

Note that F/B =const (Equation 3.31), so the generated voltage is approximately the same at all r

along the field line and can be estimated with $F = F_\star$ and $B = B_\star$. This gives

$$\frac{e\Phi}{m_e c^2} \sim 3 \times 10^9 \, \mathcal{M}^{-1} \, F_{\star,26}. \tag{3.46}$$

This voltage exceeds the threshold for $e^\pm$ discharge, as particle acceleration to $\gamma \sim 10^6 - 10^7$ is sufficient to ignite $e^\pm$ creation by emitting high-energy curvature photons [44]. This process will flood the magnetosphere and the open field-line bundle with $e^\pm$ plasma. Therefore, the quake should be capable of interrupting the normal radio pulsations of Vela.

3.5 Setup of the Numerical Simulation

In this section, we outline the formalism and the setup of our numerical simulations. We are able to simulate the elasto-dynamics of the crust in 3D; however we are currently limited to the 2D axisymmetric simulations of the magnetosphere. Since the two computations are coupled, we are restricting ourselves to the 2D axisymmetric simulations of the whole system.

3.5.1 Dynamics of the Crust

We use the linearized equations of motion (see, e.g. [84], [110]). For simplicity, the background state of the crust is assumed to have a potential magnetic field, $\nabla \times \boldsymbol{B} = 0$ and $\boldsymbol{j} = 0$. The background is static and has $\boldsymbol{E} = 0$. A displacement $\boldsymbol{\xi}(t,\boldsymbol{r})$ creates motion with velocity $\dot{\boldsymbol{\xi}} = d\boldsymbol{\xi}/dt \approx \partial\boldsymbol{\xi}/\partial t$ in the linear order. The momentum and continuity equations are

$$\rho\ddot{\boldsymbol{\xi}} = \nabla \cdot \boldsymbol{\sigma} + \frac{1}{c}\delta\boldsymbol{j} \times \boldsymbol{B} + \boldsymbol{g}\,\delta\rho - \nabla\delta p, \tag{3.47}$$

$$\delta\rho = -\nabla \cdot (\rho\boldsymbol{\xi}), \tag{3.48}$$

where $\boldsymbol{\sigma}$ is the elastic stress tensor of the crustal Coulomb lattice, $\boldsymbol{g}$ is the gravitational acceleration, and p is the pressure; perturbations are denoted by δ. The quake waves involve a fraction of the Coulomb energy density of the lattice, which is much smaller than the hydrostatic pressure.

Therefore, compressive motions and radial displacements are negligible, and hereafter we consider only solenoidal deformations ($\nabla \cdot \boldsymbol{\xi} = 0$) and set $\xi_r = 0$. In this model, $\delta\rho = 0$, $\delta p = 0$, and the density of the crust is spherically symmetric.

The stress tensor for an isotropic and incompressible solid is [129],

$$\sigma_{ij} = \mu \left(\frac{\partial \xi_i}{\partial x_j} + \frac{\partial \xi_j}{\partial x_i} \right), \tag{3.49}$$

where μ is the crustal shear modulus. The linear theory of elasticity is applicable in the limit of small strain.

For the short timescales considered in this problem, the crust is effectively an ideal conductor. In the conductor rest frame, which is moving with velocity $\dot{\boldsymbol{\xi}}$, the electric field must vanish,

$$\delta \boldsymbol{E} + \frac{\dot{\boldsymbol{\xi}} \times \boldsymbol{B}}{c} = 0. \tag{3.50}$$

Then the induction equation $\partial \boldsymbol{B}/\partial t = -c\nabla \times \boldsymbol{E}$ gives

$$\delta \boldsymbol{B} = \nabla \times (\boldsymbol{\xi} \times \boldsymbol{B}). \tag{3.51}$$

The excited electric current $\delta \boldsymbol{j}$ is related to $\delta \boldsymbol{B}$ and $\delta \boldsymbol{E}$ by the Maxwell equation,

$$\frac{4\pi}{c} \delta \boldsymbol{j} = \nabla \times \delta \boldsymbol{B} - \frac{1}{c} \frac{\partial \delta \boldsymbol{E}}{\partial t} = \nabla \times \nabla \times (\boldsymbol{\xi} \times \boldsymbol{B}) + \frac{1}{c^2} \ddot{\boldsymbol{\xi}} \times \boldsymbol{B}. \tag{3.52}$$

Substitution of Equations (3.49) and (3.52) into Equation (3.47) gives the elasto-dynamic wave equation,

$$\rho \ddot{\boldsymbol{\xi}} + \rho_B \ddot{\boldsymbol{\xi}}_\perp = (\nabla \mu \cdot \nabla) \boldsymbol{\xi} - (\boldsymbol{\xi} \cdot \nabla) \nabla \mu + \mu \nabla^2 \boldsymbol{\xi} + \frac{1}{4\pi} [\nabla \times \nabla \times (\boldsymbol{\xi} \times \boldsymbol{B})] \times \boldsymbol{B}, \tag{3.53}$$

where $\rho_B = B^2/4\pi c^2$ and $\boldsymbol{\xi}_\perp$ is the displacement perpendicular to $\boldsymbol{B}$. In the crust, Equation (3.53) describes oscillations of the magnetized solid. In the liquid ocean, $\mu \longrightarrow 0$ and Equation (3.53) describes pure Alfvén waves. The dynamics of the crust and the ocean of interest occurs at densities $\rho \gg \rho_B \sim 10^3$ g cm^{-3} where the term $\rho_B \ddot{\boldsymbol{\xi}}_\perp$ can be neglected.

3.5.2 Spectral Method

In order to numerically solve Equation (3.53), we prefer to use a spectral method for superior stability and accuracy over a large range of densities. Our formalism follows closely that of [130]. Equation (3.53) is written in the form

$$\frac{\partial^2 \boldsymbol{\xi}}{\partial t^2} = \hat{\mathcal{L}}(\boldsymbol{\xi}) = \hat{\mathcal{L}}_{\rm el}(\boldsymbol{\xi}) + \hat{\mathcal{L}}_{\rm mag}(\boldsymbol{\xi}), \tag{3.54}$$

where the linear differential operators $\hat{\mathcal{L}}_{\rm el}$ and $\hat{\mathcal{L}}_{\rm mag}$ give the acceleration due to elastic and magnetic forces, respectively. The elastic acceleration is

$$\hat{\mathcal{L}}_{\rm el}(\boldsymbol{\xi}) = \frac{1}{\rho}\left[(\nabla\mu \cdot \nabla)\boldsymbol{\xi} - (\boldsymbol{\xi} \cdot \nabla)\nabla\mu + \mu\nabla^2\boldsymbol{\xi}\right]. \tag{3.55}$$

The operator $\hat{\mathcal{L}}_{\rm mag}$ is greatly simplified by approximating the crustal magnetic field as purely radial (a monopole) with $B_r = B_0(r_\star/r)^2$, where B_0 is the typical magnetic field strength in the crust. In reality B_r varies over the crust. We use the fiducial value of $B_0 = 3 \times 10^{12}$ G. The magnetic acceleration is then

$$\hat{\mathcal{L}}_{\rm mag} = \frac{1}{4\pi\rho}[\nabla \times \nabla \times (\boldsymbol{\xi} \times \boldsymbol{B})] \times \boldsymbol{B} = r\frac{\mu_B}{\rho}\frac{\partial^2}{\partial r^2}\left(\frac{\boldsymbol{\xi}}{r}\right), \tag{3.56}$$

where $\mu_B \equiv B_r^2/4\pi$ depends only on r. We use spherical coordinates r, θ, and ϕ.

We separate variables t, r, θ, and ϕ in Equation (3.54), and define magneto-elastic modes $\boldsymbol{\xi}_{nlm}$ as the eigenfunctions of the operator $\hat{\mathcal{L}}$ with the boundary conditions of zero stress at the boundaries (free oscillations of the system),

$$\hat{\mathcal{L}}(\boldsymbol{\xi}_{nlm}) = -\omega_{nlm}^2\boldsymbol{\xi}_{nlm}. \tag{3.57}$$

Here ω_{nlm} is the eigenfrequency of the mode with radial, polar, and azimuthal numbers n, l, and

m, respectively. The modes $\boldsymbol{\xi}_{nlm}(\boldsymbol{r})$ form an orthogonal basis for a Hilbert space with the inner product

$$\langle \boldsymbol{\eta}, \boldsymbol{\beta} \rangle = \int_{\mathcal{V}} \rho \boldsymbol{\eta} \cdot \boldsymbol{\beta} \, d^3 \boldsymbol{r}, \tag{3.58}$$

where $\boldsymbol{\eta}$ and $\boldsymbol{\beta}$ are arbitrary vector functions defined over the volume of the crust $\mathcal{V}$. Therefore, an arbitrary solenoidal displacement field of the crust $\boldsymbol{\xi}(\boldsymbol{r}, t)$ may be decomposed as

$$\boldsymbol{\xi}(\boldsymbol{r}, t) = \sum_{n,l,m} a_{nlm}(t) \boldsymbol{\xi}_{nlm}(\boldsymbol{r}), \tag{3.59}$$

where

$$a_{nlm}(t) = \frac{\langle \boldsymbol{\xi}(\boldsymbol{r}, t), \boldsymbol{\xi}_{nlm} \rangle}{\langle \boldsymbol{\xi}_{nlm}, \boldsymbol{\xi}_{nlm} \rangle}. \tag{3.60}$$

Effectively, the spectral method replaces the crust with many oscillators. Equation (3.54) describes free oscillations, with no external forces, and is reduced to $\ddot{a}_{nlm}(t) + \omega_{nlm}^2 a_{nlm}(t) = 0$. In the presence of magnetic coupling to the magnetosphere/core, external forces $\boldsymbol{f}_{\rm mag}$ and $\boldsymbol{f}_{\rm core}$ appear at the upper/lower boundaries of the crust,

$$\boldsymbol{f}_{\rm ext} = \boldsymbol{f}_{\rm mag} + \boldsymbol{f}_{\rm core}. \tag{3.61}$$

Then each oscillator is driven by the projection of the external force on the eigenmode,

$$\ddot{a}_{nlm}(t) + \omega_{nlm}^2 a_{nlm}(t) = \frac{\langle \boldsymbol{f}_{\rm ext}(\boldsymbol{r}, t), \boldsymbol{\xi}_{nlm} \rangle}{\langle \boldsymbol{\xi}_{nlm}, \boldsymbol{\xi}_{nlm} \rangle}. \tag{3.62}$$

The initial conditions $a_{nlm}(t = 0)$ are determined by the initial displacement $\boldsymbol{\xi}_0$ and Equation (3.60). We then evolve the spectral coefficients a_{nlm}, our effective dynamical variables, using Equation (3.62).

3.5.3 Basis Functions

For the class of solenoidal displacements we are considering, and the above operators, the natural choice of basis functions is

$$\boldsymbol{\xi}_{nlm} = \zeta_{nl}(r)\boldsymbol{r} \times \nabla Y_{lm}, \tag{3.63}$$

where ζ_{nl} contains the radial part of the eigenfunction, and $\boldsymbol{r} \times \nabla Y_{lm}$ is the third vector spherical harmonic. Substitution of Equation (3.63) into Equation (3.54) results in the following Sturm-Liouville problem:

$$-\omega_{nl}^2 \rho \zeta_{nl} = \frac{d\tilde{\mu}}{dr}\left(\frac{d\zeta_{nl}}{dr} - \frac{\zeta_{nl}}{r}\right) + \frac{\tilde{\mu}}{r^2}\frac{d}{dr}\left(r^2\frac{d\zeta_{nl}}{dr}\right) - [l(l+1)\mu + 2\mu_B]\frac{\zeta_{nl}}{r^2}, \tag{3.64}$$

The radial eigenfunctions $\zeta_{nl}(r)$ and eigenvalues $\omega_{nlm} = \omega_{nl}$ do not depend on the azimuthal mode number m due to the spherical symmetry of $\tilde{\mu}$. Note that in the limit $\mu_B \to 0$ Equation (3.64) is the same as Equation (23) in [84].

We use a high-order Sturm-Liouville solver to numerically find the eigenfunctions and eigenvalues of Equation (3.64). The details are given in Appendix C.

3.5.4 Coupling to the Core

The magnetic field is frozen in the crust and the liquid core, and so crustal oscillations deform the magnetic field lines and launch Alfvén waves into the core. The feedback of these waves on the crust dynamics is incorporated in our simulations as follows.

For simplicity, we approximate the background magnetic field $\boldsymbol{B}$ as purely radial so that $B = B_r$. Since the core is effectively an infinite reservoir on the quake timescale (Section 3.3.3), there are only inward propagating waves with the displacement of the form $\boldsymbol{\xi}(t + r/v_A)$, where v_A is the Alfvén speed in the core. The magnetic field of the emitted waves is related to the displacement $\boldsymbol{\xi}$

by the flux-freezing condition,

$$\delta \boldsymbol{B}_< = \nabla \times (\boldsymbol{\xi} \times \boldsymbol{B}) = \frac{1}{r}\,\partial_r(B_r r\,\boldsymbol{\xi}) \approx B_r \partial_r \boldsymbol{\xi} = \frac{B_r}{v_A}\,\dot{\boldsymbol{\xi}}. \tag{3.65}$$

Here subscript "<" stands for the core region immediately below the crust, and $\dot{\boldsymbol{\xi}}$ is the time derivative of the displacement at the interface.

The presence of $\delta \boldsymbol{B}_<$ implies that the core applies Maxwell stress to the bottom of the crust. The extracted momentum flux is

$$\sigma_{rh} = -\frac{B_r\,\delta B_{h,<}}{4\pi}, \tag{3.66}$$

where $h = \theta, \phi$ labels the horizontal component. Since the crustal modes are calculated with the stress-free boundary condition $\delta \boldsymbol{B} = 0$, the external stress must be included as a driving term in the oscillation Equation (3.62). The external force appearing in this equation is applied to the bottom layer of the crust of some thickness Δr and density $\rho_>$ (just above the interface), so that $f_{\rm ext}\rho_> \approx \sigma_{rh}/\Delta r$. Approximating the layer as infinitesimally thin, the external force at the crust-core interface becomes

$$\boldsymbol{f}_{\rm core} = -\frac{B_r\,\delta \boldsymbol{B}_<}{4\pi\rho_>}\,\delta(r - r_c). \tag{3.67}$$

Substituting the core Afvén speed $v_A = B_r/(4\pi\rho_<)^{1/2}$, we obtain

$$\boldsymbol{f}_{\rm core} = -\frac{\rho_<}{\rho_>}\,v_A\,\dot{\boldsymbol{\xi}}\,\delta(r - r_c), \tag{3.68}$$

where $\rho_<$ is the mass density of the core infinitesimally below the crust-core interface. One can see that coupling to the core is equivalent to adding a damping force $\propto \dot{\boldsymbol{\xi}}$.

The projection of $\boldsymbol{f}_{\rm core}$ onto each basis function is computed once at the beginning of the simulation and stored in an array (see Appendix D).

3.5.5 Coupling to the Magnetosphere

In this work, we model the pulsar magnetosphere as dipole, and treat the magnetospheric waves as linear perturbations, using the framework of force-free electrodynamics. In force-free electrodynamics the inertia of the plasma is negligible compared to the inertia of the magnetic field, and the equation of motion is replaced by the condition

$$\rho_{\mathrm{e}}\boldsymbol{E} + \frac{\boldsymbol{j}\times\boldsymbol{B}}{c} = 0. \tag{3.69}$$

It implies $\boldsymbol{E}\cdot\boldsymbol{B} = 0$ and $\boldsymbol{E}\cdot\boldsymbol{j} = 0$, so there is no dissipation. This approximation is valid if there is enough plasma to sustain electric currents excited in the perturbed magnetosphere. For linear perturbations about a stationary background state with $\boldsymbol{E} = 0$ (in the corotating frame) and $\nabla\times\boldsymbol{B} = 0$ the force-free condition becomes $\delta\boldsymbol{j}\times\boldsymbol{B} = 0$. Substitution of $\delta\boldsymbol{j}$ from Equation (3.52) then gives

$$\rho_B\ddot{\boldsymbol{\xi}}_\perp = \frac{1}{4\pi}[\nabla\times\nabla\times(\boldsymbol{\xi}\times\boldsymbol{B})]\times\boldsymbol{B}. \tag{3.70}$$

Note that only the perpendicular displacement $\boldsymbol{\xi} = \boldsymbol{\xi}_\perp$ enters the force-free wave equation.

The wave equation gives the dispersion relation for eigen modes $\boldsymbol{\xi} \propto \exp(-i\omega t + \boldsymbol{k}\cdot\boldsymbol{r})$,

$$\frac{\omega^2}{c^2}\boldsymbol{\xi} = k_\parallel^2\boldsymbol{\xi} + \boldsymbol{k}_\perp(\boldsymbol{k}\cdot\boldsymbol{\xi}), \tag{3.71}$$

where $k_\parallel$ and $\boldsymbol{k}_\perp$ are the components of $\boldsymbol{k}$ parallel and perpendicular to $\boldsymbol{B}$, respectively. The eigen modes include shear Alfvén waves ($\boldsymbol{k}\cdot\boldsymbol{\xi} = 0$) with dispersion relation $\omega = k_\parallel c$, and compressive (called “fast”) modes. The perturbations are generated by the shear motions of the crust at the footprints of the magnetospheric field lines, and these motions should launch Alfvén waves. Their conversion to fast modes in the magnetosphere is a second-order effect, which is negligible as long as $\delta B/B \ll 1$.

The group speed of Alfvén waves is parallel to $\boldsymbol{B}$, so they are ducted along the magnetic field lines. For the linear dynamics of Equation (3.70), each poloidal field line behaves like an independent string, with no coupling to other field lines. Then effectively we need to solve a 1D wave equation along each poloidal field line.

In axisymmetry, $\partial/\partial\phi = 0$, the Alfvén waves have the displacement in the ϕ-direction, $\boldsymbol{\xi} = \xi_\phi \hat{\boldsymbol{\phi}}$. It is convenient to work in the so-called magnetic flux coordinates (ψ, χ, ϕ). The coordinate ψ represents surfaces of constant poloidal flux (for a dipole magnetosphere it is given by Equation (3.35)), and χ is the length along poloidal field lines in the $\phi = \text{const}$ plane [88]. Equation (3.70) can be written in the flux coordinates as

$$\frac{\partial^2 \xi_\phi(\psi,\chi)}{\partial t^2} = \frac{c^2}{r_\perp B}\frac{\partial}{\partial\chi}\left[r_\perp^2 B \frac{\partial}{\partial\chi}\left(\frac{\xi_\phi(\psi,\chi)}{r_\perp}\right)\right], \tag{3.72}$$

where $r_\perp = r\sin\theta$ is the cylindrical radius. Each flux surface in the magnetosphere is effectively a 1D string (with mass density and tension both proportional to $Br_\perp$) supporting shear wave propagation with speed c.

Between the solid crust and the force-free magnetosphere there is the liquid ocean. The ocean dynamics can be calculated by extending the magnetosphere model so that each 1D string includes a heavy part at the footprint where the string mass density is increased and the shear wave is decelerated below c as $v_A/c = (\rho/\rho_B + 1)^{-1/2}$. The technical motivation for treating the ocean motions as part of the magnetospheric dynamics is that it is liquid and hence "force-free" — it does not sustain any shear forces. Note however that the ocean depth is small compared with the crust thickness, and at wave frequencies of interest, it moves together with the crust at the footprints of the magnetospheric field lines. Effectively, the magnetosphere is attached to the solid crust, and in the numerical models presented in Section 3.6 the presence of the ocean will be neglected. We also performed more detailed simulations with ocean dynamics included, which support this approximation for Vela.

Solving the magnetospheric field-line dynamics requires two boundary conditions. For closed field lines, the boundary conditions are applied at the two footpoints where the field line intersects with the surface of the neutron star. The field line is attached to the star and its footprint displacement equals the instantaneous displacement of the uppermost layer of the crust, $\boldsymbol{\xi}(t, r_\star)$, which is determined by Equation (3.62).

For open field lines, only one end is attached to the star, giving one boundary condition $\boldsymbol{\xi}(r_\star)$. The other end is at the outer boundary of the computational domain. At this end, we apply the condition of free escape, which means that there are only outgoing Alfvén waves. Outgoing waves are functions of $t - \chi/c$ and satisfy the condition

$$\left.\frac{\partial \boldsymbol{\xi}}{\partial \chi}\right|_{\chi_{\rm end}} = -\frac{1}{c}\left.\frac{\partial \boldsymbol{\xi}}{\partial t}\right|_{\chi_{\rm end}}, \tag{3.73}$$

In our simulations, the magnetosphere is sampled with 275 closed and 50 open flux surfaces. The outer boundary of the open field lines is set at $r_{\rm max} = 10^7$ cm, and the last closed field line extends to $R_{\rm LC} = 4.2 \times 10^8$ cm — the light cylinder radius of Vela. We follow the dynamics of each field line by solving the string Equation (3.72) with the boundary condition $\xi(r_\star)$ at the footprints and Equation (3.73) at the outer boundary. The magnetospheric dynamics is coupled to the crustal oscillations at $r_\star$, so the crust and the magnetosphere evolve together as a coupled system. The coupled differential Equations (3.62) and (3.72) are integrated numerically using the fourth-order Runge-Kutta scheme, as described in Appendices D and E.

The feedback of the emitted magnetospheric waves on the crust oscillations is implemented similarly to the crust-core interaction described in Section 3.5.4. In the axisymmetric model, both the displacement and the perturbed magnetic field are in the ϕ-direction. Let $\delta B = B_{\phi,>}$ be the perturbed field immediately above the stellar surface. The magnetospheric stress $B_r B_{\phi,>}/4\pi$ is communicated directly to the solid crust at the bottom of the ocean, where density $\rho = \rho_{\rm crys}$. To extract the required momentum flux $\sigma_{r\phi} = -B_r B_{\phi,>}/4\pi$ from the crust, we apply force $f_{\rm mag} = -(\sigma_{r\phi}/\rho_{\rm cryst}\Delta r)$ to the upper layer of the solid material with a small thickness Δr,

$$\boldsymbol{f}_{\rm mag} \approx \frac{B_r\, \delta \boldsymbol{B}_>}{4\pi \rho_{\rm crys}}\, \delta(r - r_{\rm crys}). \tag{3.74}$$

The magnetospheric perturbation B_ϕ is related to the displacement $\xi_\phi(\psi, \chi)$ by the flux-freezing condition,

$$\delta B_\phi = B r_\perp \frac{\partial}{\partial \chi}\left(\frac{\xi_\phi}{r_\perp}\right). \tag{3.75}$$

This allows one to express $\boldsymbol{f}_{\rm mag}$ in the form

$$f^{\phi}_{\rm mag} = \frac{\rho(r_>)}{\rho_{\rm crys}} v_A^2(r_>) \cos\alpha \; r_\perp \frac{\partial}{\partial \chi}\left(\frac{\xi_\phi}{r_\perp}\right)\bigg|_{r_>} \delta(r - r_\star), \tag{3.76}$$

where α is the angle between the magnetic flux surface and the radial direction. In the model where the magnetosphere is directly attached to the solid crust (neglecting the thin ocean), $v_A(r_>) = c$ and $\rho(r_>) = \rho_B$. This approximation is used in the simulations presented below. A more detailed model of magnetospheric waves with the ocean at the footprints would have $v_A(r_>) \approx B/(4\pi\rho_{\rm crys})^{1/2} \approx 10^{-2}c$ and $\rho(r_>) = \rho_{\rm crys}$. It would explicitly follow the wave acceleration to c as it crosses the ocean.

3.6 Sample Models

We have calculated four sample models: A1, B1, and A2, B2. Their parameters are given in Table 3.1, and the initial displacement of the disturbed crust is shown Figure 3.3. In all the models, the quake has energy $E_Q = 10^{38}$ erg.

Models A1 and B1 have no crust-core coupling, representing a pulsar with a magnetic field confined to the crust and not penetrating the core. Models A2 and B2 have strong crust-core coupling; they assume a superconducting core, and the poloidal component of the magnetic field at the crust-core interface $B \approx 3.4 \times 10^{12}$ G, similar to the measured surface dipole field of Vela.

The dynamical picture of quake development is quite similar in all four models. As an example, the snapshots of model A1 are shown in Figures 3.4 and 3.5. At the beginning, we observe shear waves propagating toward the surface and launching Alfvén waves into the magnetosphere directly above the quake region (which is at the north polar cap in model A1). Due to the large impedance mismatch at both the crust-core and the crust-magnetosphere interfaces, most of the quake energy remains trapped inside the crust, and the waves bounce many times between the two

Table 3.1: Sample models.

Model	Quake Location	Core	Core v_A	$\rho_</\rho_>$	ϵ_0	A_0	E_Q
A1	Polar cap	Decoupled	—	—	4.4×10^{-4}	3×10^{11} cm^2	10^{38} erg
A2	Polar cap	Superconducting	5×10^6 cm s^{-1}	0.1	4.4×10^{-4}	3×10^{11} cm^2	10^{38} erg
B1	$\theta = \pi/4$	Decoupled	—	—	1.3×10^{-4}	1×10^{12} cm^2	10^{38} erg
B2	$\theta = \pi/4$	Superconducting	5×10^6 cm s^{-1}	0.1	1.3×10^{-4}	1×10^{12} cm^2	10^{38} erg

interfaces. Some waves are launched in the $\hat{\theta}$-direction with a large surface amplitude and cross the circumference of the crust in a time $\pi r_\star/\tilde{v}_s \sim 30\,\mathrm{ms}$. These surface waves are the so-called “whispering gallery modes" [131]. However, most of the shear wave energy remains concentrated at the north pole for a longer time, and gradually spreads toward the south pole after many small angle reflections at the interfaces. As the centroid of the shear wave energy passes the magnetic equator the luminosity of Alfvén waves into the magnetosphere, L_A, drops because B_r is small. After $\sim$ 200 ms the wave energy has spread throughout the entire crust, and the same luminosity of Alfvén waves is measured from the north and south poles. The evolution of L_A is shown in Figure 3.8.

The magnetospheric Alfvén waves are initially coherent when launched from the surface (Figure 3.4, top right), with the perpendicular length scale determined by the length of the elastic waves in the crust. After a light-crossing time ($\sim$ 45 ms for the last closed field-line) all of the Alfvén waves become de-phased (Figure 3.5, top right). The regions where $|j_\parallel/c\rho_\mathrm{GJ}| > 1$ are mapped in Figures 3.4 and 3.5. We find that avoiding charge starvation and the ignition of $e^\pm$ discharge requires the magnetospheric plasma to have a high multiplicity $\mathcal{M} \gtrsim 10^3$, in agreement with the estimates in Section 3.4.2. After three rotations of Vela, L_A has dropped by a factor of $\sim 2-3$. Less than 3% of the quake energy E_Q has been transferred to the magnetosphere (Figure 3.9).

The dynamics in model B1 is the same except that the elastic waves spread from a different quake region, now located at latitude $\theta \sim \pi/4$ instead of the north pole (Figures 3.6 and 3.7). The energy budget and the timescale for injecting the Alfvén waves into the magnetosphere are similar to those in model A1. At first, Alfvén waves are only launched into the closed field-lines (Figure 3.6), but after $\sim$ 20 ms the crustal shear waves have spread to the north polar cap, and Alfvén waves are launched into the north open field-line bundle, and the entire closed magnetosphere. Their luminosity L_A remains quite constant for the remainder of the simulation. After 3 rotations of Vela, $\sim$ 3% of the initial elastic energy has been transmitted into the magnetosphere.

Models A2 and B2, which include the crust-core coupling, show a significant difference from models A1 and B1: the lifetime of crustal waves is significantly reduced, because the wave energy

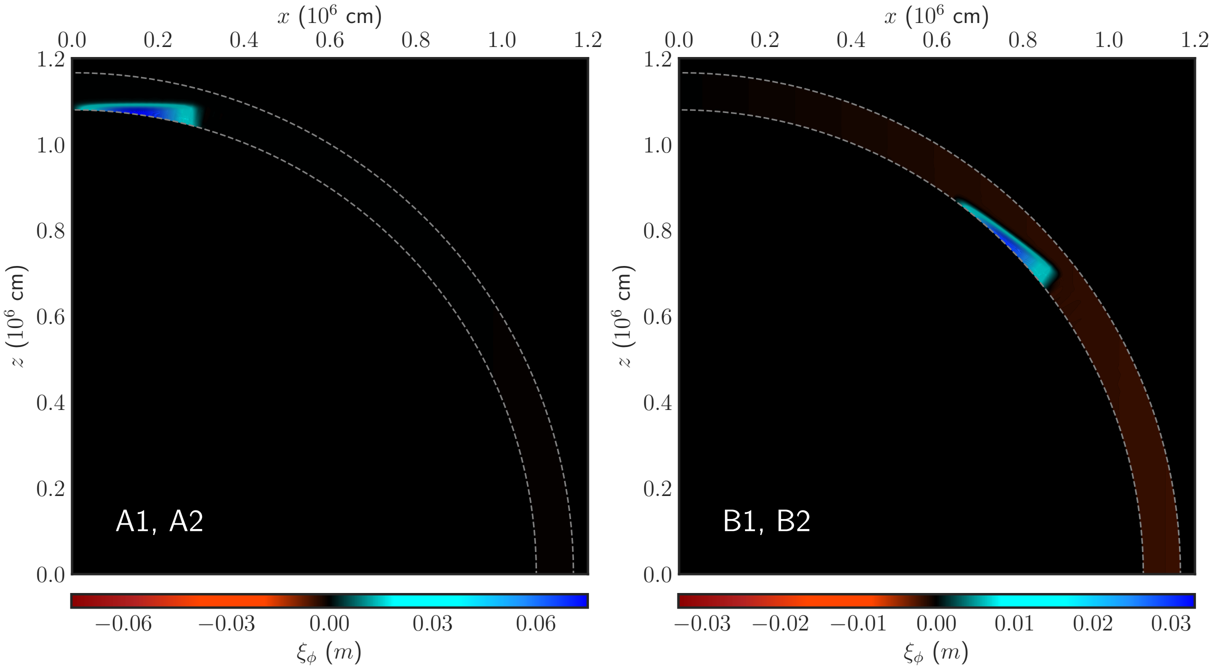

Figure 3.3: Top: initial conditions used for models A1 and A2. Bottom: initial conditions used for models B1 and B2. Color shows the amplitude of the azimuthal displacement ξ_ϕ. The amplitude is scaled so that each initial condition has the initial energy $E = 10^{38}$ erg. The gray dashed lines show the boundaries of the crust.

is drained into the core. This draining occurs exponentially, because it results from the damping force $f_{\rm core} \propto \dot{\xi}$ (Equation 3.68). The evolution of the crustal wave energy is well approximated by

$$E_{\rm crust} \approx E_Q \exp\left(-\frac{t}{\tau_{\rm core}}\right), \tag{3.77}$$

with $\tau_{\rm core} \approx 86\,{\rm ms}$ in both models A2 and B2 (Figure 3.9). The luminosity of Alfvén waves into the magnetosphere $L_{\rm A}$ decays on the same characteristic timescale. After three rotations of Vela, $\sim 1\%$ of the initial elastic energy is in the magnetosphere, and $\sim 95\%$ of the initial energy has been transmitted into the liquid core. The luminosity $L_{\rm A}$ has decreased by a factor of ~ 20. The evolution of $L_{\rm A}$ and the wave energy in all four models is summarized in Figures 3.8 and 3.9.

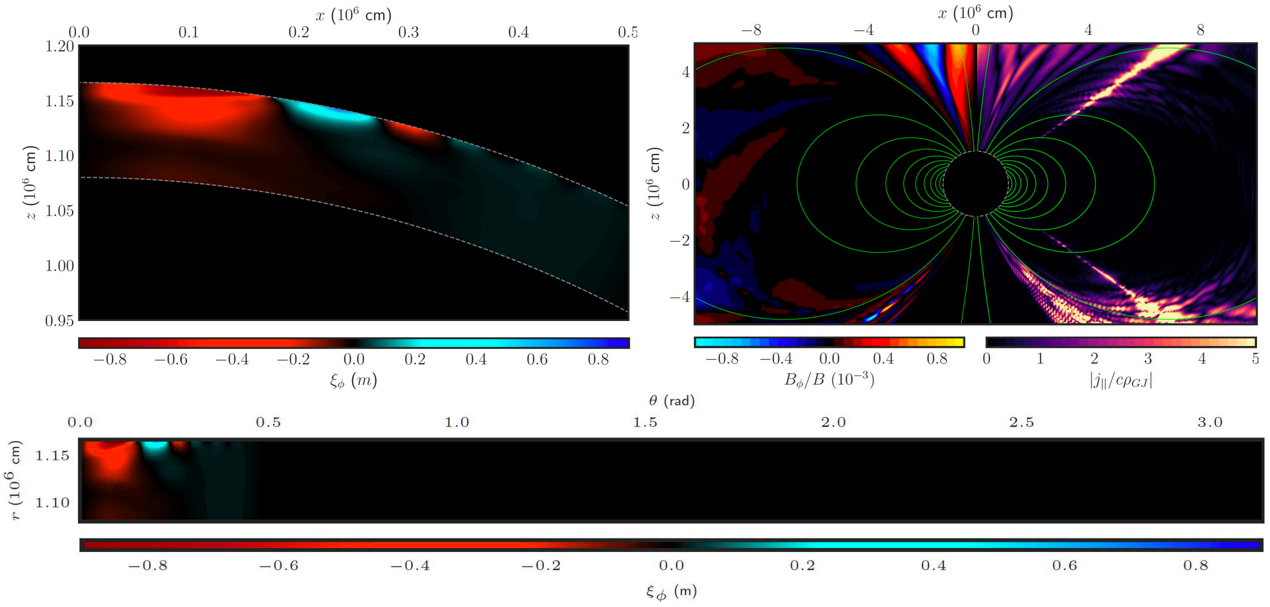

Figure 3.4: Model A1 at $t = 2$ ms. Top left: displacement ξ_ϕ of the crust near the epicenter of the quake. The dashed lines show the boundaries of the crust. Top right: toroidal perturbation of the magnetic field B_ϕ/B (left), and the ratio $|j_\parallel/c\rho_{GJ}|$ (right). The green curves show the poloidal magnetic field. The two field lines closest to the axis of symmetry are the boundary of the open field-line bundle. The gray dashed circle is the surface of the neutron star. Bottom: displacement $\xi_\phi(r,\theta)$ in the entire crust, plotted on the r-θ plane.

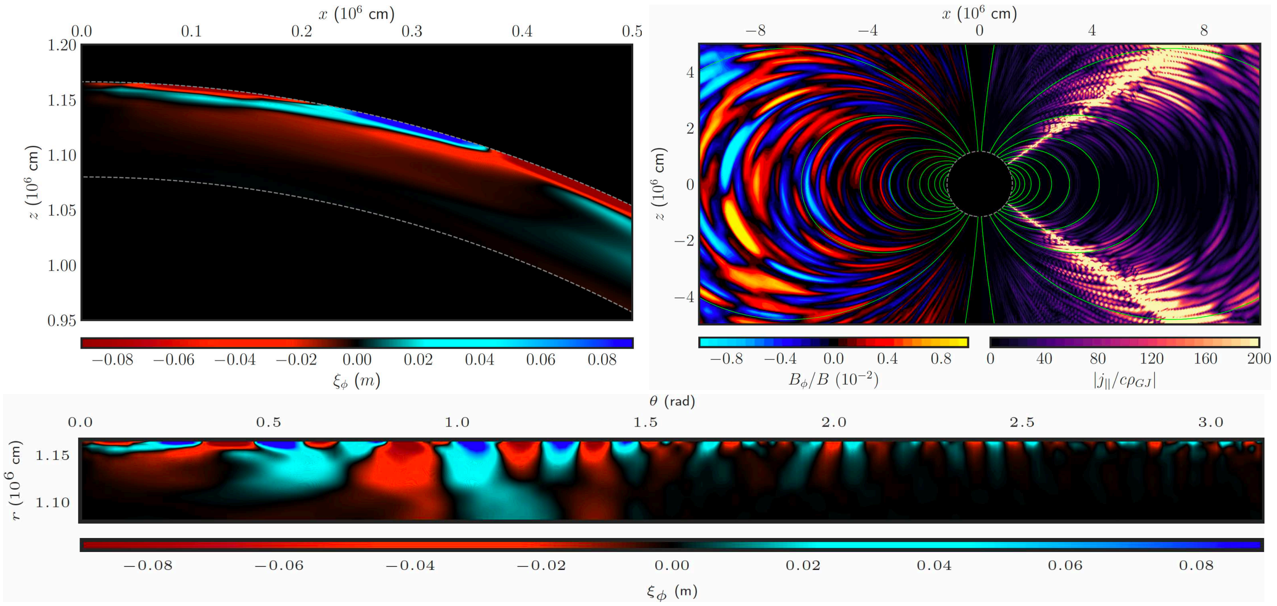

Figure 3.5: Same as Figure 3.4 but at time $t = 50$ ms.

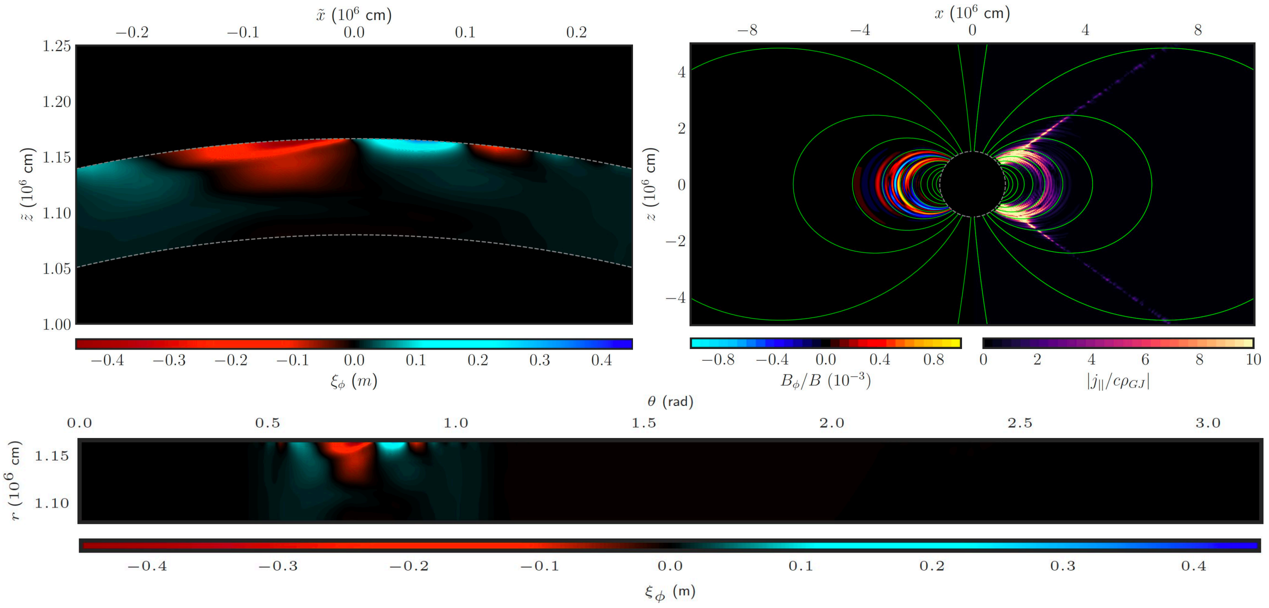

Figure 3.6: Model B1 at $t = 2$ ms. Top left: displacement ξ_ϕ of the crust near the epicenter of the quake. The epicenter is at $\theta = 45$ °, and we have rotated the figure by -45 ° ($\tilde{x} = x - z$ and $\tilde{z} = x + z$). The dashed lines show the boundaries of the crust. Top right: toroidal perturbation of the magnetic field B_ϕ/B (left), and the ratio $|j_\parallel/c\rho_{GJ}|$ (right). The green curves show the poloidal magnetic field. The two field lines closest to the axis of symmetry are the boundary of the open field-line bundle. The gray dashed circle is the surface of the neutron star. Bottom: displacement $\xi_\phi(r, \theta)$ in the entire crust, plotted on the r-θ plane.

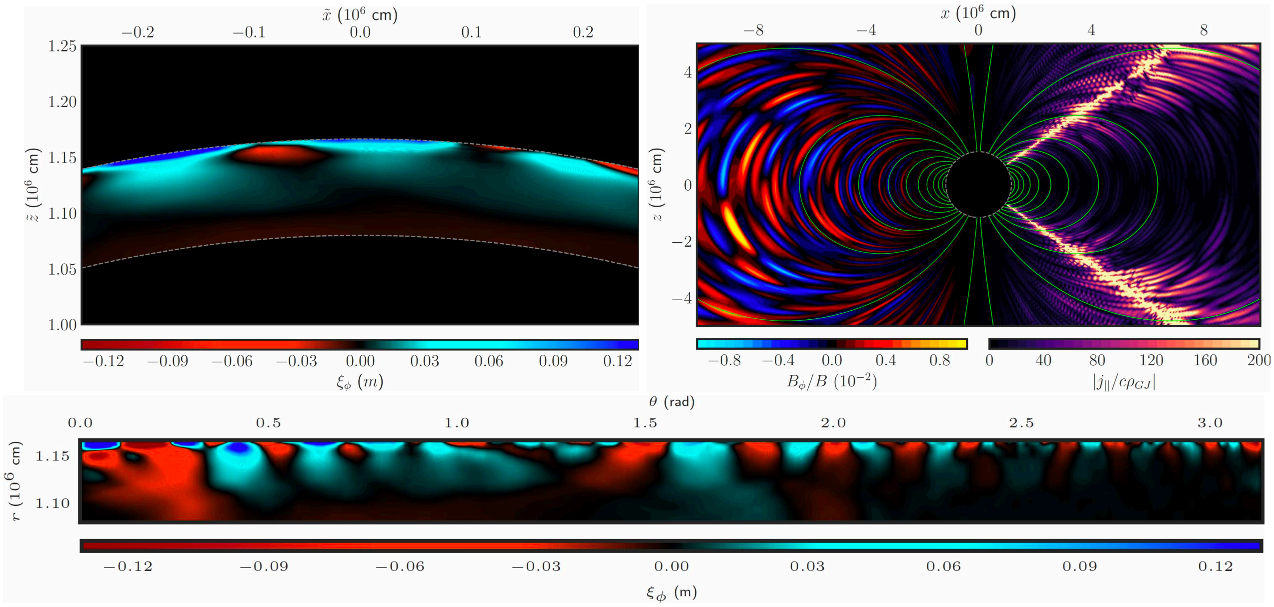

Figure 3.7: Same as Figure 3.6 but at time $t = 50$ ms.

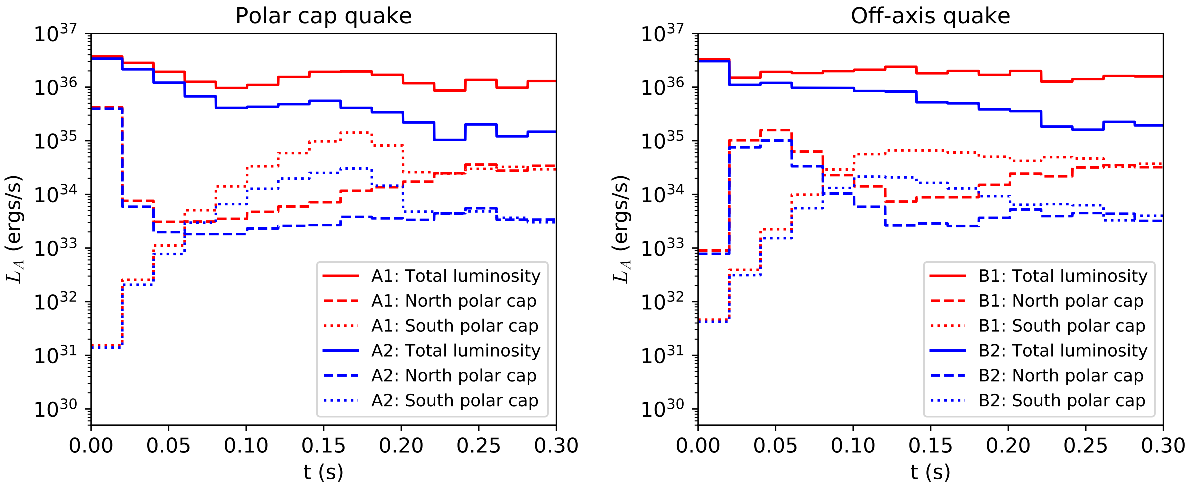

Figure 3.8: Luminosity of Alfvén waves emitted into the magnetosphere, L_A. The luminosity has been averaged into 20 ms bins to remove the noise from fast oscillations. Left: models A1 and A2 (initial quake under the polar cap). Right: models B1 and B2 (initial quake at $\theta \sim \pi/4$). Red is used for models with no crust-core coupling (A1 and B1), and blue for models with strong crust-core coupling (A2 and B2). For each model, we show L_A from the entire stellar surface (solid curve), and the contributions from the north (dashed) and south (dotted) polar caps.

3.7 Discussion

Glitches give deep insight into the exotic dynamics of quantum fluids that likely exist in pulsar interiors. One of the unsolved theoretical issues is the cause of the nearly simultaneous unpinning of billions of superfluid vortices over a macroscopic $10 - 10^3$ m length that must take place during a glitch. The catastrophic unpinning is required to explain the glitches' magnitudes, especially the giant glitches with the relative spin-up of $\sim 10^{-5}$ observed in Vela. Crustal quakes have been suggested as one of the candidates for the glitch trigger, but not considered promising for Vela. Indeed, what could deform the crust so dramatically that it would have a mechanical failure? Vela's external magnetic field is two orders of magnitude smaller than that of magnetars, and thus the magnetic stresses are not obviously sufficient to break the crust. Furthermore, Vela is spinning at 1% of the break-up angular velocity, and thus its relative rotational deformation is $\sim 10^{-4}$, which is smaller than the critical strain of the crust. Therefore, rotational deformation is also unlikely to lead to a quake.

Nonetheless, the remarkable observations of the 2016 glitch by [40] force one to seriously

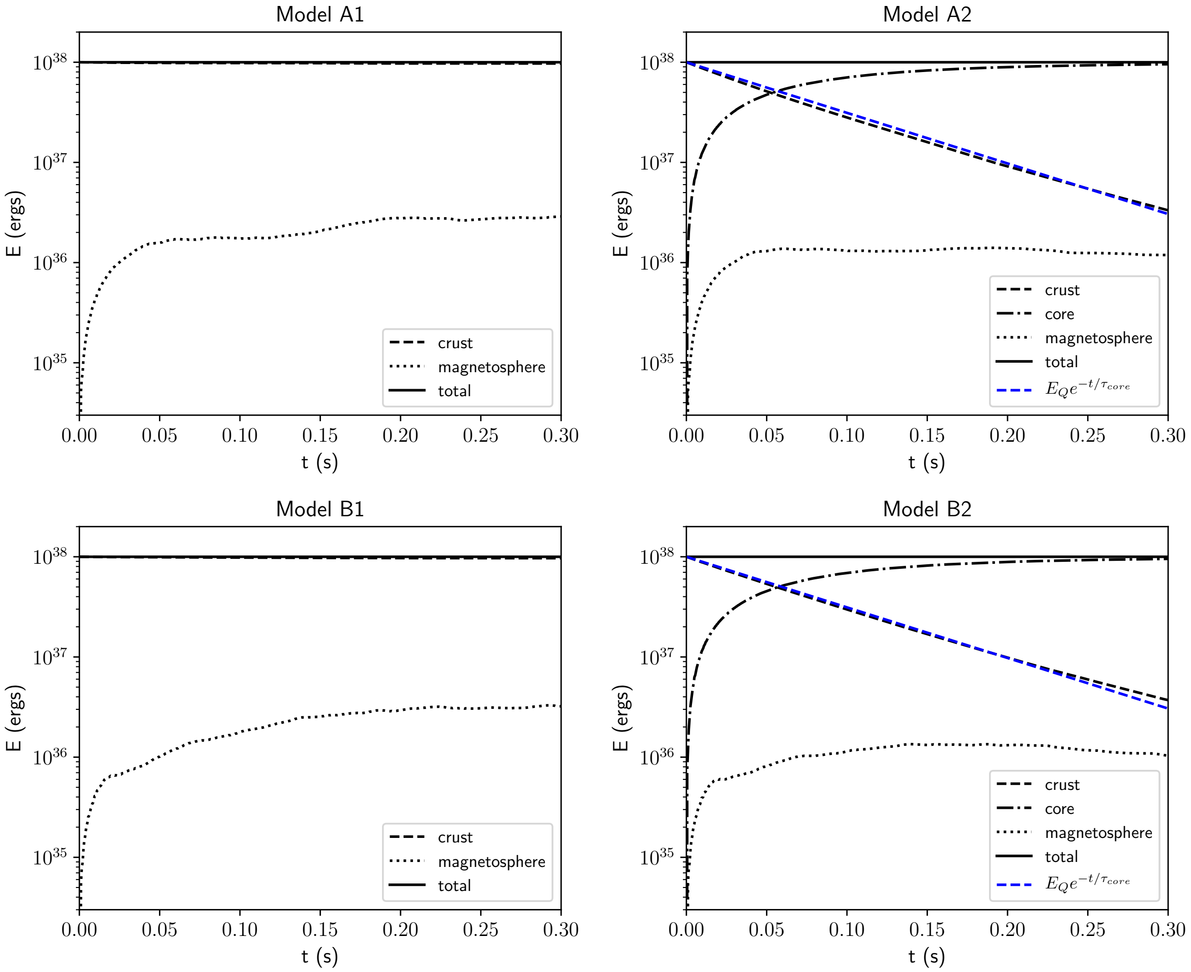

Figure 3.9: Evolution of the quake energy. The four panels show the results for models A1, A2, B1 and B2. The energy retained by the crustal oscillations E_{crust} (dashed curve) is reduced by the transmission into the magnetosphere (dotted) and (in models A2, B2) transmission into the core (dotted-dashed). As required by energy conservation, the sum of the retained and transmitted energies remains equal to $E_Q = 10^{38}$ erg (horizontal solid line). The blue dashed line shows the analytical approximation to $E_{\mathrm{crust}}(t)$ (Equation 3.77) with $\tau_{\mathrm{core}} = 86\,\mathrm{ms}$.

consider a quake as a trigger. The change in the magnetospheric activity indicates its strong disturbance by the glitch on a timescale shorter than 0.1 s. The only plausible way for such a disturbance to be delivered from the star's interior is through a shear wave that reaches the interface between the crust and the magnetosphere. The high-frequency elastic wave can shake vortex pinning sites in the crust. The resulting magnus force can unpin vortices in a macroscopic region causing a glitch [132]. Alternatively, plastic failure of the crust could generate sufficient heat to thermally unpin many vortices [133].

In this paper, we studied an important ingredient of such a scenario — the seismic motion in the crust and its coupling to the magnetosphere and the core. We have shown that the seismic activity, once created, spreads through the crust and engages the whole magnetosphere in Alfvén-type oscillations. Even for a modest-amplitude quake, we find that the magnetospheric disturbance can cause an electric discharge that produces gamma-rays and $e^{\pm}$ pairs. We are unable to make specific predictions for the quake effect on the radio luminosity $L_{\rm GHz}$, because the mechanism of pulsar emission is poorly understood. However, it is reasonable to expect that the appearance of a new powerful $e^{\pm}$ source changes $L_{\rm GHz}$ for the duration of the quake, and could shut down the radio pulsations as observed in the Vela glitch in 2016 December. The seismic motion in the crust is damped on a short timescale through emission of Alfvén waves into the liquid core. This process is sped up by the enhanced magnetic tension due to the bunching of the magnetic field into flux tubes in the superconducting core of Vela. As a result, the damping timescale for the crustal oscillations is as short as ~ 0.2 s, comparable to the duration of the observed pulse disturbance.

New detailed observations would help confirm the presence of magnetospheric disturbances during glitches. If such disturbances turn out to be common, they will require a paradigm shift that should include crustal quakes as a common phenomenon in young pulsars. This could indicate internal magnetic fields that are orders of magnitude greater than the external dipole component responsible for the pulsar spin-down. The existence of ultra-strong internal fields would not require the assumption of superconductivity to explain the short lifetime of the quake. In addition, it would indicate that the Vela glitches are due to the crustal superfluid, contrary to models that invoke the core superfluid (e.g. [7], [134]). The theoretical challenges pertaining to pulsar exteriors would also be considerable: the damping of the strong magnetospheric waves and their impact on pair production and pulsar radio emission will need to be understood.

The methodology developed in this paper is not limited to studies of quakes in pulsars, but can also be used for studies of magnetars, where superstrong crustal quakes were proposed as triggers of giant X-ray flares [9].

Finally, we note that the quake we invoked for the Vela glitch is capable of producing a weak X-ray burst. We found the Alfvén wave energy deposited in the magnetosphere $E_{\rm A} \sim 10^{-2} E_Q \sim 10^{36}$ erg. This energy is dissipated through the discharge, and a large fraction of $E_{\rm A}$ should be emitted in the X-ray band. In particular, X-rays are emitted by $e^{\pm}$ created near the star in excited Landau states, and cascading down to the ground state. The duration of the X-ray burst is comparable to the dissipation timescale for the magnetospheric Alfvén waves. The burst is much brighter than than the normal pulsating X-ray luminosity of Vela; however, its detection is challenging because of the short duration and the modest fluence.

Chapter 4: Pulsar Magnetospheres and Radio Emission

4.1 Introduction

Pulsars are rotating magnetized neutron stars which produce powerful beams of coherent radio emission. Despite an abundance of observational data, the mechanism generating radio waves in pulsar magnetospheres has remained elusive for more than fifty years. Pulsar magnetospheres are filled with highly magnetized collisionless electron-positron ($e^{\pm}$) plasma which is produced in electric gaps — regions with voltage along magnetic field lines. Electric discharge in the gaps may be responsible for pulsar radio emission, and the only reliable way to solve this nonlinear problem is with a self-consistent numerical simulation.

In the last decade there has been a significant computational effort to model the magnetosphere structure and multi-wavelength emission from first-principles using the particle-in-cell (PIC) technique [52–54]. Global simulations unanimously display powerful gamma-ray emission from the outer magnetosphere [54, 135], but radio waves were not observed. Recently [50] showed that radio waves can be generated directly by the time-dependent $e^{\pm}$ discharge above the polar-cap. The authors used local PIC simulations of the gap in cartesian geometry — it required high voltage and resolution which were not achieved in global simulations.

In this Letter we present a global kinetic plasma simulation of an axisymmetric magnetosphere. Our numerical experiment achieves voltage and spatial resolution sufficient to reveal new features, including locations of electric gaps where $e^{\pm}$ lightning ignites and produces coherent radio waves. We observe streaming instabilities in the magnetosphere for the first time.

4.2 Numerical Method

The kinetic plasma simulation is performed with the relativistic PIC code `Pigeon` [55, 56], which solves Maxwell's equations with the equations of motion for charged particles and $e^{\pm}$ creation. We include a general-relativistic correction to Faraday's law which describes the rotational frame-dragging effect near the star [54]. We set the compactness of the star $r_s/r_\star = 0.5$, where $r_s = 2GM/c^2$ is the Schwarzschild radius and $r_\star$ is the radius of the star. Hereafter lengths are given in units of $r_\star$, and times in units of $r_\star/c$. The $e^{\pm}$ have mass m and charge $\pm e$, while ions (protons) have charge e and mass $m_i = 10m$. Electromagnetic fields are given in units of $mc^2e^{-1}r_\star^{-1}$, number density in units of $r_\star^{-3}$, and charge density in units of $er_\star^{-3}$.

The scales of the problem are set by the angular velocity Ω and the magnetic dipole moment μ of the pulsar. Rotation of the magnetized star induces a voltage $\Phi_0 \approx \mu\Omega^2/c^2$ capable of accelerating $e^{\pm}$ to Lorentz factor $\gamma_0 = e\Phi_0/mc^2$. For real pulsars $\gamma_0 \sim 10^{11}$. We scale it down to $\gamma_0 = 2 \times 10^4$, which allows us to resolve the plasma skin depth. Our value of γ_0 is twice as large as in previous work [56], and our resolution is twice as high. We set $\Omega = 1/6$, which implies the light-cylinder radius $R_{\mathrm{LC}} = c/\Omega = 6$. The minimum charge density required to support the co-rotating magnetosphere $\rho_{\mathrm{GJ}} = -\boldsymbol{\Omega} \cdot \boldsymbol{B}/(2\pi c)$ [43] defines the characteristic number density $n_{\mathrm{GJ}} = |\rho_{\mathrm{GJ}}|/e$ and plasma frequency $\omega_p = (4\pi n_{\mathrm{GJ}} e^2/m)^{1/2}$. Similar to real pulsars, the simulation preserves the hierarchy of scales $\Omega \ll \omega_p \ll \omega_B$, where $\omega_B = eB/mc$ is the cyclotron frequency.

The gamma-ray emission, propagation, and $e^{\pm}$ production is modelled using the Monte-Carlo method [52]. The $e^{\pm}$ emit gamma-rays of energy $\epsilon_\gamma = 10mc^2$ when they reach the threshold energy $\gamma_{\mathrm{thr}}mc^2$. The threshold depends on the curvature of the field lines [52], and has typical value $\gamma_{\mathrm{thr}} \sim 100$. The gamma-rays propagate with mean free path ℓ before converting to secondary $e^{\pm}$ with $\gamma_s mc^2 = \epsilon_\gamma/2$. For $r < 2$, we set $\ell = 0.2$ to simulate conversion off the strong magnetic field near the stellar surface ($\gamma - B$ channel). For $r > 2$, we set $\ell = 5$ to simulate collisions with soft target photons in the outer magnetosphere ($\gamma - \gamma$ channel). The energy scales in our numerical experiment satisfy the correct hierarchy $1 \ll \gamma_s \ll \gamma_{\mathrm{thr}} \ll \gamma_0$.

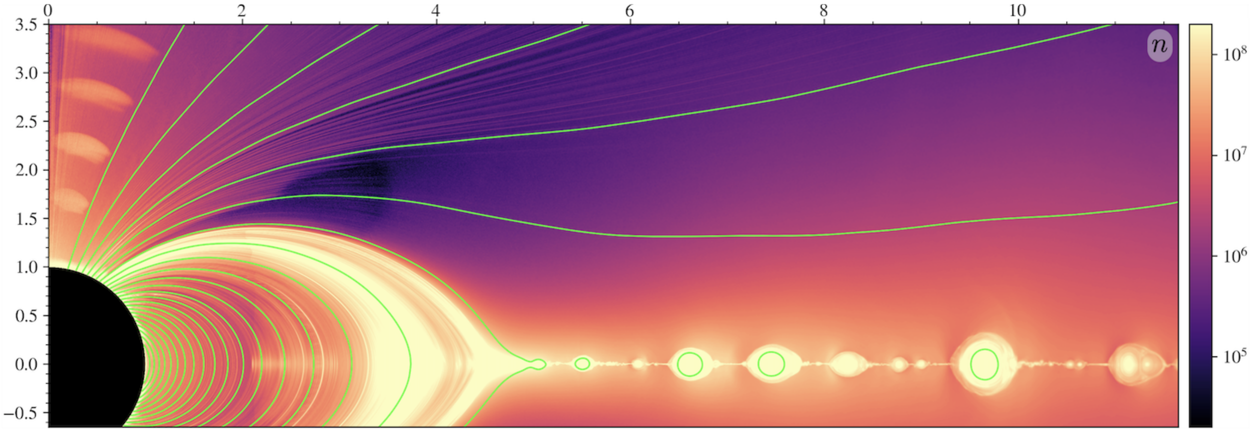

Figure 4.1: Plasma density n (color bar) in the quasi-steady state. The vertical axis shows distance along the spin axis. Green curves show poloidal magnetic field lines. The dense clouds of plasma above the polar cap form in $e^{\pm}$ discharge episodes. The absence of plasma (dark zone) above the separatrix shows the return-current gaps in the unscreened state; it fills with plasma every $\sim 2R_{\rm LC}/c$ when the return-current discharges ignite.

The computational domain covers $1 \leq r \leq 30$ and $0 \leq \theta \leq \pi$. The grid is uniform in $\log r$ and θ, and has resolution $N_r \times N_\theta = 8192 \times 8192$ cells. The plasma scale $2\pi c/\omega_p$ near the stellar surface is resolved by 25 grid cells. At the surface, the electromagnetic fields satisfy a rotating conductor boundary condition, and we maintain a gravitationally bound electron-ion atmosphere with multiplicity $\mathcal{M}_{atm} = n_{atm}/n_{\rm GJ} = 10$. At the outer boundary fields are damped, and particles are absorbed.

4.3 Magnetosphere Structure

The simulation begins with a non-rotating star with a vacuum dipole magnetosphere. As we smoothly increase the angular velocity to Ω, charges are lifted from the atmosphere and accelerated, triggering gamma-ray emission and $e^{\pm}$ production which fills the magnetosphere with plasma. The magnetosphere reaches a quasi-steady state after the first rotation of the star (Fig. 4.1). Its global structure is similar to previous axisymmetric force-free and PIC models [52, 136–138]. The higher voltage in our simulation leads to more efficient filling of the open field lines with plasma. A new feature is the $e^{\pm}$ discharge in the outer magnetosphere outside the Y-shaped current sheet.

This feature was not present in previous PIC simulations with smaller voltages. We also observe $e^{\pm}$ discharge near the polar caps, an expected result of the relativistic frame-dragging effect [139]. The strongest dissipation and gamma-ray emission occurs in the equatorial current-sheet [135]. Here, magnetic reconnection forms a dynamic plasmoid chain.

4.4 Gaps and Electric Discharge

The gaps (regions with non-zero $E_{||} = \boldsymbol{E} \cdot \boldsymbol{B}/|\boldsymbol{B}|$) form because of a mismatch between the required parallel current $j_B = (c/4\pi)(\nabla \times \boldsymbol{B}) \cdot \boldsymbol{B}/|\boldsymbol{B}|$ and the maximum possible current $j_{\max} = c\rho_{\rm GJ}$ that could be supplied by the outward flow of a charge-separated plasma with the local charge density $\rho = \nabla \cdot \boldsymbol{E}/4\pi$. If the charged plasma under-supplies the required current ($\alpha \equiv j_B/j_{\max} > 1$), or supplies it with the wrong sign of charge ($\alpha < 0$), Ampere's law guarantees the inductive growth of $E_{||}$ which can trigger the runaway production of $e^{\pm}$ [140]. The time-dependent gaps observed in the simulation differ from the gap models based on electrostatic considerations (Gauss' law), including the classical polar-gap [44], slot-gap [141], and outer-gap [142, 143].

A time-dependent gap with $\alpha > 1$ forms near the magnetic axis above the pulsar polar cap. This gap occurs because the general-relativistic frame-dragging effect reduces the apparent rotation of the star, and thus reduces $\rho_{\rm GJ}$ near the surface, while leaving the required current j_B [53, 139, 144, 145]. The resulting $\alpha > 1$ renders the electron flow extracted from the star unable to supply j_B, even if it moves at the speed of light. Thus, $E_{||}$ is induced, igniting $e^{\pm}$ discharge. The discharge begins when electrons are lifted from the atmosphere by $E_{||}$ and accelerated to energies $\sim \gamma_{\rm thr} mc^2$. The electrons emit gamma-rays, which convert to $e^{\pm}$ through the $\gamma - B$ channel. The increasing density of pairs quickly screens $E_{||}$, and the $e^{\pm}$ shower proceeds outward. As the cloud of $e^{\pm}$ leaves, $E_{||}$ grows again and the discharge cycle repeats. The discharge reaches maximum multiplicity $\mathcal{M} \equiv n/n_{\rm GJ} \sim 10$. The gap height is $h \sim 0.4$, and the cycle time is $\sim h/c$.

The magnetosphere prevents the accumulation of net electric charge on the neutron star by arranging positive return-currents, which compensate the negative charge flowing out of the polar-cap. Most of the return-current flows along the thin separatrix layer and is sustained by pair creation

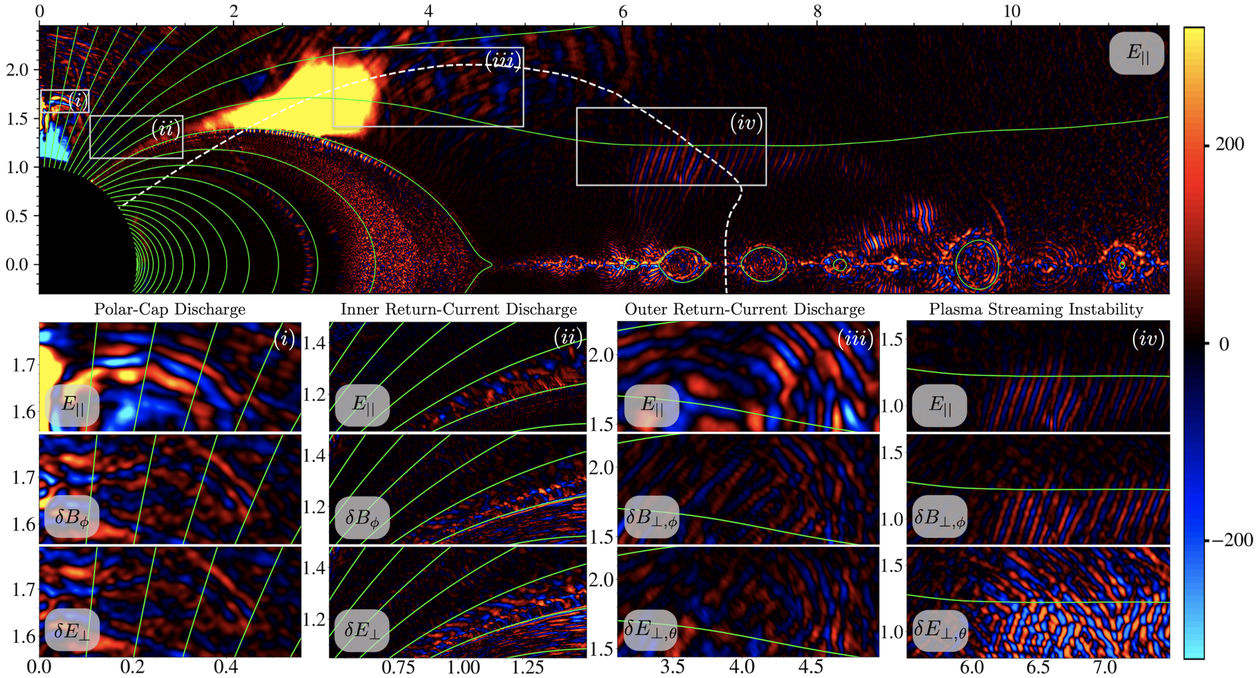

Figure 4.2: Excitation of plasma waves in the pulsar magnetosphere. The vertical axis shows distance along the spin axis, and the color bar shows components of the electromagnetic field multiplied by $(r/r_\star)^2$. Top : $E_{||}$ in the quasi-steady state. The dashed white curve shows the null-surface $\rho_{\rm GJ} = 0$ (the null-surface breathes outside $r_{\rm LC}$ due to plasmoid motion). Insets (i)-(iii): Electromagnetic modes excited during $e^\pm$ discharges at the polar-cap, inner return-current, and outer return-current gaps. Inset (iv): Waves excited by a streaming instability. For insets (i) and (ii), $\delta E_\perp$ lies in the poloidal plane.

at the Y-point [56]. We also observe a bulk return-current of macroscopic thickness on open field lines outside the separatrix layer which pass through the null-surface defined by $\rho_{\rm GJ} = 0$ [Fig. 4.2, top, dashed line]. The bulk return-current draws electrons from the pair plasma created around the light-cylinder.

The simulation reveals two time-dependent gaps on the field lines that conduct the bulk return-current: (i) an inner return-current gap of type $\alpha < 0$ forms between the polar-cap and the null-surface where $\rho_{\rm GJ} < 0$ and $j_B > 0$, and (ii) an outer return-current gap of type $\alpha > 1$ forms outside the null-surface where $\rho_{\rm GJ} > 0$ and $j_B > 0$. The presence of two gaps on the same field lines results in coupled discharge dynamics. The two interacting discharges reach $e^\pm$ multiplicities $\mathcal{M} \sim 5$ and repeat on the timescale $\sim 2R_{\rm LC}/c$.

The inner return-current gap has $\rho_{\rm GJ} < 0$, so here the charge density can only be supplied by electrons. Electrons flow toward the star in order to conduct $j_\mathrm{B} > 0$. When this flow dwindles, a gap opens near the null-surface (with $E_{||}$ directed away from the star) and expands inward until it reaches altitude $r \sim 2r_\star$ where pair production through the $\gamma - B$ channel becomes possible. Then discharge develops, seeded by the inward electron flow accelerated in the gap. Pair creation quickly screens $E_{||}$, and the shower proceeds toward the star, spreading laterally due to the curvature of the magnetic field lines and the finite free paths of tangentially emitted gamma-rays. Some of the secondary positrons are reversed by $E_{||}$ at the discharge onset; they escape outward and serve as seeds for the discharge in the outer return-current gap.

The outer return-current gap extends from the null-surface toward R_LC (Fig. 4.2, top). The gap occurs because the required current is positive, $j_B > 0$, but positrons are not readily available from inside the null-surface where $\rho_\mathrm{GJ} < 0$. This generates $E_{||}$ directed away from the star. It pulls electrons into the gap from larger radii. The inward flowing electrons supply the correct sign of the current, but the wrong sign of charge ($\rho_\mathrm{GJ} > 0$), so they cannot screen the gap. Instead, they get accelerated by $E_{||}$, cross the null-surface and trigger the inner return-current discharge, which provides a source of positrons from inside the null-surface. These seed positrons get accelerated and trigger pair production in the outer return-current gap through the $\gamma - \gamma$ channel. Thus, the two gaps (inner and outer) assist each other in repeating pair discharge.

4.5 Discharge Waves

Fig. 4.2 shows the plasma waves excited during the polar-cap discharge [inset (i)], the inner return-current discharge [inset (ii)], and the outer return-current discharge [inset (iii)]. The electromagnetic fields of the waves $\delta\boldsymbol{B}$ and $\delta\boldsymbol{E}$ are isolated by first subtracting the time average to remove the zero frequency (background) component. Then we subtract a local spatial average calculated along the magnetic field line, which removes large amplitude low frequency oscillations caused by breathing of the global magnetosphere. The perpendicular part of the waves are calculated as $\delta\boldsymbol{B}_\perp = \boldsymbol{B} - \delta\boldsymbol{B}_{||}$, where $\delta\boldsymbol{B}_{||} = \delta\boldsymbol{B} \cdot \boldsymbol{B}/|\boldsymbol{B}|$.

The observed discharge waves are consistent with the mechanism seen in previous local simulations: pair production in the gap electric field drives a current which directly couples to oscillations in $E_{||}$, $\delta \boldsymbol{B}_{\perp}$, and $\delta \boldsymbol{E}_{\perp}$ [50, 146]. The wavelength of the modes is consistent with $\lambda \sim 2\pi c/\omega$ [Fig. 4.2, insets (i)-(iii)], where $\omega = (4\pi n e^2/\langle\gamma^3\rangle m)^{1/2}$ is the local plasma frequency. The wave electric field is polarized in the $\boldsymbol{k}-\boldsymbol{B}$ plane, which suggests that an ordinary (O) mode is excited ($\boldsymbol{k}$ is the wave vector). In particular, $\delta E_{\perp}/E_{||}$ is consistent with the superluminal O-mode polarization [147], in agreement with local simulations [50, 146]. As the discharge develops and plasma density increases, a spectrum of higher frequency modes is excited [50], although we only resolve low frequencies in the global simulation. The wave amplitude is consistent with $E_{||}^{\star} \sim \gamma_s m c \omega_{\star}/e$, where $\omega_{\star} = 2\pi\nu_{\star}$ is the plasma frequency later in the discharge when $E_{||}$ can barely reverse $e^{\pm}$ [148]. At each gap the emission of waves is strongly modulated on the gap light-crossing timescale.

Our simulation also demonstrates the extraordinary (X) modes emitted from the equatorial plasmoid chain [Fig. 4.2, $\delta B_{\perp}$, $\delta E_{\perp}$, insets (iii), (iv)] [149, 150]. These waves are easy to identify, because their electric field is polarized in the $\boldsymbol{k}\times\boldsymbol{B}$ direction, and is absent in $E_{||}$. Note, in axisymmetry $\boldsymbol{k}$ lies in the poloidal plane. Near the star $\boldsymbol{B}$ is approximately poloidal, and insets (i) and (ii) display the O-mode polarization. At large radii $\boldsymbol{B}$ is twisted, and insets (iii) and (iv) contain contributions from the O-mode and X-mode.

4.6 Instabilities

The simulation also reveals plasma streaming instabilities, triggered at several sites in the outer magnetosphere. The triggering mechanism is non-local: the $e^{\pm}$ wind becomes exposed to a gamma-ray beam emitted elsewhere in the magnetosphere, which injects an $e^{\pm}$ beam with a different momentum (Fig. 4.3). Both streams are made of secondary $e^{\pm}$, and thus the instability growth rate is not strongly suppressed by ultra-high Lorentz factors typical for primary accelerated particles. The instability is electrostatic in nature, and controlled by plasma oscillations along the magnetic field lines (rapid gyration of the particles increases their effective parallel inertia, but

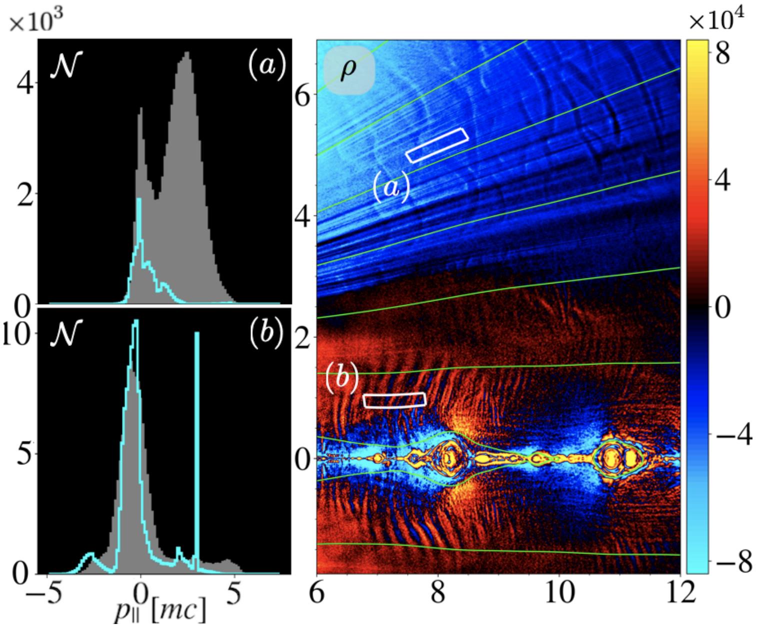

Figure 4.3: Streaming instabilities in the outer magnetosphere. Left: Parallel momentum ($p_{||}$) distributions of $e^{\pm}$ (grey) and gamma-rays (cyan) in regions (a) and (b) in the right panel. For gamma-rays we show distributions of $p_{||}/2$ (their momentum is split between the created e^+ and e^-). (a): Gamma-rays from the current-sheet (cyan peak) inject $e^{\pm}$ (grey peak). (b): Gamma-rays from the separatrix (thin cyan peak) and the current-sheet (wider cyan peak) inject different $e^{\pm}$ beams. Right: Charge density ρ and charge bunch formation.

does not change the qualitative behaviour of the instability). Charge bunches form at each site where the instability occurs (Fig. 4.3).

The beam energy is deposited into growing plasma modes [Fig. 4.2, inset (iv)]. The observed wavelength of the modes is consistent with $\lambda_0 \sim 2\pi c/(\omega_p \gamma^{1/2})$, indicating that the instability is first triggered on Cherenkov resonance [151]. The modes are inclined to the local magnetic field, and have transverse and longitudinal components [Fig. 4.2, inset (iv)]. The phase speed is necessarily subluminal. Therefore, we identify the excited waves as hybrid electrostatic-Alfvén modes [147, 152]. The waves have amplitude $E_{||} \sim 4\pi \Delta\rho \lambda_0$, where $\Delta\rho \sim \rho_{\rm GJ}$ is the charge density of the observed bunches (Fig. 4.3). The fate of the waves and radiation from the charge bunches should be investigated with detailed local simulations.

4.7 Discussion

Our numerical experiment has achieved a voltage large enough to reveal the locations where the $e^{\pm}$ lightning ignites and produces coherent radio waves. In addition to the well known polar-cap gap, the simulation has uncovered a pair of interacting gaps in the outer magnetosphere, which form around the null-surface in the bulk return-current. Furthermore, we observed waves and charge bunches excited by streaming instabilities in the secondary $e^{\pm}$ plasma — a result of multiple gamma-ray streams revealed by the global simulation. The high resolution is key to these findings, providing a glimpse of the origin of pulsar radio waves, a subtle phenomenon compared to pulsar gamma-ray emission. The simulation also confirms the powerful narrow fan of the equatorial gamma-rays reported in [56].

The electric discharge in our simulation reaches pair multiplicity $\mathcal{M} \sim 5 - 10$, much smaller than in real pulsars. However, it is large enough to demonstrate the limit-cycle behaviour of the gaps and the excitation of electromagnetic modes in the global magnetosphere. Realistic multiplicities up to $\mathcal{M} \sim 10^4$ are so far achieved only in local 1D discharge simulations [49, 57], and excitation of waves in a polar-cap discharge was previously demonstrated in local 2D simulations with $\mathcal{M} \sim 10$ [50, 146]. Simple estimates suggest that the discharge waves offer a promising mechanism for pulsar radio emission. The waves are excited near the local plasma frequency $\nu \sim \nu_p$ which scales as $\mathcal{M}^{1/2}$. For a realistic $\mathcal{M}$, one can estimate $\nu \sim (2\pi)^{-1}(4\pi\mathcal{M}n_{\rm GJ}e^2/\langle\gamma^3\rangle m)^{1/2} \sim$ MHz-GHz [50, 153]. The expected wave amplitude at the polar-cap $E_{||}^{\star} \sim 10^5\ (\gamma_s/10^3)(\nu_{\star}/\mathrm{GHz})$ G implies $L_{\rm radio} \sim cE_{||}^{\star 2}A_{\rm pc}/(4\pi) \sim 10^{29}\ (A_{\rm pc}/10^9\mathrm{cm}^2)$ erg s^{-1} [148], similar to observed pulsars ($A_{\rm pc}$ is the polar-cap area).

The global kinetic simulation offers a physical framework to start interpreting the rich pulsar observations. In particular, the polar-cap discharge may be responsible for the so-called “core” radio emission, and the inner return-current discharge may produce “conal" radio emission. The wave power is strongly modulated by the electric discharge of the gaps, which may produce microstructure in the pulse profiles. The plasma instabilities could produce outer magnetospheric radio emission in energetic pulsars which is different to the traditional emission. However, significant work is needed to improve the simulations before they can be directly compared to individual pulsars. It should be understood how the down-scaled voltage (and $\mathcal{M}$) may affect the non-linear interaction of the return-current gaps. A more detailed implementation of gamma-ray emission and $e^{\pm}$ production may change the streaming instabilities and charge bunching. It has been suggested that charge bunches could produce coherent curvature emission in the radio band [44, 154] and the waves experience propagation effects [45–48], which needs further investigation. Finally, our simulation was limited to aligned rotators $\boldsymbol{\mu} \parallel \boldsymbol{\Omega}$. It will be essential to investigate radio emission in inclined rotators.

Chapter 5: Black Hole Magnetospheres and No-Hair Theorem

5.1 Introduction

Black holes (BHs) formed by the collapse of a magnetized progenitor are born with magnetic fields penetrating the event horizon. There are several possible scenarios, such as the spin-down of a rotationally supported hyper-massive neutron star (NS) [155], or gravitational collapse induced by the accretion of dark matter onto the NS core [156]. BHs can also acquire magnetic flux later in life by merging with a magnetized NS [157], or in accretion flows. The fate of the magnetic flux (hair) on the event horizon should be in accordance with the no-hair theorem of general relativity.

The original no-hair conjecture [59] states that all stationary, asymptotically flat BH spacetimes should be completely described by the mass, angular momentum, and electric charge. It was later proved formally that any field with zero rest mass and arbitrary integer spin is radiated away on a light crossing timescale [158]. In particular, the multipole component l of a magnetic field in vacuum decays as $t^{-(2l+2)}$. However, magnetized BHs are unlikely to exist in vacuum. If a BH is formed by the collapse of a magnetized star, plasma will inevitably exist in the magnetosphere around the newly formed event horizon. Furthermore, BHs can generate a self-regulated plasma supply through electron-positron discharges near the event horizon [60–62]. The discharges can fill the magnetosphere with plasma in a light crossing time.

The presence of highly conducting plasma, and thus non-zero stress-energy tensor of matter, dramatically changes the vacuum dynamics assumed in the classical no-hair theorem. Essentially, in the limit of vanishing resistivity a topological constraint is imposed which prevents the magnetic field from sliding off the event horizon [63]. The only way for the BH to lose its magnetic field is for the field to change its topology (reconnect). Fast magnetic reconnection occurs through the tearing instability [64]. A chain of plasmoids (magnetic loops containing plasma) forms along the reconnection layer which are ejected at relativistic velocities. For highly magnetized collisionless plasma (as expected in a BH magnetosphere), the reconnection rate $v_{\rm rec} \sim 0.1c$ is independent of the magnetization [65–67]. The lifetime of the magnetic flux on the event horizon should be determined in part by this universal reconnection rate.

Previous work in an ideal fluid approximation correctly established the qualitative evolution of a dipole magnetic field on the event horizon opening into a split-monopole [63]. However, it neglected collisionless physics, and was performed at low numerical resolution such that the reconnection was not in the high Lundquist number regime [63, 68]. This lead to the conclusion of an extremely long lifetime of the magnetic flux on the event horizon, dictated by the resistive timescale of the plasma [63]. In this Letter we describe for the first time GRPIC (general-relativistic particle-in-cell) and GRRMHD (general-relativistic resistive magnetohydrodynamics) simulations which are converged and produce the correct reconnection physics.

5.2 Numerical Method

The system is solved numerically in Kerr spacetime. Kerr-schild coordinates (t, r, θ, ϕ) are used so that all quantities are regular at the event horizon. The dimensionless BH spin is set to $a = 0.99$ to maximize the ergosphere volume. We define “fiducial observers" (FIDOs), whose worldlines are normal to spatial hypersurfaces. We assume that the NS was already surrounded by plasma, and that it collapsed into a BH before the simulation begins. This setup is sufficient to test the no-hair theorem because when plasma is present, the magnetic field cannot escape before the event horizon has formed [63]. The initial condition for all simulations is a magnetic dipole described by the vector potential $A_\phi = B_0 \sin^2\theta / r$, where B_0 is the dimensionless magnetic field strength at the horizon as measured by the FIDO. The magnetic field components are obtained from $B^i = \epsilon^{ijk}\partial_j A_k/\sqrt{\gamma}$, where $\sqrt{\gamma}$ is the spatial metric determinant. In vacuum non-zero $\nabla \times (\alpha \boldsymbol{B})$ is quickly radiated away or swallowed by the BH (α is the lapse). However, when plasma is present non-zero $\nabla \times (\alpha \boldsymbol{B})$ drives currents which slow down the balding process.

The kinetic plasma simulations are performed using the general-relativistic particle-in-cell

(PIC) code `Zeltron` [61]. We solve the equations of motion for pair plasma particles, together with Maxwell's equations for electromagnetic fields. All lengths are given in units of $r_g = GM/c^2$ with M the BH mass, and times in units of r_g/c. The particles have mass m, and charge $\pm e$. The GRPIC simulations begin with vacuum, and plasma particles are injected with density proportional to the local parallel electric field as a proxy for the electron-positron discharge (see [61] for details of the injection scheme).

We set the dimensionless magnetic field strength at the event horizon $B_0 = r_g/r_L$, with r_L the Larmor radius. For the gravitational collapse of a NS it implies $B_0 \sim 10^{14}(M/M_\odot)(B/10^{12}\ G)$. In this work we scale it down, and consider $B_0 \sim 10^4, 3 \times 10^4, 10^5$ (Table 5.1). We show that our results are independent of B_0, as long as the plasma is highly magnetized. The characteristic minimum plasma density required to support the rotating magnetosphere is the Goldreich-Julian number density [43], $n_0 = \Omega_H B_0/(2\pi ce)$, where $\Omega_H = acr_g/[r_H^2 + (r_g a)^2]$ is the angular velocity of the event horizon radius $r_H = r_g(1 + \sqrt{1 - a^2})$. It implies the characteristic magnetization $\sigma_0 = B_0^2/(4\pi n_0 mc^2) = (1/2)(\omega_B/\Omega_H) = (1/4)(\omega_p/\Omega_H)^2 \gg 1$, where $\omega_p = (4\pi n_0 e^2/m)^{1/2}$ is the plasma frequency and $\omega_B = c/r_L$ the Larmor frequency. We have preserved the astrophysically relevant hierarchy of scales $r_L \ll \lambda_p \ll r_g$, and $\Omega_H \ll \omega_p \ll \omega_B$, where $\lambda_p = c/\omega_p$ is the plasma skin depth.

Table 5.1: Summary of the simulation parameters. For all GRRMHD runs the diffusivity is $\eta = 10^{-5}$. For MHD runs $N_r \times N_\theta \times N_\phi$ refers to the effective resolution. Runs with $N_\phi = 1$ are axisymmetric, while those with $N_\phi > 1$ refer to 3D simulations. All models have spin $a = 0.99$ except VAC0, which has $a = 0$.

Model	r_L	λ_p	$N_r \times N_\theta \times N_\phi$
VAC0	—	—	$9600 \times 8016 \times 1$
VAC1	—	—	$9600 \times 8016 \times 1$
GRPIC1	1×10^{-5}	3×10^{-3}	$2880 \times 2160 \times 1$
GRPIC2	3×10^{-5}	6×10^{-3}	$2880 \times 2160 \times 1$
GRPIC3	1×10^{-4}	1×10^{-2}	$2880 \times 2160 \times 1$
GRRMHD1	—	—	$6144 \times 3072 \times 1$
GRRMHD2	—	—	$3072 \times 1536 \times 1536$

The computational domain of the axisymmetric GRPIC simulations covers $0.99 \leq r \leq 75$, and $0 \leq \theta \leq \pi$. Simulations for each of the (3) magnetic field strengths were performed at two resolutions to check for numerical convergence (a total of 6 kinetic plasma simulations): (i) $N_r \times N_\theta = 1440 \times 1080$, and (ii) $N_r \times N_\theta = 2880 \times 2160$. The grid is uniformly spaced in $\log r$ and $\cos\theta$, so that resolution is concentrated near the BH horizon, and the equator. We check that the plasma skin depth is well resolved a posteriori, since the plasma density is determined self-consistently. Electromagnetic fields are damped and particles are absorbed at the outer boundary in order to mimic an outflow boundary condition. For $r \leq r_H$ all characteristics are inward, and causality prevents waves and plasma from escaping. Therefore, the equations are solved without modification at the event horizon, and no boundary condition is imposed there.

The GRRMHD simulations are performed using the Black Hole Accretion Code [159–161]. A minimum density is set throughout the domain such that the magnetization $\sigma \gg 1$, and the plasma is nearly force-free. We set a constant and uniform diffusivity $\eta = 10^{-5}$, so that the Lundquist number $S = v_A L/\eta \approx \eta^{-1} = 10^5$ is above the plasmoid instability limit $S > 10^4$ [64], where $v_A \approx c$ is the Alfvén speed and $L \approx r_e - r_g \approx 1$ is the characteristic length of the current-sheet inside the ergosphere.

The computational domain of the GRRMHD simulations covers $0.99 \leq r \leq 200$, $0 \leq \theta \leq \pi$, and $0 \leq \phi \leq 2\pi$. By adding AMR, we increase resolution at the current-sheet to assure convergence. The base grid, and additional AMR blocks are uniformly spaced in $\log r$, and ϕ, while the θ grid is concentrated near the equator.

5.3 Global Dynamics

The evolution of all simulations is qualitatively similar. In GRPIC simulations, strong electric fields induced by spacetime rotation near the event horizon trigger particle injection which rapidly fills the magnetosphere with plasma up to a density $n \sim \mathcal{M} n_0$, where $\mathcal{M} \sim$ few is the multiplicity, while GRRMHD simulations begins with a static low-density plasma throughout the domain. In the ergosphere plasma is dragged into co-rotation with the BH, bending field-lines in the ϕ direction and inflating the poloidal magnetic field. As field-lines extend in the radial direction, flux on the horizon moves toward the equator, and some loops which close inside the ergosphere are pushed

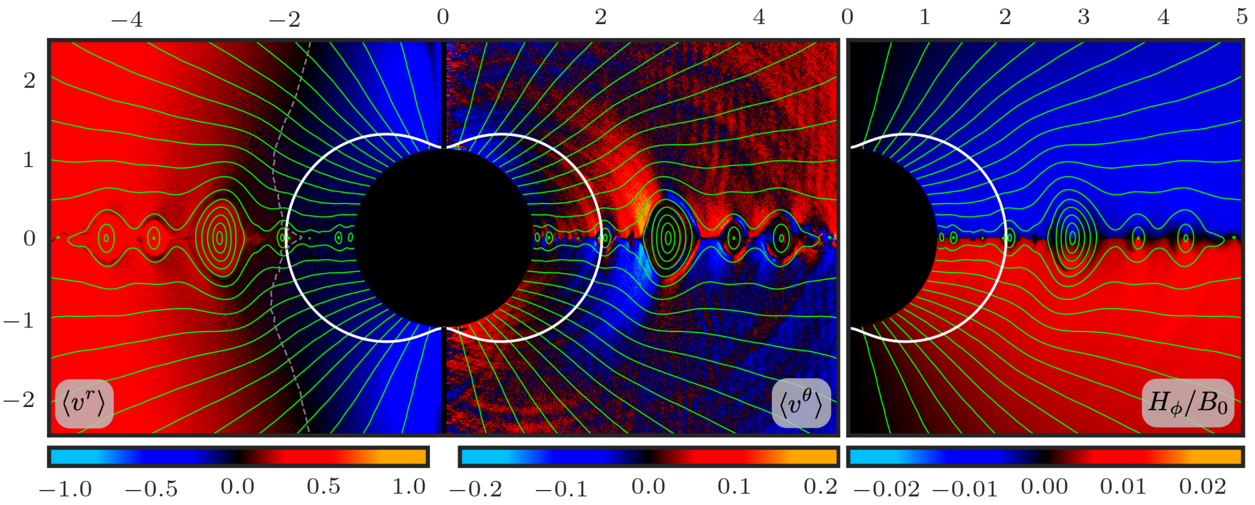

Figure 5.1: Reconnecting magnetosphere in the FIDO frame (GRPIC1) at $t = 100\ r_g/c$. Green curves show poloidal magnetic flux surfaces, and white curves show the boundary of the ergosphere. The black circle is the interior of the BH event horizon. Left: Color shows radial and θ components of the bulk plasma 3-velocity in the orthonormal tetrad basis. The grey dashed curve indicates the stagnation surface defined by $\langle v^r \rangle = 0$. Right: Azimuthal component of the auxiliary field $\boldsymbol{H}$.

into the BH. After $t \approx 40\ r_g/c$, the dipole has opened into a split-monopole with $\boldsymbol{\Omega} \cdot \boldsymbol{B}_p > 0$ in both hemispheres, where $\boldsymbol{\Omega}$ is the angular velocity vector of the BH and $\boldsymbol{B}_p$ is the poloidal magnetic field. The field-lines rotate rigidly with angular velocity $\Omega_F = \Omega_H/2$, in agreement with force-free solutions [60]. The toroidal magnetic field H_ϕ has opposite sign to B^r in each hemisphere (Fig. 5.1, right) indicating swept-back field-lines, where $\boldsymbol{H} = \alpha \boldsymbol{B} - \boldsymbol{\beta} \times \boldsymbol{D}$, $\boldsymbol{\beta}$ is the shift, and $\boldsymbol{D}$ the electric field. A well defined MHD stagnation surface is established, separating regions of inflow $\langle v^r \rangle < 0$, and outflow $\langle v^r \rangle > 0$ (Fig. 5.1, dashed grey curve). Here $\langle \ldots \rangle$ indicates averaging over the particles in a single grid-cell.

5.4 Reconnection Dynamics

Magnetic reconnection is first triggered near the stagnation surface in both GRPIC and GRRMHD, and rapidly spreads along the entire current-sheet. The onset of reconnection occurs later in GRRMHD $t \sim 70\ r_g/c$, compared to GRPIC $t \sim 30\ r_g/c$. However, once the current-sheet is sufficiently thin the tearing instability develops and a chain of self-similar plasmoids forms.

Generally plasmoids born inside the stagnation surface move slowly ($v < 0.1c$) toward the event horizon and fall into the BH, while those born outside are ejected from the magnetosphere and accelerate to relativistic velocities ($v \approx c$). Therefore, we identify the stagnation surface at the equator as a main site of field-line "pinching", and a primary X-point in the global magnetosphere. Occasionally plasmoids born inside the stagnation surface have sufficient kinetic energy to escape.

We analyzed the reconnection rate for all simulations by measuring the inflow velocity of flux into the current-sheet. The analysis is performed by transforming the electric and magnetic field components into the locally Minkowski reference frame of the FIDO. The inflow velocity is then calculated using the component of $\boldsymbol{E} \times \boldsymbol{B}$ in the direction perpendicular to the current-sheet, and avoiding plasmoids. We confirm $\sigma \gg 1$ in the upstream plasma, so that $v_A/c = (\sigma/(\sigma+1))^{1/2} \approx 1$, and the reconnection is in the relativistic regime. All components of the magnetic field change sign at the current-sheet, indicating zero guide-field reconnection.

The measured reconnection rate in the GRPIC simulations $v_{\rm rec} \approx 0.1c$ is consistent with studies of magnetic reconnection in relativistic collisionless plasmas [65–67]. For the GRRMHD simulations the high Lundquist number $S \approx 10^5 \gg 10^4$ ensures that the reconnection occurs deep in the plasmoid dominated regime [162]. The reconnection rate in resistive MHD at high Lundquist number is $v_{\rm rec} \approx 0.01 v_A$ [64], which is confirmed by our measured $v_{\rm rec} \approx 0.01c - 0.02c$ and is consistent with other studies in relativistic MHD [163] where the reconnection dynamics is modified by $v_A \rightarrow c$. In GRPIC simulations the plasmoids grow at a rate $\sim 0.1c$, until they are ejected and the growth is suppressed as they reach relativistic velocities. Thus the plasmoids are on average smaller in GRRMHD simulations (Fig. 5.2), where the growth rate $\sim 0.01c$ is smaller.

Reconnection in collisionless pair plasma occurs due to kinetic effects resulting from the divergence of the anisotropic electron pressure tensor, which plays the role of an effective non-uniform diffusivity [164]. Therefore, the difference in reconnnection rates between the two formalisms can be attributed to the use of a uniform diffusivity in GRRMHD as a proxy for kinetic effects, representing the simplest model of reconnection and plasmoid formation, while in GRPIC the dissipation at the current-sheet is determined from first principles.

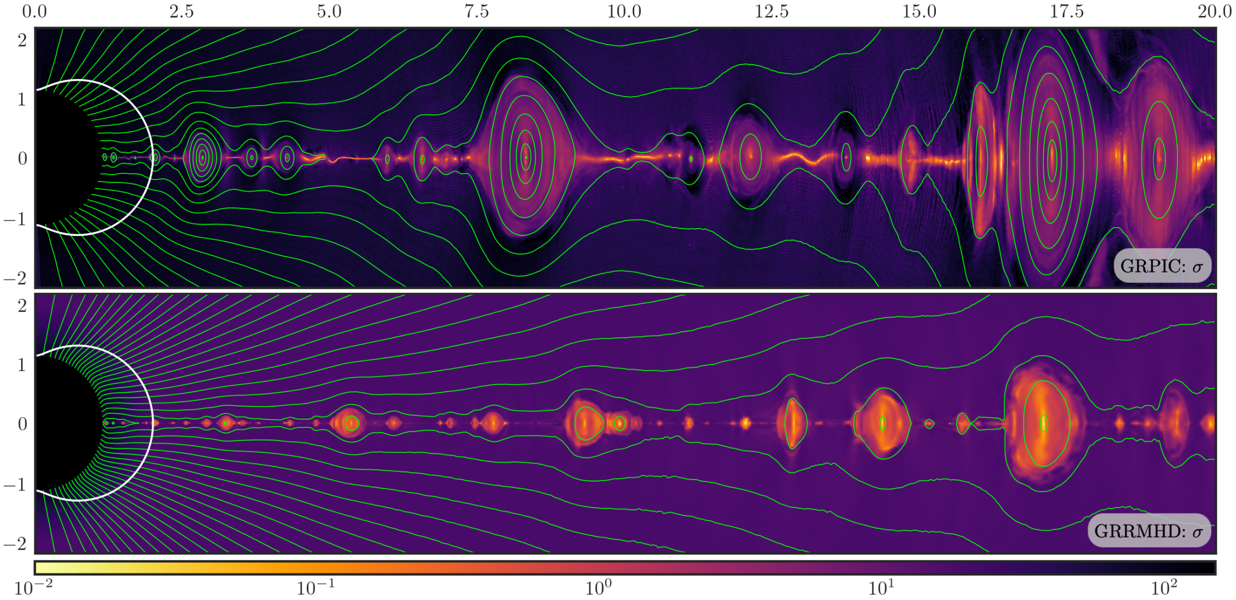

Figure 5.2: Different realizations of the reconnecting magnetosphere in the FIDO frame. Color shows the cold plasma magnetization σ. Top: GRPIC1 at $t = 100\ r_g/c$, $\sigma = B^2/(4\pi mnc^2)$. Bottom: GRRMHD1 at $t = 311\ r_g/c$, $\sigma = B^2/(4\pi\rho c^2)$. The GRPIC simulation (top) displays larger plasmoids than GRRMHD (bottom) due to the faster reconnection rate.

The reconnection is collisionless when the plasma skin depth λ_p is larger than the elementary current-sheet width in the resistive-MHD chain $w \sim 100\eta/v_A \sim 100\eta/c$ [64, 165], where η is the diffusivity due to coulomb collisions of pairs. Since our simulations do not include the detailed pair production and collision physics, we estimate analytically when this condition is satisfied (see supplement). The temperature of the reconnection layer is estimated by assuming the combined pressure of radiation and pairs is comparable to $B^2/(8\pi)$. The density of pairs is then given by the annihilation balance. We find that the reconnection is evidently collisionless when $B \ll 10^{12}$ G. However, if the magnetic field is very strong $B \gtrsim 10^{12}$ G, or pair production is very efficient, the separation between the two regimes is less clear, and a self consistent calculation is required to determine the reconnection rate. However, even in this intermediate case, the GRRMHD simulations described in this work with uniform η provide a lower limit on the reconnection rate.

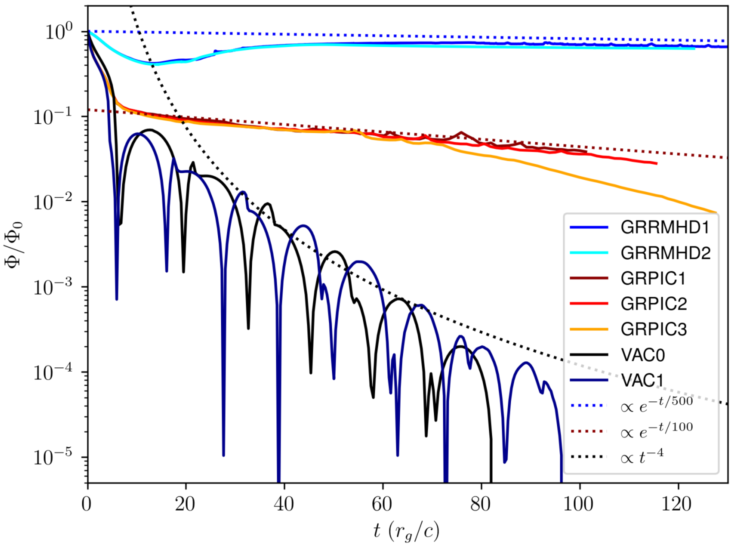

Figure 5.3: Flux on the event horizon vs time for vacuum (power law decay), collisional MHD plasma (exponential decay), and collisionless plasma (faster exponential decay).

5.5 Flux Decay Rate

The magnetic flux on the event horizon Φ decays quasi-exponentially with time (Fig. 5.3). In GRPIC simulations the flux decays with characteristic timescale $\tau \approx 100\ r_g/c$, and in GRRMHD simulations $\tau \approx 500\ r_g/c$ (Fig. 5.3). The difference in timescales can be attributed to different reconnection rates in these formalisms, which differ by a factor ~ 5. Since B and $n \propto B$ decay exponentially, all components of the stress-energy tensor become vanishingly small at late times and the no-hair theorem is satisfied. We calculate the charge of the BH at the end of the GRPIC simulation as $Q = (1/4\pi) \int D^r \sqrt{\gamma} \mathrm{d}\theta \mathrm{d}\phi$ at $r = r_H$ and find that $Q = 0$, so the final state is a Kerr BH. The decay timescale converges with decreasing r_L/r_H in GRPIC simulation (Fig. 5.3), indicating the correct asymptotic behaviour with a sufficient separation of scales. Therefore, the measured decay timescale is independent of B, as long as the plasma is highly magnetized, $\sigma \gg 1$, and finite Larmor radius corrections are negligible, $r_L/r_g \ll 1$.

The evolution of Φ is estimated analytically using Faraday's law, and assuming a constant reconnection rate on the equator at the stagnation surface (see supplement) [166]. In this toy model Φ decays exponentially on a timescale $\tau \approx 3r_g/\langle v^\theta \rangle$, with $\langle v^\theta \rangle$ the θ component of the plasma 3-

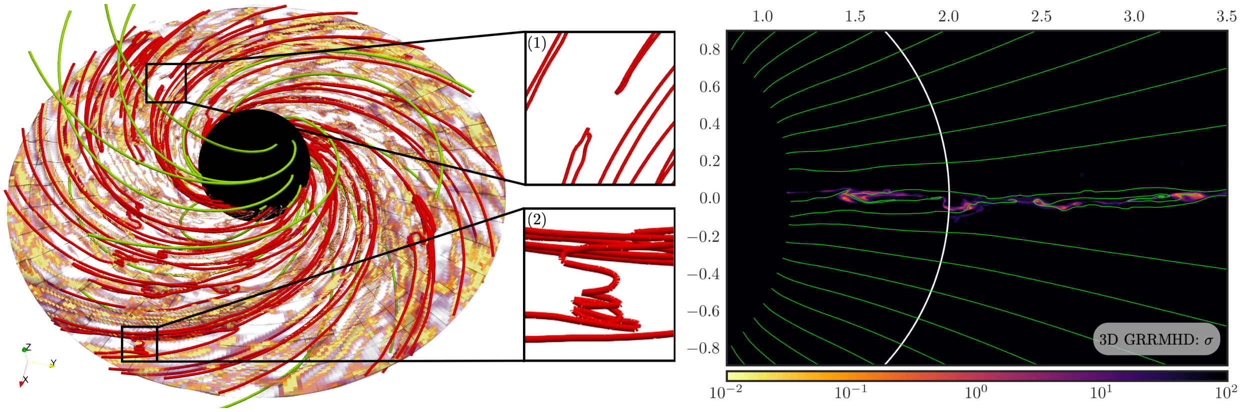

Figure 5.4: Reconnecting magnetosphere in 3D (GRRMHD2) at $t = 118\ r_g/c$. Left: Volume rendering shows $\sigma = B^2/(4\pi\rho c^2)$, green tubes are magnetic field-lines which penetrate the event horizon, red tubes are magnetic field-lines which are reconnecting in the current-sheet. Right: 2D slice of GRRMHD2 in the $\phi = 0$ half-plane. Color shows σ, green curves are magnetic field-lines in the $\phi = 0$ half-plane. The picture highlights the non-axisymmetric nature of reconnection in 3D, yet still displays similar fundamental structures — X-points (inset 1), and helical winding of magnetic field-lines in plasmoids (flux ropes) (inset 2).

velocity in the orthonormal tetrad basis (Fig. 5.1). For example, in GRPIC1 $\langle v^\theta \rangle \approx 0.02 - 0.04c$ at the current-sheet implies $\tau \sim 100\ r_g/c$, consistent with Fig. 5.3. The local reconnection rate observed by the FIDO is estimated by taking into account time dilation at the stagnation surface. For GRPIC1 it implies $\langle v^\theta \rangle/(c\alpha) \sim 0.05$, with α evaluated on the equator at the stagnation surface, consistent with the measured values.

In 3D (GRRMHD2), the balding proceeds similarly to the axisymmetric simulations (Fig. 5.3, cyan curve), but the plasmoid instability leads to non-axisymmetric (in ϕ) structures. Therefore, 3D plasmoids, or flux tubes of tangled field-lines with a finite extent in ϕ, generally display more complex topologies than those in 2D (Fig. 5.4).

5.6 Emission

The flux of conserved energy through spherical shells, as seen by an observer at infinity is comparable in magnitude to $L_{\rm BZ} = 0.053\Omega_H^2\Phi^2/(4\pi c)$ [167], indicating successful activation of the Blandford-Znajek mechanism (see supplement) [60]. Large fluctuations up to several $L_{\rm BZ}$ are seen at the locations of plasmoids. We observe the emission of fast modes from plasmoid mergers (Fig. 5.2). In the high$-\sigma$ limit, and where $B \sim 10^6$ G, these fast modes correspond to vacuum electromagnetic waves in the radio band, and could be observed as coherent radio emission [168]. The escaping giant plasmoids (Fig. 5.2) may shock the upstream wind, resulting in coherent synchrotron maser emission [169, 170]. For collisionless plasma, we measure the total dissipative power as seen by an observer at infinity $L_{\rm diss,\infty} \approx 0.4 L_{\rm BZ}$. When the magnetic field is strong ($B \gtrsim 10^6$ G) as expected in BH-NS mergers, the reconnection is radiative and most of the dissipated magnetic energy will go into photons. In this regime, $L_{\rm diss,\infty} \approx 0.4 L_{\rm BZ} \sim 4 \times 10^{45} M_{10\odot}^2 B_{12}^2$ erg s^{-1} corresponds to emission in the hard X-ray band [171]. We also observe a population of negative energy-at-infinity particles localized in the current sheet inside the ergosphere. They contribute to $\boldsymbol{J} = (c/4\pi)\nabla \times \boldsymbol{H}$, and some are advected into the BH with plasmoids — an instance of the Penrose process facilitated by magnetic reconnection [61, 172].

5.7 Discussion

We considered Kerr BH's endowed with highly magnetized plasma-filled magnetospheres. We find that: (i) The no-hair theorem holds, in the sense that all components of the stress-energy tensor decay exponentially in time, (ii) Reconnection occurs at the universal rate when measured in the locally Minkowski frame of the FIDO, (iii) The lifetime of the magnetic field on the event horizon is controlled by the local reconnection rate measured by the FIDO in concert with other global effects, and (iv) The final state is a Kerr BH with charge $Q = 0$. Balding BHs resulting from the merger or collapse of compact objects should appear as a spectacular source of hard X-rays for a short duration, similar to the flares of galactic magnetars. Observation of the X-rays requires a clean environment around the BH. It is possible during the gravitational collapse of a rotationally supported NS, and in BH-NS mergers with a high mass ratio, so that the NS falls through the event horizon without forming a torus or disk. Gamma-ray bursts and other collapsars may be different to the scenario described in this work, depending on how much matter surrounds the newly formed BH. The decay of magnetic flux on the event horizon may also explain powerful X-ray and near-infrared flares and hot spots [173] driven by plasmoid-regulated reconnection in magnetically dominated supermassive BH magnetospheres [162, 172]. The faster reconnection rate in collisionless plasma implies that larger plasmoids, powering a flare near the BH, can form in a shorter time and in this way regulate the typical flare duration.

Conclusion

This dissertation explored the dynamics of strongly magnetized neutron stars and black holes by using a combination of theoretical and computational techniques.

Chapter 2 studied the magnetic field evolution of neutron stars in axisymmetry. We developed from scratch a numerical code which includes the effects of Hall drift, ohmic diffusion, and elastic deformation in the crust. We also model the drift of superconducting flux tubes (using the Jones prescription [8]), and vortices in the liquid core. We enforce the correct hydromagnetic equilibrium in the core. We find that (i) The Hall attractor found by Gourgouliatos and Cumming in the crust also exists for B-fields which penetrate the core. (ii) If the flux tube drift is fast in the core, the pulsar magnetic fields are depleted on the ohmic timescale ($\sim$ 150 Myr for hot neutron stars, or $\sim$ 1.8 Gyr for cold neutron stars such as recycled pulsars, depending on impurity levels). (iii) The outward motion of superfluid vortices during the rapid spin-down of a young highly magnetized pulsar, can partially expel magnetic flux from the core when $B \lesssim 10^{13}$ G. Future work should aim to resolve theoretical uncertainties in the flux tube equation of motion, and develop a more detailed understanding of the vortex flux tube interactions (see e.g. [174, 175]). Clarifying these issues will enable detailed modeling of pulsar magnetic fields which will shed light on the origin of millisecond pulsars. The models will also be essential to interpret NICER (neutron star interior composition explorer) observations of X-ray hot spots on millisecond pulsars [176].

In Chapter 3 we developed a theoretical model to explain the radio emission anomaly coincident with the 2016 glitch in Vela rotation [40]. We show how a star quake could simultaneously trigger a glitch in the neutron star interior and ignite a powerful electron-positron discharge in the magnetosphere which switches off the pulsar radio emission. As part of this work we developed the first numerical simulations of a neutron star quake. Our code follows the evolution of elastic waves in the neutron star crust, and Alfvén waves in the magnetosphere, as well as the magnetic coupling to the the liquid core. The lifetime of the star quake is controlled by crust-core coupling. Therefore, the duration of observed star quakes may provide insights to the neutron star interior physics by means of seismology. The major uncertainty in this work is the origin of the star quake. Vela's magnetic field is too weak to break the crust, and its rotation is too slow to significantly deform it. Nevertheless, a star quake is the only plausible way to couple the neutron star interior (where the glitch occurred) to the observed radio emission disturbance in the magnetosphere. Future multi-wavelength observations of Vela at the time of the glitch will be crucial to understand the phenomenon. The numerical models developed in this work can also be applied to magnetar quakes which are thought to produce X-ray bursts and the observed galactic fast radio burst (FRB) [12].

In Chapter 4 we present an extreme high resolution kinetic plasma simulation of a pulsar magnetosphere using the pigeon code [55, 56]. For the first time, we resolve regions of wave excitation by electric discharges and instabilities in a global magnetosphere. The discharge waves may be responsible for the observed pulsar radio emission [50], and the streaming instabilities could produce exotic radio emission from the outer magnetosphere of energetic pulsars like the Crab [177]. For the first time we observe the non-linear interaction of electric discharges which occur at different altitudes on the same magnetic field lines. Future work should investigate the interacting discharges at higher (more realistic) pair multiplicities. It will also be essential to study the development of plasma streaming instabilities in local simulations with realistic $e^{\pm}$ pair production. The simulation in this work was restricted to aligned rotators in 2D axisymmetry. It will be important to understand the radio emission of inclined rotators in 3D kinetic models.

In Chapter 5 we modeled the evolution of plasma magnetospheres on Kerr black holes. We performed general relativistic kinetic plasma simulations with the GRZeltron code [61], and general relativistic resistive magnetohydrodynamics simulations with the BHAC code [159–161]. We showed that a dipole magnetic field on the event horizon opens into a split-monopole and reconnects in a plasmoid-unstable current-sheet. The plasmoids are ejected from the magnetosphere, or swallowed by the black hole. The no-hair theorem is satisfied, in the sense that all components of the stress-energy tensor decay exponentially in time. We measure the decay time of magnetic flux on the event horizon for plasmoid-dominated reconnection in collisionless and collisional plasma. Future work should investigate the emission of balding black holes in more detail, including the possible emission of FRBs during the gravitational collapse of a strongly magnetized neutron star. The balding solution was also found to be important in simulations of magnetically arrested accretion onto supermassive black holes [178, 179]: The simulations show ‘balding episodes’ during which the accretion flow is halted, and the decay of magnetic flux on the event horizon is controlled by the physics of magnetic reconnection (as described in this work). A detailed understanding of the radiation physics during balding episodes may provide insights into the multi-wavelength flares of Sgr A* and M87 [178].

References

[1] R. N. Manchester, G. B. Hobbs, A. Teoh, and M. Hobbs, “The Australia Telescope National Facility Pulsar Catalogue,” *The Astrophysical Journal*, vol. 129, pp. 1993–2006, Apr. 2005.

[2] S. A. Olausen and V. M. Kaspi, “The McGill Magnetar Catalog,” *The Astrophysical Journal Supplement Series*, vol. 212, p. 6, May 2014.

[3] R. W. Romani, “A unified model of neutron-star magnetic fields,” *Nature*, vol. 347, no. 6295, pp. 741–743, Oct. 1990.

[4] A. Cumming, E. G. Zweibel, and L. Bildsten, “Magnetic Screening in Accreting Neutron Stars,” *The Astrophysical Journal*, vol. 557, no. 2, pp. 958–966, Aug. 2001, arXiv: astro-ph/0102178.

[5] A. R. Choudhuri and S. Konar, “Diamagnetic Screening of the Magnetic Field in Accreting Neutron Stars,” *Monthly Notices of the Royal Astronomical Society*, vol. 332, no. 4, pp. 933–944, Jun. 2002, arXiv: astro-ph/0108229.

[6] D. J. B. Payne and A. Melatos, “Burial of the polar magnetic field of an accreting neutron star - I. Self-consistent analytic and numerical equilibria,” *Monthly Notices of the Royal Astronomical Society*, vol. 351, pp. 569–584, Jun. 2004.

[7] M. Ruderman, T. Zhu, and K. Chen, “Neutron Star Magnetic Field Evolution, Crust Movement, and Glitches,” *The Astrophysical Journal*, vol. 492, pp. 267–280, Jan. 1998.

[8] P. B. Jones, “Type II superconductivity and magnetic flux transport in neutrons stars,” *Monthly Notices of the Royal Astronomical Society*, vol. 365, no. 1, pp. 339–344, Jan. 2006, arXiv: astro-ph/0510396.

[9] C. Thompson and R. C. Duncan, “The Soft Gamma Repeaters as Very Strongly Magnetized Neutron Stars. II. Quiescent Neutrino, X-Ray, and Alfven Wave Emission,” *The Astrophysical Journal*, vol. 473, p. 322, Dec. 1996.

[10] V. M. Kaspi and A. Beloborodov, “Magnetars,” *Annual Review of Astronomy and Astrophysics (in press)*, Feb. 2017, arXiv: 1703.00068.

[11] A. C. Collazzi *et al.*, “The Five Year Fermi/GBM Magnetar Burst Catalog,” *The Astrophysical JournalS*, vol. 218, no. 1, p. 11, May 2015.

[12] C. D. Bochenek, V. Ravi, K. V. Belov, G. Hallinan, J. Kocz, S. R. Kulkarni, and D. L. McKenna, “A fast radio burst associated with a galactic magnetar,” *Nature*, vol. 587, no. 7832, pp. 59–62, 2020.

[13] R. Perna and J. A. Pons, “A unified model of the magnetar and radio pulsar bursting phenomenology,” *The Astrophysical Journal*, vol. 727, no. 2, p. L51, Feb. 2011, arXiv: 1101.1098.

[14] A. M. Beloborodov and Y. Levin, “Thermoplastic waves in magnetars,” *The Astrophysical Journal*, vol. 794, no. 2, p. L24, Oct. 2014, arXiv: 1406.4850.

[15] X. Li, Y. Levin, and A. M. Beloborodov, “Magnetar Outbursts from Avalanches of Hall Waves and Crustal Failures,” *arXiv:1606.04895 [astro-ph]*, Jun. 2016, arXiv: 1606.04895.

[16] C. Thompson, H. Yang, and N. Ortiz, “Global Crustal Dynamics of Magnetars in Relation to Their Bright X-Ray Outbursts,” *The Astrophysical Journal*, vol. 841, no. 1, p. 54, 2017.

[17] N. Chamel and P. Haensel, “Physics of Neutron Star Crusts,” *Living Reviews in Relativity*, vol. 11, no. 1, Dec. 2008, arXiv: 0812.3955.

[18] P. B. Jones, “Neutron star magnetic field decay - Hall drift and Ohmic diffusion,” *Monthly Notices of the Royal Astronomical Society*, vol. 233, pp. 875–885, Aug. 1988.

[19] P. Goldreich and A. Reisenegger, “Magnetic field decay in isolated neutron stars,” *The Astrophysical Journal*, vol. 395, pp. 250–258, Aug. 1992.

[20] A. M. Beloborodov and X. Li, “Magnetar heating,” *The Astrophysical Journal*, vol. 833, no. 2, p. 261, Dec. 2016.

[21] R. Hollerbach and G. Rüdiger, “Hall drift in the stratified crusts of neutron stars,” *Monthly Notices of the Royal Astronomical Society*, vol. 347, pp. 1273–1278, Feb. 2004.

[22] J. A. Pons and U. Geppert, “Magnetic field dissipation in neutron star crusts: From magnetars to isolated neutron stars,” *Astronomy and Astrophysics*, vol. 470, pp. 303–315, Jul. 2007.

[23] D. Viganò, J. A. Pons, and J. A. Miralles, “A new code for the Hall-driven magnetic evolution of neutron stars,” *Computer Physics Communications*, vol. 183, no. 10, pp. 2042–2053, Oct. 2012, arXiv: 1204.4707.

[24] K. N. Gourgouliatos and A. Cumming, “Hall Effect in Neutron Star Crusts: Evolution, Endpoint and Dependence on Initial Conditions,” *Monthly Notices of the Royal Astronomical Society*, vol. 438, no. 2, pp. 1618–1629, Feb. 2014, arXiv: 1311.7004.

[25] F. Castillo, A. Reisenegger, and J. A. Valdivia, "Magnetic field evolution and equilibrium configurations in neutron star cores: The effect of ambipolar diffusion," *Monthly Notices of the Royal Astronomical Society*, vol. 471, no. 1, pp. 507–522, Oct. 2017, arXiv: 1705.10020.

[26] A. Y. Potekhin, J. A. Pons, and D. Page, "Neutron stars - cooling and transport," *SSRv*, vol. 191, no. 1-4, pp. 239–291, Oct. 2015.

[27] G. Baym and C. Pethick, "Neutron stars.," *Annual Review of Nuclear and Particle Science*, vol. 25, pp. 27–77, 1975.

[28] P. B. Jones, "Neutron superfluid spin-down and magnetic field decay in pulsars," *Monthly Notices of the Royal Astronomical Society*, vol. 253, pp. 279–286, Nov. 1991.

[29] M. A. Ruderman and P. G. Sutherland, "Rotating Superfluid in Neutron Stars," *The Astrophysical Journal*, vol. 190, pp. 137–140, May 1974.

[30] G. Srinivasan, D. Bhattacharya, A. G. Muslimov, and A. J. Tsygan, "A novel mechanism for the decay of neutron star magnetic fields," *Current Science*, vol. 59, pp. 31–38, Jan. 1990.

[31] M. Ruderman, "A Biography of the Magnetic Field of a Neutron Star," *arXiv:astro-ph/0410607*, Oct. 2004, arXiv: astro-ph/0410607.

[32] M. E. Gusakov, "Force on proton vortices in superfluid neutron stars," *Mon Not R Astron Soc*,

[33] G. Hobbs, A. G. Lyne, and M. Kramer, "An analysis of the timing irregularities for 366 pulsars," *Monthly Notices of the Royal Astronomical Society*, vol. 402, no. 2, pp. 1027–1048, Feb. 2010.

[34] A. Lyne, G. Hobbs, M. Kramer, I. Stairs, and B. Stappers, "Switched magnetospheric regulation of pulsar spin-down," *Science*, vol. 329, no. 5990, pp. 408–412, Jul. 2010.

[35] V. Radhakrishnan and R. N. Manchester, "Detection of a Change of State in the Pulsar PSR 0833-45," *Nature*, vol. 222, pp. 228–229, Apr. 1969.

[36] R. N. Manchester, "Pulsar glitches and their impact on neutron-star astrophysics," *arXiv:1801.04332 [astro-ph]*, Jan. 2018.

[37] C. M. Espinoza, A. G. Lyne, B. W. Stappers, and M. Kramer, "A study of 315 glitches in the rotation of 102 pulsars," *Monthly Notices of the Royal Astronomical Society*, vol. 414, no. 2, pp. 1679–1704, Jun. 2011.

[38] A. Melatos, C. Peralta, and J. S. B. Wyithe, “Avalanche Dynamics of Radio Pulsar Glitches,” *The Astrophysical Journal*, vol. 672, no. 2, p. 1103, Jan. 2008.

[39] P. W. Anderson and N. Itoh, “Pulsar glitches and restlessness as a hard superfluidity phenomenon,” *Nature*, vol. 256, no. 5512, p. 25, Jul. 1975.

[40] J. Palfreyman, J. M. Dickey, A. Hotan, S. Ellingsen, and W. van Straten, “Alteration of the magnetosphere of the Vela pulsar during a glitch,” *Nature*, vol. 556, no. 7700, pp. 219–222, Apr. 2018.

[41] R. P. Mignani, R. Paladino, B. Rudak, A. Zajczyk, A. Corongiu, A. de Luca, W. Hummel, A. Possenti, U. Geppert, M. Burgay, and G. Marconi, “The First Detection of a Pulsar with ALMA,” *The Astrophysical Journal Letters*, vol. 851, no. 1, L10, p. L10, Dec. 2017. arXiv: `1708.02828 [astro-ph.HE]`.

[42] A. Philippov and M. Kramer, “Pulsar Magnetospheres and Their Radiation,” *ARAA*, vol. 60, pp. 495–558, Aug. 2022.

[43] P. Goldreich and W. H. Julian, “Pulsar Electrodynamics,” *The Astrophysical Journal*, vol. 157, p. 869, Aug. 1969.

[44] M. A. Ruderman and P. G. Sutherland, “Theory of pulsars - Polar caps, sparks, and coherent microwave radiation,” *The Astrophysical Journal*, vol. 196, pp. 51–72, Feb. 1975.

[45] J. J. Barnard and J. Arons, “Wave Propagation in Pulsar Magnetospheres: Refraction of Rays in the Open Flux Zone,” *The Astrophysical Journal*, vol. 302, p. 138, Mar. 1986.

[46] Y. E. Lyubarsky, “Induced wave scattering and transformation in pulsar magnetospheres,” *Astron. Lett.*, vol. 19, no. 6, pp. 208–216, Jun. 1993.

[47] Y. Lyubarskii and S. Petrova, *Astrophy. Space Sci.*, vol. 262, no. 4, pp. 379–389, 1998.

[48] V. S. Beskin and A. A. Philippov, “On the mean profiles of radio pulsars – I. Theory of propagation effects,” *Mon. Not. R. Astron Soc.*, vol. 425, no. 2, pp. 814–840, Sep. 2012.

[49] A. N. Timokhin, “Time-dependent pair cascades in magnetospheres of neutron stars – I. Dynamics of the polar cap cascade with no particle supply from the neutron star surface,” *Mon. Not. R. Astron Soc.*, vol. 408, no. 4, pp. 2092–2114, Oct. 2010.

[50] A. Philippov, A. Timokhin, and A. Spitkovsky, “Origin of Pulsar Radio Emission,” *Physical Review Letters*, vol. 124, no. 24, p. 245 101, Jun. 2020.

[51] D. B. Melrose, M. Z. Rafat, and A. Mastrano, “A rotation-driven pulsar radio emission mechanism,” *Monthly Notices of the Royal Astronomical Society*, vol. 500, no. 4, pp. 4549–4559, Jan. 2021. arXiv: `2006.15487 [astro-ph.HE]`.

[52] A. Y. Chen and A. M. Beloborodov, "Electrodynamics of axisymmetric pulsar magnetosphere with electron-positron discharge: A numerical experiment," *The Astrophysical Journal*, vol. 795, no. 1, p. L22, Oct. 2014, arXiv: 1406.7834.

[53] A. A. Philippov, B. Cerutti, A. Tchekhovskoy, and A. Spitkovsky, "Ab-initio pulsar magnetosphere: The role of general relativity," *The Astrophysical Journal*, vol. 815, no. 2, p. L19, Dec. 2015.

[54] A. A. Philippov and A. Spitkovsky, "Ab-Initio Pulsar Magnetosphere: Particle acceleration in Oblique Rotators and High-energy Emission Modeling," *The Astrophysical Journal*, vol. 855, no. 2, p. 94, Mar. 2018.

[55] R. Hu, A. M. Beloborodov, and A. Y. Chen, *arXiv:210903927*, Sep. 2021.

[56] R. Hu and A. M. Beloborodov, "Axisymmetric pulsar magnetosphere revisited," *arXiv:210903935*, Sep. 2021.

[57] A. N. Timokhin and J. Arons, "Current flow and pair creation at low altitude in rotation-powered pulsars' force-free magnetospheres: Space charge limited flow," *Mon. Not. R. Astron Soc.*, vol. 429, no. 1, pp. 20–54, Feb. 2013.

[58] K. S. Thorne, *Black holes and time warps: Einstein's outrageous legacy*. 1994.

[59] C. W. Misner, K. S. Thorne, and J. A. Wheeler, *Gravitation*. 1973.

[60] R. D. Blandford and R. L. Znajek, "Electromagnetic extraction of energy from Kerr black holes.," *Monthly Notices of the Royal Astronomical Society*, vol. 179, pp. 433–456, May 1977.

[61] K. Parfrey, A. Philippov, and B. Cerutti, "First-principles plasma simulations of black-hole jet launching," *Physical Review Letters*, vol. 122, no. 3, 2019.

[62] B. Crinquand, B. Cerutti, A. Philippov, K. Parfrey, and G. Dubus, "Multidimensional Simulations of Ergospheric Pair Discharges around Black Holes," *Physical Review Letters*, vol. 124, no. 14, 145101, p. 145 101, Apr. 2020.

[63] M. Lyutikov and J. C. McKinney, "Slowly balding black holes," *Phys. Rev. D*, vol. 84, no. 8, p. 084 019, Oct. 2011, arXiv: 1109.0584.

[64] A. Bhattacharjee, Y.-M. Huang, H. Yang, and B. Rogers, "Fast reconnection in high-Lundquist-number plasmas due to the plasmoid Instability," *Physics of Plasmas*, vol. 16, no. 11, 112102, p. 112 102, Nov. 2009.

[65] L. Sironi and A. Spitkovsky, “Relativistic Reconnection: An Efficient Source of Non-thermal Particles,” *The Astrophysical Journal Letters*, vol. 783, no. 1, L21, p. L21, Mar. 2014.

[66] F. Guo, H. Li, W. Daughton, and Y.-H. Liu, “Formation of hard power laws in the energetic particle spectra resulting from relativistic magnetic reconnection,” *Physical Review Letters*, vol. 113, no. 15, 2014.

[67] G. R. Werner, D. A. Uzdensky, B. Cerutti, K. Nalewajko, and M. C. Begelman, “The extent of power-law energy spectra in collisionless relativistic magnetic reconnection in pair plasmas,” *The Astrophysical Journal*, vol. 816, no. 1, p. L8, 2015.

[68] L. Lehner, C. Palenzuela, S. L. Liebling, C. Thompson, and C. Hanna, “Intense electromagnetic outbursts from collapsing hypermassive neutron stars,” *Physical Review D*, vol. 86, no. 10, 2012.

[69] T. M. Tauris, V. M. Kaspi, R. P. Breton, A. T. Deller, E. F. Keane, M. Kramer, D. R. Lorimer, M. A. McLaughlin, A. Possenti, P. S. Ray, B. W. Stappers, and P. Weltevrede, “Understanding the Neutron Star Population with the SKA,” *Proceedings of Science*, vol. 39, preprint (arXiv: 1501.00005), Dec. 2014, arXiv: 1501.00005.

[70] F. Camilo, S. M. Ransom, J. P. Halpern, J. Reynolds, D. J. Helfand, N. Zimmerman, and J. Sarkissian, “Transient pulsed radio emission from a magnetar,” *Nature*, vol. 442, no. 7105, pp. 892–895, Aug. 2006.

[71] R. F. Archibald, V. M. Kaspi, S. P. Tendulkar, and P. Scholz, “A Magnetar-like Outburst from a High-B Radio Pulsar,” *The Astrophysical Journal Letters*, vol. 829, no. 1, p. L21, 2016.

[72] V. M. Kaspi and M. Kramer, “Radio Pulsars: The Neutron Star Population & Fundamental Physics,” *International Journal of Modern Physics D*, Feb. 2016.

[73] D. Viganò, N. Rea, J. A. Pons, R. Perna, D. N. Aguilera, and J. A. Miralles, “Unifying the observational diversity of isolated neutron stars via magneto-thermal evolution models,” *Mon Not R Astron Soc*, vol. 434, no. 1, pp. 123–141, Sep. 2013.

[74] Y. Levin and M. Lyutikov, “On the dynamics of mechanical failures in magnetized neutron star crusts,” *Monthly Notices of the Royal Astronomical Society*, vol. 427, no. 2, pp. 1574–1579, Dec. 2012.

[75] R. Hollerbach and G. Rüdiger, “The influence of Hall drift on the magnetic fields of neutron stars,” *Monthly Notices of the Royal Astronomical Society*, vol. 337, pp. 216–224, Nov. 2002.

[76] V. C. A. Ferraro, “The non-uniform rotation of the Sun and its magnetic field,” *Monthly Notices of the Royal Astronomical Society*, vol. 97, p. 458, Apr. 1937.

[77] T. S. Wood and R. Hollerbach, “Three Dimensional Simulation of the Magnetic Stress in a Neutron Star Crust,” *Physical Review Letters*, vol. 114, no. 19, p. 191 101, May 2015.

[78] K. N. Gourgouliatos, T. Wood, and R. Hollerbach, “Magnetic field evolution in magnetar crusts through three dimensional simulations,” *Proceedings of the National Academy of Sciences*, vol. 113, no. 15, pp. 3944–3949, Apr. 2016, arXiv: 1604.01399.

[79] J. G. Elfritz, J. A. Pons, N. Rea, K. Glampedakis, and D. Viganò, “Simulated magnetic field expulsion in neutron star cores,” *Monthly Notices of the Royal Astronomical Society*, vol. 456, no. 4, pp. 4461–4474, Mar. 2016, arXiv: 1512.07151.

[80] A. M. Beloborodov, “Untwisting magnetospheres of neutron stars,” *The Astrophysical Journal*, vol. 703, no. 1, pp. 1044–1060, Sep. 2009, arXiv: 0812.4873.

[81] P. Marchant, A. Reisenegger, and T. Akgün, “Revisiting the Flowers-Ruderman instability of magnetic stars,” *Monthly Notices of the Royal Astronomical Society*, vol. 415, pp. 2426–2438, Aug. 2011.

[82] P. Marchant, A. Reisenegger, J. A. Valdivia, and J. H. Hoyos, “Stability of Hall equilibria in neutron star crusts,” *The Astrophysical Journal*, vol. 796, no. 2, p. 94, Nov. 2014, arXiv: 1410.5833.

[83] M. A. Ruderman, “Crystallization and Torsional Oscillations of Superdense Stars,” *Nature*, vol. 218, pp. 1128–1129, Jun. 1968.

[84] P. N. McDermott, H. M. van Horn, and C. J. Hansen, “Nonradial oscillations of neutron stars,” *The Astrophysical Journal*, vol. 325, pp. 725–748, Feb. 1988.

[85] G. Baym, C. Pethick, and D. Pines, “Superfluidity in Neutron Stars,” *Nature*, vol. 224, pp. 673–674, Nov. 1969.

[86] P. S. Shternin, D. G. Yakovlev, C. O. Heinke, W. C. G. Ho, and D. J. Patnaude, “Cooling neutron star in the Cassiopeia A supernova remnant: Evidence for superfluidity in the core,” *Monthly Notices of the Royal Astronomical Society*, vol. 412, pp. L108–L112, Mar. 2011.

[87] D. Page, M. Prakash, J. M. Lattimer, and A. W. Steiner, “Rapid Cooling of the Neutron Star in Cassiopeia A Triggered by Neutron Superfluidity in Dense Matter,” *Physical Review Letters*, vol. 106, no. 8, p. 081 101, Feb. 2011.

[88] J. P. Goedbloed, R. Keppens, and S. Poedts, *Advanced Magnetohydrodynamics: With Applications to Laboratory and Astrophysical Plasmas*. Cambridge: Cambridge University Press, 2010, ISBN: 978-1-139-19556-0.

[89] A. G. Suvorov, A. Mastrano, and U. Geppert, “Gravitational radiation from neutron stars deformed by crustal Hall drift,” *Monthly Notices of the Royal Astronomical Society*, vol. 459, no. 3, pp. 3407–3418, Jul. 2016, arXiv: 1604.04305.

[90] P. B. Jones, “The alignment of the Crab pulsar magnetic axis,” *Astrophysics and Space Science*, vol. 33, pp. 215–230, Mar. 1975.

[91] I. Easson and C. J. Pethick, “Stress tensor of cosmic and laboratory type-II superconductors,” *Phys. Rev. D*, vol. 16, no. 2, pp. 275–280, Jul. 1977.

[92] V. A. Dommes and M. E. Gusakov, “Vortex buoyancy in superfluid and superconducting neutron stars,” *Mon Not R Astron Soc Lett*, vol. 467, no. 1, pp. L115–L119, May 2017.

[93] A. Passamonti, T. Akgün, J. A. Pons, and J. A. Miralles, “The relevance of ambipolar diffusion for neutron star evolution,” *Monthly Notices of the Royal Astronomical Society*, vol. 465, no. 3, pp. 3416–3428, Mar. 2017, arXiv: 1608.00001.

[94] K. Glampedakis, N. Andersson, and L. Samuelsson, “Magnetohydrodynamics of superfluid and superconducting neutron star cores,” *Monthly Notices of the Royal Astronomical Society*, vol. 410, no. 2, pp. 805–829, Jan. 2011, arXiv: 1001.4046.

[95] V. Graber, N. Andersson, K. Glampedakis, and S. K. Lander, “Magnetic field evolution in superconducting neutron stars,” *Monthly Notices of the Royal Astronomical Society*, vol. 453, pp. 671–681, Oct. 2015.

[96] P. Nozières and W. F. Vinen, “The motion of flux lines in type II superconductors,” *Philosophical Magazine*, vol. 14, no. 130, pp. 667–688, Sep. 1966.

[97] R. D. Parks, *Superconductivity: Part 2 (In Two Parts)*. New York, New York: Marcel Dekker, Inc., Apr. 1969, ISBN: 978-0-8247-1521-2.

[98] X. H. Li, Z. F. Gao, X. D. Li, Y. Xu, P. Wang, N. Wang, and J. Yuan, “Numerically Fitting The Electron Fermi Energy and The Electron Fraction in A Neutron Star,” *International Journal of Modern Physics D*, vol. 25, no. 01, p. 1 650 002, Jan. 2016, arXiv: 1603.00224.

[99] E. Gügercinoğlu and M. A. Alpar, “Microscopic vortex velocity in the inner crust and outer core of neutron stars,” *Monthly Notices of the Royal Astronomical Society*, vol. 462, pp. 1453–1460, Oct. 2016.

[100] L. Ferrario and D. Wickramasinghe, “Modelling of isolated radio pulsars and magnetars on the fossil field hypothesis,” *Monthly Notices of the Royal Astronomical Society*, vol. 367, pp. 1323–1328, Apr. 2006.

[101] C. Thompson and R. C. Duncan, “Neutron star dynamos and the origins of pulsar magnetism,” *The Astrophysical Journal*, vol. 408, pp. 194–217, May 1993.

[102] A. Cumming, P. Arras, and E. Zweibel, “Magnetic Field Evolution in Neutron Star Crusts Due to the Hall Effect and Ohmic Decay,” *The Astrophysical Journal*, vol. 609, pp. 999–1017, Jul. 2004.

[103] E. Flowers and M. A. Ruderman, “Evolution of pulsar magnetic fields,” *The Astrophysical Journal*, vol. 215, pp. 302–310, Jul. 1977.

[104] P. B. Jones, “First-principles point-defect calculations for solid neutron star matter,” *Monthly Notices of the Royal Astronomical Society*, vol. 321, pp. 167–175, Feb. 2001.

[105] J. A. Pons, J. A. Miralles, and U. Geppert, “Magneto–thermal evolution of neutron stars,” *Astronomy and Astrophysics*, vol. 496, no. 1, pp. 207–216, Mar. 2009, arXiv: 0812.3018.

[106] A. Tiengo, P. Esposito, S. Mereghetti, R. Turolla, L. Nobili, F. Gastaldello, D. Götz, G. L. Israel, N. Rea, L. Stella, S. Zane, and G. F. Bignami, “A variable absorption feature in the X-ray spectrum of a magnetar,” *Nature*, vol. 500, pp. 312–314, Aug. 2013.

[107] G. A. Rodríguez Castillo, G. L. Israel, A. Tiengo, D. Salvetti, R. Turolla, S. Zane, N. Rea, P. Esposito, S. Mereghetti, R. Perna, L. Stella, J. A. Pons, S. Campana, D. Götz, and S. Motta, “The outburst decay of the low magnetic field magnetar SWIFT J1822.3-1606: Phase-resolved analysis and evidence for a variable cyclotron feature,” *Mon.Not.Roy.Astron.Soc.*, vol. 456, pp. 4145–4155, Mar. 2016.

[108] G. Ashton, P. D. Lasky, V. Graber, and J. Palfreyman, “Rotational evolution of the Vela pulsar during the 2016 glitch,” *NatAs*, Jul. 2019.

[109] P. Weltevrede, S. Johnston, and C. M. Espinoza, “The glitch-induced identity changes of PSR J1119-6127,” *Monthly Notices of the Royal Astronomical Society*, vol. 411, pp. 1917–1934, Mar. 2011.

[110] O. Blaes, R. Blandford, P. Goldreich, and P. Madau, “Neutron starquake models for gamma-ray bursts,” *The Astrophysical Journal*, vol. 343, pp. 839–848, Aug. 1989.

[111] C. Thompson and R. C. Duncan, “The soft gamma repeaters as very strongly magnetized neutron stars - I. Radiative mechanism for outbursts,” *Monthly Notices of the Royal Astronomical Society*, vol. 275, pp. 255–300, Jul. 1995.

[112] A. N. Timokhin, G. S. Bisnovatyi-Kogan, and H. C. Spruit, “Magnetosphere of Oscillating Neutron Star. Nonvacuum Treatment,” *Monthly Notices of the Royal Astronomical Society*, vol. 316, no. 4, pp. 734–748, Aug. 2000.

[113] A. N. Timokhin, “Impact of neutron star oscillations on the accelerating electric field in the polar cap of pulsar: Or could we see oscillations of the neutron star after the glitch in pulsar?” *Ap&SS*, vol. 308, no. 1-4, pp. 345–351, May 2007.

[114] M. I. Large, A. E. Vaughan, and B. Y. Mills, "A Pulsar Supernova Association?" *Nature*, vol. 220, no. 5165, p. 340, Oct. 1968.

[115] A. A. Abdo, "Fermi LAT Observations of the Vela Pulsar," *The Astrophysical Journal*, vol. 696, no. 2, pp. 1084–1093, May 2009.

[116] D. Page, Y. A. Shibanov, and V. E. Zavlin, "Temperature, distance and cooling of the Vela pulsar.," in *Roentgenstrahlung from the Universe*, H. U. Zimmermann, J. Trümper, and H. Yorke, Eds., 1996, pp. 173–174.

[117] K. S. Thorne, "The relativistic equations of stellar structure and evolution," *The Astrophysical Journal*, vol. 212, pp. 825–831, Mar. 1977.

[118] A. Y. Potekhin, W. C. G. Ho, and G. Chabrier, "Atmospheres and radiating surfaces of neutron stars with strong magnetic fields," *arXiv:1605.01281*, May 2016.

[119] E. H. Gudmundsson, C. J. Pethick, and R. I. Epstein, "Structure of neutron star envelopes," *The Astrophysical Journal*, vol. 272, pp. 286–300, Sep. 1983.

[120] A. Y. Potekhin and G. Chabrier, "Equation of state of fully ionized electron-ion plasmas. II. Extension to relativistic densities and to the solid phase," *PhRvE*, vol. 62, no. 6, pp. 8554–8563, Dec. 2000.

[121] F. Douchin and P. Haensel, "A unified equation of state of dense matter and neutron star structure," *A&A*, vol. 380, no. 1, pp. 151–167, Dec. 2001.

[122] F. J. Rogers, F. J. Swenson, and C. A. Iglesias, "OPAL Equation-of-State Tables for Astrophysical Applications," *The Astrophysical Journal*, vol. 456, p. 902, Jan. 1996.

[123] P. Haensel and A. Y. Potekhin, "Analytical representations of unified equations of state of neutron-star matter," *A&A*, vol. 428, no. 1, pp. 191–197, Dec. 2004.

[124] T. Strohmayer, S. Ogata, H. Iyetomi, S. Ichimaru, and H. M. van Horn, "The shear modulus of the neutron star crust and nonradial oscillations of neutron stars," *The Astrophysical Journal*, vol. 375, pp. 679–686, Jul. 1991.

[125] C. J. Horowitz and K. Kadau, "The Breaking Strain of Neutron Star Crust and Gravitational Waves," *PhRvL*, vol. 102, no. 19, p. 191 102, May 2009.

[126] Y. Levin, "QPOs during magnetar flares are not driven by mechanical normal modes of the crust," *Monthly Notices of the Royal Astronomical SocietyL*, vol. 368, no. 1, pp. L35–L38, May 2006.

[127] B. Carter, N. Chamel, and P. Haensel, “Entrainment coefficient and effective mass for conduction neutrons in neutron star crust: II Macroscopic treatment,” *IJMPD*, vol. 15, no. 05, pp. 777–803, May 2006.

[128] M. van Hoven and Y. Levin, “Hydromagnetic waves in a superfluid neutron star with strong vortex pinning,” *Monthly Notices of the Royal Astronomical Society*, vol. 391, no. 1, pp. 283–289, Nov. 2008.

[129] L. Landau and E. Lifshitz, *Theory of Elasticity*. Pergamon Press, 1970.

[130] M. van Hoven and Y. Levin, “Magnetar Oscillations II: Spectral method,” *Monthly Notices of the Royal Astronomical Society*, vol. 420, no. 4, pp. 3035–3046, Mar. 2012.

[131] J. W. S. Rayleigh, *The theory of sound*. Macmillan, 1894.

[132] D. Eichler and R. Shaisultanov, “Dynamical Oscillations and Glitches in Anomalous X-ray Pulsars,” *The Astrophysical Journal Letters*, vol. 715, pp. L142–L145, Jun. 2010.

[133] B. Link and R. I. Epstein, “Thermally Driven Neutron Star Glitches,” *The Astrophysical Journal*, vol. 457, p. 844, Feb. 1996.

[134] T. Sidery and M. A. Alpar, “The Effect of Quantized Magnetic Flux Lines on the Dynamics of Superfluid Neutron Star Cores,” *Monthly Notices of the Royal Astronomical Society*, vol. 400, no. 4, pp. 1859–1867, Dec. 2009.

[135] A. Gruzinov, “Aristotelian Electrodynamics solves the Pulsar: Lower Efficiency of Strong Pulsars,” *arXiv:1303.4094*, Mar. 2013.

[136] I. Contopoulos, D. Kazanas, and C. Fendt, “The Axisymmetric Pulsar Magnetosphere,” *The Astrophysical Journal*, vol. 511, no. 1, pp. 351–358, Jan. 1999.

[137] A. Gruzinov, “Power of an Axisymmetric Pulsar,” *Physical Review Letters*, vol. 94, no. 2, 021101, p. 021 101, Jan. 2005.

[138] K. Parfrey, A. M. Beloborodov, and L. Hui, “Introducing PHAEDRA: A new spectral code for simulations of relativistic magnetospheres,” *Monthly Notices of the Royal Astronomical Society*, vol. 423, no. 2, pp. 1416–1436, Jun. 2012, arXiv: 1110.6669.

[139] A. G. Muslimov and A. I. Tsygan, “General relativistic electric potential drops above pulsar polar caps,” *Mon. Not. R. Astron Soc.*, vol. 255, no. 1, pp. 61–70, Mar. 1992.

[140] A. M. Beloborodov, “Polar-cap accelerator and radio emission from pulsars,” *The Astrophysical Journal*, vol. 683, no. 1, pp. L41–L44, Aug. 2008.

[141] J. Arons, “Pair creation above pulsar polar caps : Geometrical structure and energetics of slot gaps.,” *The Astrophysical Journal*, vol. 266, pp. 215–241, Mar. 1983.

[142] K. S. Cheng, C. Ho, and M. Ruderman, “Energetic Radiation from Rapidly Spinning Pulsars. I. Outer Magnetosphere Gaps,” *The Astrophysical Journal*, vol. 300, p. 500, Jan. 1986.

[143] A. G. Muslimov and A. K. Harding, “High-Altitude Particle Acceleration and Radiation in Pulsar Slot Gaps,” *The Astrophysical Journal*, vol. 606, pp. 1143–1153, May 2004.

[144] M. A. Belyaev and K. Parfrey, “Spatial Distribution of Pair Production over the Pulsar Polar Cap,” *The Astrophysical Journal*, vol. 830, no. 2, p. 119, Oct. 2016.

[145] S. E. Gralla, A. Lupsasca, and A. Philippov, “PULSAR MAGNETOSPHERES: BEYOND THE FLAT SPACETIME DIPOLE,” *The Astrophysical Journal*, vol. 833, no. 2, p. 258, 2016.

[146] F. Cruz, T. Grismayer, A. Y. Chen, A. Spitkovsky, and L. O. Silva, “Coherent emission from QED cascades in pulsar polar caps,” *The Astrophysical Journal Letters*, vol. 919, no. 1, p. L4, Sep. 2021.

[147] J. Arons and J. J. Barnard, “Wave Propagation in Pulsar Magnetospheres: Dispersion Relations and Normal Modes of Plasmas in Superstrong Magnetic Fields,” *The Astrophysical Journal*, vol. 302, p. 120, Mar. 1986.

[148] E. A. Tolman, A. A. Philippov, and A. N. Timokhin, *arXiv:2202.01303*, no. arXiv:2202.01303, Feb. 2022.

[149] A. Philippov, D. A. Uzdensky, A. Spitkovsky, and B. Cerutti, “Pulsar Radio Emission Mechanism: Radio Nanoshots as a Low Frequency Afterglow of Relativistic Magnetic Reconnection,” *The Astrophysical Journal*, vol. 876, no. 1, p. L6, Apr. 2019.

[150] Y. Lyubarsky, “Radio emission of the Crab and Crab-like pulsars,” *Mon. Not. R. Astron Soc.*, vol. 483, no. 2, pp. 1731–1736, Feb. 2019.

[151] V. D. Egorenkov, D. G. Lominadze, and P. G. Mamradze, “Beam instability of the plasma in pulsar magnetospheres,” *Astrophys.*, vol. 19, no. 4, pp. 426–431, Oct. 1983.

[152] M. Z. Rafat, D. B. Melrose, and A. Mastrano, “Wave dispersion in pulsar plasma. part 1. plasma rest frame,” *J. Plasma Phys.*, vol. 85, no. 3, 2019.

[153] A. N. Timokhin and A. K. Harding, “ON THE POLAR CAP CASCADE PAIR MULTIPLICITY OF YOUNG PULSARS,” *The Astrophysical Journal*, vol. 810, no. 2, p. 144, Sep. 2015.

[154] J. Gil, Y. Lyubarsky, and G. I. Melikidze, “Curvature radiation in pulsar magnetospheric plasma,” *The Astrophysical Journal*, vol. 600, no. 2, pp. 872–882, 2004.

[155] H. Falcke and L. Rezzolla, “Fast radio bursts: The last sign of supramassive neutron stars,” *Astron. The Astrophysical Journal*, vol. 562, A137, 2014.

[156] I. Goldman and S. Nussinov, “Weakly interacting massive particles and neutron stars,” *Physical Review D*, vol. 40, no. 10, pp. 3221–3230, Nov. 1989.

[157] W. E. East, L. Lehner, S. L. Liebling, and C. Palenzuela, “Multimessenger signals from black hole-neutron star mergers without significant tidal disruption,” *arXiv:2101.12214*, 2021.

[158] R. H. Price, “Nonspherical perturbations of relativistic gravitational collapse. ii. integer-spin, zero-rest-mass fields,” *Phys. Rev. D*, vol. 5, pp. 2439–2454, 10 1972.

[159] O. Porth, H. Olivares, Y. Mizuno, Z. Younsi, L. Rezzolla, M. Moscibrodzka, H. Falcke, and M. Kramer, “The black hole accretion code,” *Computational Astrophysics and Cosmology*, vol. 4, 1, 2017.

[160] H. Olivares, O. Porth, J. Davelaar, E. R. Most, C. M. Fromm, Y. Mizuno, Z. Younsi, and L. Rezzolla, “Constrained transport and adaptive mesh refinement in the Black Hole Accretion Code,” *Astron. Astrophys.*, vol. 629, A61, A61, 2019.

[161] B. Ripperda, F. Bacchini, O. Porth, E. R. Most, H. Olivares, A. Nathanail, L. Rezzolla, J. Teunissen, and R. Keppens, “General-relativistic Resistive Magnetohydrodynamics with Robust Primitive-variable Recovery for Accretion Disk Simulations,” *Astrophys. J. Suppl. Ser.*, vol. 244, no. 1, 10, p. 10, 2019.

[162] B. Ripperda, F. Bacchini, and A. A. Philippov, “Magnetic reconnection and hot spot formation in black hole accretion disks,” *Astrophys. J.*, vol. 900, no. 2, p. 100, 2020.

[163] B. Ripperda, O. Porth, L. Sironi, and R. Keppens, “Relativistic resistive magnetohydrodynamic reconnection and plasmoid formation in merging flux tubes,” *Monthly Notices of the Royal Astronomical Society*, vol. 485, no. 1, pp. 299–314, 2019.

[164] N. Bessho and A. Bhattacharjee, “Collisionless reconnection in an electron-positron plasma,” *Physical Review Letters*, vol. 95, p. 245 001, 24 2005.

[165] D. A. Uzdensky, N. F. Loureiro, and A. A. Schekochihin, “Fast magnetic reconnection in the plasmoid-dominated regime,” *Physical Review Letters*, vol. 105, no. 23, 2010.

[166] B. Crinquand, B. Cerutti, G. Dubus, K. Parfrey, and A. Philippov, “Synthetic gamma-ray lightcurves of Kerr black-hole magnetospheric activity from particle-in-cell simulations,” *arXiv:2012.09733*, 2020.

[167] A. Tchekhovskoy, R. Narayan, and J. C. McKinney, “Efficient generation of jets from magnetically arrested accretion on a rapidly spinning black hole,” *Monthly Notices of the Royal Astronomical Society Lett.*, vol. 418, no. 1, L79–L83, 2011.

[168] A. Philippov, D. A. Uzdensky, A. Spitkovsky, and B. Cerutti, “Pulsar radio emission mechanism: Radio nanoshots as a low-frequency afterglow of relativistic magnetic reconnection,” *The Astrophysical Journal*, vol. 876, no. 1, p. L6, 2019.

[169] Y. Lyubarsky, “A model for fast extragalactic radio bursts.,” *Monthly Notices of the Royal Astronomical Society*, vol. 442, pp. L9–L13, Jul. 2014.

[170] A. M. Beloborodov, “A flaring magnetar in frb 121102?” *The Astrophysical Journal*, vol. 843, no. 2, p. L26, 2017.

[171] A. M. Beloborodov, “Emission of magnetar bursts and precursors of neutron star mergers,” *arXiv:2011.07310*, Nov. 2020.

[172] L. Comisso and F. A. Asenjo, “Magnetic reconnection as a mechanism for energy extraction from rotating black holes,” *Physical Review D*, vol. 103, no. 2, 2021.

[173] R. Abuter et al. (Gravity Collaboration), “Detection of orbital motions near the last stable circular orbit of the massive black hole SgrA*,” *Astron. Astrophys.*, vol. 618, L10, p. L10, Oct. 2018.

[174] M. Gusakov and V. Dommes, “Relativistic dynamics of superfluid-superconducting mixtures in the presence of topological defects and an electromagnetic field with application to neutron stars,” *Physical Review D*, vol. 94, no. 8, 2016.

[175] M. E. Gusakov, “Force on proton vortices in superfluid neutron stars,” *Monthly Notices of the Royal Astronomical Society*, vol. 485, no. 4, pp. 4936–4950, 2019.

[176] T. E. Riley, A. L. Watts, S. Bogdanov, P. S. Ray, R. M. Ludlam, S. Guillot, Z. Arzoumanian, C. L. Baker, A. V. Bilous, D. Chakrabarty, K. C. Gendreau, A. K. Harding, W. C. G. Ho, J. M. Lattimer, S. M. Morsink, and T. E. Strohmayer, “A NICER view of PSR j0030+0451: Millisecond pulsar parameter estimation,” *The Astrophysical Journal*, vol. 887, no. 1, p. L21, 2019.

[177] J. A. Eilek and T. H. Hankins, “Radio emission physics in the crab pulsar,” *Journal of Plasma Physics*, vol. 82, no. 3, 2016.

[178] B. Ripperda, M. Liska, K. Chatterjee, G. Musoke, A. A. Philippov, S. B. Markoff, A. Tchekhovskoy, and Z. Younsi, “Black hole flares: Ejection of accreted magnetic flux through 3d plasmoid-mediated reconnection,” *The Astrophysical Journal Letters*, vol. 924, no. 2, p. L32, 2022.

[179] A. Galishnikova, A. Philippov, E. Quataert, F. Bacchini, K. Parfrey, and B. Ripperda, "Collisionless accretion onto black holes: Dynamics and flares," *Physical Review Letters*, vol. 130, no. 11, 2023.

[180] M. K. Bowen and R. Smith, "Derivative formulae and errors for non-uniformly spaced points," *Proceedings of the Royal Society of London A: Mathematical, Physical and Engineering Sciences*, vol. 461, no. 2059, pp. 1975–1997, Jul. 2005.

[181] D. A. Uzdensky, "Magnetic reconnection in extreme astrophysical environments," *Space Science Reviews*, vol. 160, no. 1-4, 45–71, 2011.

[182] F. C. Michel, "Rotating Magnetospheres: an Exact 3-D Solution," *The Astrophysical Journal Letters*, vol. 180, p. L133, Mar. 1973.

[183] A. Tchekhovskoy, A. Philippov, and A. Spitkovsky, "Three-dimensional analytical description of magnetized winds from oblique pulsars," *Monthly Notices of the Royal Astronomical Society*, vol. 457, no. 3, pp. 3384–3395, Apr. 2016.

Appendix A: Twist Evolution of the Core

The Hall evolution of B_ϕ in the crust can be written as

$$\frac{\partial B_\phi}{\partial t} = -\nabla_{\rm p} \cdot (B_\phi \boldsymbol{v}_{\rm p}) + (r_\perp \boldsymbol{B}_{\mathbf{p}} \cdot \nabla_{\rm p}) \left(\frac{v_\phi}{r_\perp} \right), \tag{A.1}$$

with $\boldsymbol{v}_p$ and v_ϕ the poloidal and toroidal parts of the Hall drift velocity, and we have defined the poloidal differential operator

$$\nabla_p \equiv \left(\frac{\partial}{\partial r_\perp}, \frac{\partial}{\partial z} \right), \tag{A.2}$$

using cylindrical coordinates $(r_\perp, z)$. The first term on the RHS of (A.1) represents advection of B_ϕ by poloidal velocities, and the second term represents shearing of poloidal field lines in the azimuthal direction. By using a combination of the product rule and the divergence constraint, (A.1) can be written in conservative form as

$$\frac{\partial B_\phi}{\partial t} + \nabla_{\rm p} \cdot \boldsymbol{F}_{\rm hall} = 0, \tag{A.3}$$

where we identify the Hall advection flux

$$\boldsymbol{F}_{\rm hall} = B_\phi \boldsymbol{v}_{\rm p} - v_\phi \boldsymbol{B}_{\rm p}. \tag{A.4}$$

It is convenient to work in the so-called flux-coordinates (Ψ, λ, ϕ), where Ψ labels surfaces of constant poloidal flux, and λ is the length along a given poloidal field line in the $\phi = const$ plane (see eg. [88]). At the base of the crust the boundary condition is $f_\phi = \boldsymbol{j}_{\rm p} \times \boldsymbol{B}_{\rm p}/c = 0$, which implies

$\boldsymbol{v}_\mathrm{p} \parallel \boldsymbol{B}_\mathrm{p}$. So the Hall flux can be written in flux coordinates as

$$\boldsymbol{F}_\mathrm{Hall} = B_\phi |\boldsymbol{v}_\mathrm{p}| \hat{e}_\lambda - v_\phi |\boldsymbol{B}_\mathrm{p}| \hat{e}_\lambda = (B_\phi v_\lambda - v_\phi B_\lambda)\hat{e}_\lambda = F_\lambda \hat{e}_\lambda, \tag{A.5}$$

where $\boldsymbol{B}_\mathrm{p} = B_\lambda \hat{e}_\lambda$, and $\boldsymbol{v}_\mathrm{p} = v_\lambda \hat{e}_\lambda$ at the base of the crust. Then, using the scale factors for flux-coordinates

$$h_\psi = \frac{1}{r_\perp B_\lambda},\ h_\lambda = 1, \tag{A.6}$$

we may write the conservation equation for B_ϕ in flux coordinates as,

$$\frac{\partial B_\phi}{\partial t} = -r_\perp B_\lambda \frac{\partial}{\partial \lambda}\left(\frac{F_\lambda}{r_\perp B_\lambda}\right). \tag{A.7}$$

Rearranging and integrating both sides with respect to λ yields an evolution equation for the twist of the core magnetic field

$$\frac{\partial \zeta(\Psi)}{\partial t} = -[J(\Psi, \lambda_2) - J(\Psi, \lambda_1)], \tag{A.8}$$

where we have identified the twist angle

$$\zeta(\Psi) = \int_{\lambda_1}^{\lambda_2} d\lambda \left(\frac{B_\phi}{r_\perp B_\lambda}\right), \tag{A.9}$$

and the “flux of twist" into/out of the core as

$$J = \frac{F_\lambda}{r_\perp B_\lambda} = \frac{v_\lambda}{r_\perp}\frac{B_\phi}{B_\lambda} - \frac{v_\phi}{r_\perp}. \tag{A.10}$$

Appendix B: Numerical Details of the Code

We evolve the poloidal and toroidal scalar functions on a discrete grid, which is linear in r and $u \equiv \cos\theta$, in the crust and the core. The variable u varies from -1 at the south pole, to 1 at the north pole, and the radius of the star is $r_* = 1$ in units of 10^6cm. The crust core interface is at $r_c = 0.9r_*$. We use the indices i and j to specify grid points in the r and u directions respectively. In most simulations the index j varies from $j_1 = -50$ corresponding to the south pole, to $j_2 = 50$ corresponding to the north pole, with $j = 0$ defining the equator. We choose the difference in u such that $\delta u = 2/(j_2 - j_1)$. The index i varies from $i_0 = 0$ at the centre ($r = 0$), to typical values of $i_c = 400$ at the crust core interface ($r = r_c$) depending on the simulation. Throughout the crust and the last few rows of the core (ghost points for the crust) the radial grid spacing is $\delta r_{\text{crust}} = 1/i_s$. The radial grid spacing in the outer few rows of the core grid matches the radial grid spacing of the crust, for ease of implementing boundary conditions on the crustal field. In order to avoid numerical instabilities near the poles in some simulations, we added adjustable patches of increased resolution in the u direction. Depending on the magnetic field structure, angular resolution was some times set to 3 times the original resolution near the poles in order to obtain convergence. This resolved the issue, and added little expense to the computations.

We evaluate spatial derivatives on the RHS of the crustal evolution equations [Equations (2.10),

Table B.1: The grid resolution used in the crust and core for each of the Models A-E.

Model	Crust ($N_r \times N_u$)	Core ($N_r \times N_u$)
A	(100×133)	(400×133)
B	(100×101)	(400×101)
C	(100×201)	—
D1	(100×101)	(900×101)
D2	(100×101)	(900×101)
D3	(100×101)	(900×101)
E	(500×201)	—

(2.11), (2.25)] with the following finite difference formulae. To evaluate the radial derivatives at each time step in the crust we use

$$\Psi_r = \frac{\Psi_{j,i+1} - \Psi_{j,i-1}}{2\delta r}, \tag{B.1}$$

$$\Psi_{rr} = \frac{\Psi_{j,i-1} - 2\Psi_{j,i} + \Psi_{j,i+1}}{\delta r^2}, \tag{B.2}$$

with the subscript a short hand for partial derivative. For the derivatives with respect to u however, a different approach was needed, since central differences do not preserve second order accuracy on a non-uniform grid. We use the following finite differences which are generalized to maintain second order accuracy (Equations A3b, and A4c in [180]). These are found by using Lagrange interpolation to fit a polynomial to the points, and then taking a derivative of that polynomial. We first define the displacements $\alpha_j = u_j - u$, where u is the point at which we evaluate the derivative, and u_j is a grid point. The point u may be any point contained by the grid points $(j-1, j, j+1)$, not necessarily a grid point. The first and second derivatives with respect to u are then

$$\Psi_u = -\frac{(\alpha_2 + \alpha_3)\Psi_{j-1,i}}{(\alpha_1 - \alpha_2)(\alpha_1 - \alpha_3)} - \frac{(\alpha_1 + \alpha_3)\Psi_{j,i}}{(\alpha_2 - \alpha_1)(\alpha_2 - \alpha_3)} - \frac{(\alpha_1 + \alpha_2)\Psi_{j+1,i}}{(\alpha_3 - \alpha_1)(\alpha_3 - \alpha_2)}, \tag{B.3}$$

$$\begin{aligned}\Psi_{uu} = &- \frac{2(\alpha_2 + \alpha_3 + \alpha_4)\Psi_{j-2,i}}{(\alpha_1 - \alpha_2)(\alpha_1 - \alpha_3)(\alpha_1 - \alpha_4)} - \frac{2(\alpha_1 + \alpha_3 + \alpha_4)\Psi_{j-1,i}}{(\alpha_2 - \alpha_1)(\alpha_2 - \alpha_3)(\alpha_2 - \alpha_4)} \\ &- \frac{2(\alpha_1 + \alpha_2 + \alpha_4)\Psi_{j,i}}{(\alpha_3 - \alpha_1)(\alpha_3 - \alpha_2)(\alpha_3 - \alpha_4)} - \frac{2(\alpha_1 + \alpha_2 + \alpha_3)\Psi_{j+1,i}}{(\alpha_4 - \alpha_1)(\alpha_4 - \alpha_2)(\alpha_4 - \alpha_3)}.\end{aligned} \tag{B.4}$$

We use the same derivative formula for the toroidal scalar function I.

For evolution equations in the core (Equations (2.40), (2.52), (2.61)) we use the difference Equations (B.3) and (B.4) for derivatives in the u direction. We also require specialized formula for radial derivatives in the core, because the radial grid spacing changes in the outer few rows of the core grid. We use formula the same as those above (Equations (B.3) and (B.4)), but with differences in the radial direction ($u \longrightarrow r$, $j \longrightarrow i$).

We use a variable time step, which shrinks in order to avoid instability in the evolution. Because we are evolving magnetic fields and crustal displacements with a variety of evolution equations, we calculate a stable time step for each evolution equation. For the Hall effect [Equations (2.10) and (2.11)], we use the fastest electron velocity in the grid to limit the maximum time step, using

$$\delta t_{\mathrm{hall}} = k_c \frac{4\pi n_e e}{c} \frac{\delta r \delta \mu}{|\nabla \times \boldsymbol{B}_{\mathrm{T}}|}, \tag{B.5}$$

with k_c a Courant parameter. For Ohmic diffusion [RHS of Equations (2.10) and (2.11)], we use

$$\delta t_{\mathrm{ohm}} = k_c \frac{\delta r^2}{\eta} = k_c \frac{4\pi\sigma \delta r^2}{c}, \tag{B.6}$$

which is minimized by choosing the smallest conductivity. For the elastic relaxation [Equation (2.25)] we use the time step

$$\delta t_{\mathrm{el}} = k_c \gamma \frac{\delta r^2}{v_{\mathrm{sh}}^2}. \tag{B.7}$$

For the hydromagnetic relaxation Equation (2.40) we choose the diffusion time step

$$\delta t_{\mathrm{hme}} = k_c \frac{\delta r^2}{k}. \tag{B.8}$$

The stable time step for Jones drift [Equation (2.52)] is chosen using the maximum flux tube velocity on the computational grid,

$$\delta t_{\mathrm{Jones}} = k_c \frac{\delta r \delta \mu}{\max|\boldsymbol{v}_{\mathrm{J}}|}, \tag{B.9}$$

and similarly with the spin-down transport of flux [Equation (2.61)]

$$\delta t_{\mathrm{sd}} = k_c \frac{\delta r \delta \mu}{\max|\boldsymbol{v}_{\mathrm{sd}}|}. \tag{B.10}$$

In all of the above, the Courant parameter $0 < k_c < 1$ is chosen so that such that we observe convergence and stability. At each time step, we evaluate the RHS of the evolution equations using the difference formulae above, then use Euler integration with the smallest time step

$$\delta t = \min\{dt_{\mathrm{hall}}, \delta t_{\mathrm{ohm}}, \delta t_{\mathrm{el}}, \delta t_{\mathrm{hme}}, \delta t_{\mathrm{Jones}}, \delta t_{\mathrm{sd}}\}, \tag{B.11}$$

to advance the functions Ψ and I to $t + \delta t$. In the code we normalize the Hall Evolution equation in the same way as [24],

$$1.6 \times 10^6 \frac{\partial \boldsymbol{B}_{14}}{\partial t_{\rm yr}} = -\tilde{\nabla} \times \left(\frac{\tilde{\nabla} \times \boldsymbol{B}_{14}}{n_{e,0}} \times \boldsymbol{B}_{14} \right) - 0.02 \tilde{\nabla} \times \left(\frac{\tilde{\nabla} \times \boldsymbol{B}_{14}}{\sigma_0} \right), \tag{B.12}$$

where $\boldsymbol{B}_{14} = \boldsymbol{B}/10^{14}$ G, $t_{\rm yr} = t/3.15 \times 10^7$ s, $\tilde{\nabla}$ is the del operator with lengths normalized to 10^6 cm, $n_{e,0} = n_e/2.5 \times 10^{34}$ cm^{-3}, and $\sigma_0 = \sigma/1.8 \times 10^{23}$ s^{-1}. In Model A we choose the relaxation parameter $k = 2 \times 10^{-6}$ cm s^{-1} In Model E we choose the parameter $\gamma = 1 \times 10^{16}$ s^{-1}.

In the core we treat coordinate singularities along the pole, and at the origin by freezing in the magnetic field beyond some flux surface Ψ_0, so that the magnetic field is unevolving very close to the pole. This is done by multiplying the velocity fields in Equations (2.40) (2.52) and (2.61) by the function

$$s(\Psi) = \frac{1}{\exp[-a(\Psi - \Psi_0)] + 1}, \tag{B.13}$$

which behaves like a smoothed step function. The parameter a is chosen to make the step as steep as possible while still being resolved by the grid mesh. In Model A we also add a term to the RHS of Equation (2.40),

$$-\frac{1}{\tau} \frac{I(r,\theta)}{\exp[b(\Psi - \Psi_0)] + 1}, \tag{B.14}$$

to ensure that any toroidal field beyond Ψ_0 is exponentially reduced on the timescale τ. Our results are not sensitive to these methods, so long as Ψ_0 is close to the pole.

We have tested the Ohmic evolution of our code by comparing with the analytic Ohmic eigenmodes, and observe excellent agreement. We also study the agreement of our code with the grid based code of [24], (data files provided by the authors). We compare the Hall-Ohmic evolution of 3 initial fields–the so-called “Hall Equilibrium", “Ohmic Eigenmode", and “Barotropic MHD Equilibrium", shown in Figure 2 of [24]. Excellent agreement was observed in all cases. We have also carried out resolution studies of all simulations presented in Section 3.6, and summarize the grid sizes for which each simulation had converged in Table B.1.

Appendix C: Elastic Modes

The elastic modes $\zeta_{nl}(r)$ and corresponding frequencies ω_{nl} are found by solving the eigenvalue equation [Equation (3.64)],

$$-\omega_{nl}^2\rho\zeta_{nl} = \frac{d\tilde{\mu}}{dr}\left(\frac{d\zeta_{nl}}{dr} - \frac{\zeta_{nl}}{r}\right) + \frac{\tilde{\mu}}{r^2}\frac{d}{dr}\left(r^2\frac{d\zeta_{nl}}{dr}\right) - [l(l+1)\mu + 2\mu_B]\frac{\zeta_{nl}}{r^2}. \tag{C.1}$$

Following [84] Equation (3.64) is reduced to two first-order ordinary diffrential equations by introducing the dimensionless variables

$$S_1 \equiv \frac{\zeta_{nl}}{r}, \tag{C.2}$$

$$S_2 \equiv \frac{\tilde{\mu}r_\star}{\omega^2 M_\star}\left(\frac{d\zeta_{nl}}{dr} - \frac{\zeta_{nl}}{r}\right), \tag{C.3}$$

where S_1 refers to a dimensionless amplitude, and S_2 is a dimensionless stress. In terms of these variables, the equation for ζ_{nl} becomes

$$r\frac{dS_1}{dr} = \frac{\omega^2}{\tilde{\mu}}\frac{M_\star}{r_\star}S_2, \tag{C.4}$$

$$r\frac{dS_2}{dr} = \frac{\mu r_\star}{\omega^2 M_\star}\left[l(l+1) - 2 - \frac{\omega^2\rho r^2}{\mu}\right]S_1 - 3S_2. \tag{C.5}$$

In the limit $\mu_B \longrightarrow 0$ Equations (C.4) and (C.5) reduce to Equations 25(a) and (b) of [84]. The appropriate boundary conditions for these unforced modes are zero magnetic stress $\sigma_{r\theta}^{\text{mag}} = \sigma_{r\phi}^{\text{mag}} = 0$ and zero elastic stress $\sigma_{r\theta}^{\text{el}} = \sigma_{r\phi}^{\text{el}} = 0$ at the boundaries. These conditions are expressed through the single equation

$$\tilde{\mu}\left(\frac{d\zeta_{nl}}{dr} - \frac{\zeta_{nl}}{r}\right) = 0, \tag{C.6}$$

or in terms of the variable S_2,

$$S_2(r_i) = 0, \tag{C.7}$$

where r_i is either the radius of the crust-core interface (r_c), or the surface of the crust ($r_\star$). The amplitude of the displacement is arbitrary, as the problem is linear. We set the amplitude at the crust-core interface

$$S_1(r_c) = 1. \tag{C.8}$$

Equations (C.4) and (C.5), together with the boundary conditions Equations (C.7) and (C.8), constitute a well posed Sturm-Liouville problem.

The Sturm-Lioville problem is solved by ‘shooting’ (integrating) from the crust-core interface and varying the eigenvalue until the boundary condition Equation (C.7) is satisfied at the surface of the crust. We have implemented a fourth-order Runge-Kutta integrator, and used it in two modes: i) Scanning: for each value of l the eigenvalue is varied coarsely through all possible values up to some maximum frequency. The frequencies for which $S_2(r_\star)$ is minimized are recorded as estimates of the eigenvalues, together with the corresponding value of n. ii) Root finding: for each (n, l) Newton-Raphson method is used to converge on the eigenvalue ω_{nl} for which $|S_2(r_\star)| < \epsilon_\star$ (typically we set $\epsilon_\star = 10^{-12}$). The frequencies from the scanning mode are used as first guesses for the Newton-Raphson iterations.

When finding modes we use a uniform radial grid of $50,000$ points. As a test we check the orthogonality of our modes. We typically find

$$\int_{r_c}^{r_\star} \rho r^2 \zeta_{nl} \zeta_{n'l} dr = \delta_{nn'} \pm 10^{-9}. \tag{C.9}$$

We also studied the time-dependent propagation of a radial $l = 0$ wave using our elastic modes. This was compared to the same wave propagation using a 1D finite difference solver. The two methods produced the same time-dependent solution. To test the convergence, we found one set of modes on a grid of $20,000$ points, and another on a grid of $50,000$ points. We ran simulations of 2D axisymmetric elastic waves with both sets of modes, using the same initial conditions. The time-dependent solutions were indistinguishable, indicating that our elastic modes and frequencies are converged to a sufficient accuracy for our dynamical simulations. The obtained normalized modes ζ_{nl} and their frequencies ω_{nl} are stored and used for the dynamical simulations described below.

Appendix D: Crust Dynamics: Numerical Method

The spectral method follows the dynamics of the crust through the coefficients $a_{nlm}(t)$. Since we are only considering axisymmetric dynamics in this work, the index m is set to zero, and ξ_ϕ is the only nonzero component of the displacement. The displacement is written as a sum over basis functions (orthogonal eigenmodes),

$$\boldsymbol{\xi}(t,r,\theta) = \xi_\phi(t,r,\theta)\hat{\boldsymbol{\phi}} = \sum_{n=0}^{n_{\max}} \sum_{l=1}^{l_{\max}} a_{nl}(t)\boldsymbol{\xi}_{nl}(r,\theta), \tag{D.1}$$

where finite $n_{\max}$ and $l_{\max}$ are chosen to truncate the infinite series. The product $n_{\max} \times l_{\max}$ is the total number of the eigenmodes in our simulations. The basis functions are

$$\boldsymbol{\xi}_{nl} = \xi^{\phi}_{nl}\hat{\boldsymbol{\phi}} = \zeta_{nl}(r)\frac{dY_{l0}(\theta)}{d\theta}\hat{\boldsymbol{\phi}}, \tag{D.2}$$

where $Y_{l0} = P_l(\cos\theta)$ are the Legendre polynomials and the radial eigenfunctions $\zeta_{nl}(r)$ are found as described in Appendix C. The initial conditions are set by projecting $\boldsymbol{\xi}(t = 0)$ on to the basis functions $\boldsymbol{\xi}_{nl}$ for each (n,l),

$$a_{nl}(t=0) = \langle \boldsymbol{\xi}(\boldsymbol{r}, t=0), \boldsymbol{\xi}_{nl} \rangle = \int_{r_c}^{r_\star} dr \int_0^{\pi} d\theta\, r^2 \sin\theta\, \rho\, \xi_\phi(t=0)\, \xi^{\phi}_{nl}, \tag{D.3}$$

where we have used that the modes are orthonormal. The integration is done numerically on a uniform (r,θ) grid of $N_r \times N_\theta = 1000 \times 600$ points using the fifth-order accurate Simpsons rule. The Legendre polynomials P_l and derivatives are computed once at the beginning of the simulation and stored. The time evolution of a_{nl} is given by the equation of motion

$$\ddot{a}_{nl}(t) + \omega^2_{nl}a_{nl}(t) = \langle \boldsymbol{f}_{\rm ext}(\boldsymbol{r},t), \boldsymbol{\xi}_{nl} \rangle, \tag{D.4}$$

where $\boldsymbol{f}_{\rm ext} = \boldsymbol{f}_{\rm core} + \boldsymbol{f}_{\rm mag}$ is the force on the crust due to the core and magnetosphere, and $\langle \boldsymbol{f}_{\rm ext}(\boldsymbol{r}, t), \boldsymbol{\xi}_{nl} \rangle$ is a matrix containing the projection of $\boldsymbol{f}_{\rm ext}$ onto the basis functions. The force of the core on the crust (Equation (3.68)) is written as

$$\boldsymbol{f}_{\rm core} = -v_A \frac{\rho_<}{\rho_>} \delta(r - r_c) \dot{\boldsymbol{\xi}} = -v_A \frac{\rho_<}{\rho_>} \delta(r - r_c) \sum_{n=0}^{n_{\rm max}} \sum_{l=1}^{l_{\rm max}} \dot{a}_{nl}(t) \boldsymbol{\xi}_{nl}, \tag{D.5}$$

where we have used Equation (D.1) to express the $\dot{\boldsymbol{\xi}}$ in terms of the coefficients $\dot{a}_{nl}$. Then the projection of $\boldsymbol{f}_{\rm core}$ onto the basis functions is given by

$$\langle \boldsymbol{f}_{\rm core}(\boldsymbol{r}, t), \boldsymbol{\xi}_{nl} \rangle = \sum_{n'=0}^{n_{\rm max}} \sum_{l'=1}^{l_{\rm max}} \dot{a}_{n'l'}(t) C_{n'l'nl}, \tag{D.6}$$

where

$$C_{n'l'nl} = -\int_{r_c}^{r_\star} dr \int_0^\pi d\theta r^2 \sin\theta \rho v_A \frac{\rho_<}{\rho_>} \delta(r - r_c) \xi^\phi_{n'l'} \xi^\phi_{nl} = -r_c^2 v_A \rho_< f_{n'l'}(r_c) f_{nl}(r_c) \delta_{ll'}. \tag{D.7}$$

The components of the coupling matrix $C_{n'l'nl} = 0$ for $l' \neq l$; therefore, it is not necessary to sum over l' in Equation (D.6). The matrix $C_{n'l'nl}$ is calculated once at the beginning of each simulation and stored.

The force of the magnetosphere on the crust is

$$f^\phi_{\rm mag} = \frac{\rho_B}{\rho_{\rm crys}} c^2 \cos\alpha\, \delta(r - r_\star)\, r_\perp \frac{\partial}{\partial \chi} \left(\frac{\xi_\phi}{r_\perp} \right) \Bigg|_{r_>}. \tag{D.8}$$

As ξ_ϕ is evolved self-consistently in the magnetosphere (Appendix E), the force $f^\phi_{\rm mag}$ is calculated at each time step and used to evaluate

$$\begin{aligned} \langle \boldsymbol{f}_{\rm mag}(\boldsymbol{r}, t), \boldsymbol{\xi}_{nl} \rangle &= \int_{r_c}^{r_\star} dr \int_0^\pi d\theta r^2 \sin\theta\, \rho\, f^\phi_{\rm mag}(t, r, \theta)\, \xi^\phi_{nl} \\ &= r_\star^2 \rho(r_\star) \zeta_{nl}(r_\star) \int_0^\pi d\theta \sin\theta f^\phi_{\rm mag}(t, r_\star, \theta) \frac{\partial Y_{l0}}{\partial \theta}, \end{aligned} \tag{D.9}$$

where the integral is evaluated numerically at each time step on a uniform grid of N_θ points using the fifth-order Simpsons rule. Equation (D.4) is integrated in time together with using the fourth-order Runge-Kutta integration, with a constant time step $\Delta t = \min\{\Delta t_{\mathrm{crust}}, \Delta t_{\mathrm{mag}}\}$, where $\Delta t_{\mathrm{crust}}$ is the largest stable time step for the crust, and Δt_{core} is the largest stable time step for the magnetosphere (see Appendix E). We use $\Delta t_{\mathrm{crust}} = k_c/\max\{\omega_{nl}\}$ with $k_c \leq 0.1$, where $\max\{\omega_{nl}\}$ is the highest frequency of all of the modes we are using. We have found that for a free crust (without external forcing terms), our code conserves energy to one part per million. If the external forcing terms are included, some additional error is introduced, and energy is usually conserved to one part in 10^5.

We use $(n_{\mathrm{max}}, l_{\mathrm{max}}) = (300, 200)$, a total of 60,000 modes. More radial modes are needed ($n_{\mathrm{max}} > l_{\mathrm{max}}$) to properly resolve the wave transmission through the upper layers of the crust where the scale height is very small. The only relevant scale in the θ-direction is introduced by the initial conditions. We have tried independently increasing n_{max} to 600, and l_{max} to 400, and we observe the same results.

Appendix E: Magnetosphere Dynamics: Numerical Method

In the magnetosphere, we calculate the small azimuthal displacement ξ_ϕ, using the so-called magnetic flux coordinates (ψ, χ, ϕ), where ψ =const defines surfaces of constant poloidal flux, and χ is the length along poloidal the field lines in the ϕ = const plane. The dependence of the Cartesian position vector $\boldsymbol{x}$ on the coordinates ψ and χ is found by integrating the equation

$$\frac{d\boldsymbol{x}(\psi, \chi)}{d\chi} = \frac{\boldsymbol{B}}{|\boldsymbol{B}|}. \tag{E.1}$$

The footpoints of the field lines are chosen to coincide with the grid points used in the projection Equation (D.9). We chose the grid spacing along the field lines so that the light-crossing time of each grid cell is the same. When we include the liquid ocean, the grid spacing remains large in the magnetosphere, but becomes very small in the ocean where the density increases. By using this grid spacing, we are not limited to a prohibitively small time step by the Courant condition. The time evolution of $\xi_\phi(\psi, \chi)$ is given by the wave equation

$$\frac{\partial^2 \xi_\phi(\psi, \chi)}{\partial t^2} = \frac{B}{4\pi r_\perp \rho_B} \frac{\partial}{\partial \chi} \left[r_\perp^2 B \frac{\partial}{\partial \chi} \left(\frac{\xi_\phi(\psi, \chi)}{r_\perp} \right) \right]. \tag{E.2}$$

We are effectively solving a 1D wave equation for each flux surface ψ. The right-hand side of Equation (E.2) is evaluated using the second-order finite difference formulas given by [180]. The first derivatives use a three-point stencil, and the second derivatives use a four-point stencil, so that second-order accuracy is preserved when the grid spacing is nonuniform. We integrate Equation (E.2) in time, together with Equation (D.4) for the crust using the fourth-order Runge-Kutta integration.

The crust provides the boundary condition for $\xi_\phi(\psi, \chi)$ at the surface in the magnetosphere, and the magnetosphere communicates to the crust through the force Equation (D.8). The stable time step for the magnetosphere is $\Delta t_{\rm mag} = k_c dt_\chi$, where dt_χ is the light-crossing time of a grid cell, and $k_c < 0.5$. We set the time step for the simulation $\Delta t = \min\{\Delta t_{\rm crust}, \Delta t_{\rm mag}\}$, where $\Delta t_{\rm crust}$ is the largest stable time step for the crust (see Appendix D). We find that $\sim$ 600 grid points are required for the projection Equation (D.9), which results in $\sim$ 50 open flux surfaces ($\sim$ 25 at each pole), and $\sim$ 275 closed flux surfaces.

Appendix F: A Test for Wave Transmission

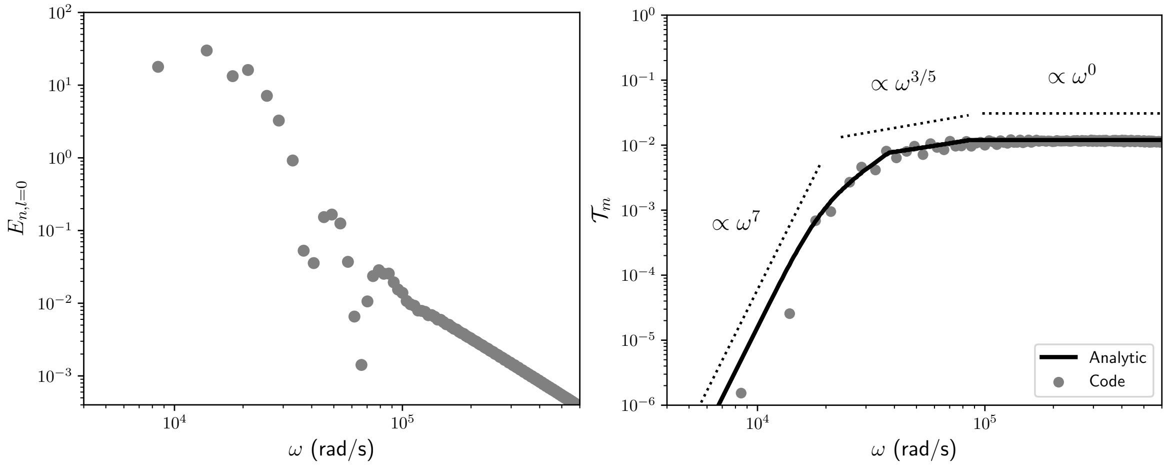

Figure F.1: Left: initial energy spectrum of waves in this test problem. Right: transmission coefficient of waves into the magnetosphere $\mathcal{T}_m(\omega)$. The thick black line shows the transmission coefficient found by solving the analytic reflection conditions (Section 3.3), and the gray dots show the numerical transmission coefficient measured using our code for an $l = 0$ radial wave. The dotted lines show the powe-law scalings in each frequency range.

In order to test the implementation of the crust-magnetosphere coupling in our numerical model, we have measured the frequency-dependent transmission coefficient $\mathcal{T}_m(\omega)$ using our code. We initialize the simulation by launching a purely radial $l = 0$ wave in the crust. The magnetosphere is chosen to be a radial monopole with outflow boundary conditions on *all* flux surfaces, so that no Alfvén waves return to the crust. The setup is effectively 1D, so that we should recover the transmission coefficient calculated in Section 3.3 for a Cartesian slab crust.

The energy spectrum of the initial condition is shown in Figure F.1 (left panel). The initial displacement is a smoothed step function, similar to the 2D initial conditions used in Section 3.6. It corresponds to a strain layer of thickness $\Delta\ell \sim 10^4$ cm, similar to the pressure scale height in the deep crust. The energy spectrum peaks around $\omega \sim \tilde{v}_s/\ell_0 \sim 2 \times 10^4$ rad/s.

We measure the transmission coefficient by calculating the exponential decay time of the energy in each mode τ_m. The transmission coefficient for a given elastic mode is then calculated as $\mathcal{T}_m = 2\tau/\tau_m$, where $\tau \approx 1$ ms is the elastic wave crossing time of the crust. This gives the effective transmission coefficient as a function of the mode frequency, $\mathcal{T}_m(\omega)$, which we compare with the analytically calculated $\mathcal{T}_m$ (Figure F.1). The two lowest-frequency modes deviate from the analytical result, because they are reflected deep in the crust near neutron drip, where the exact density profile used in the code deviates from the approximation $\rho \propto |z|^3$ used in the analytical model. There are few data points at low frequencies in Figure F.1 because there are few elastic modes in that frequency range. We performed similar simulations with different initial conditions and found nearly the same $\mathcal{T}_m(\omega)$.

Appendix G: Dispersion Relation and Normal Modes of Pulsar Plasma

Here we review the dispersion relation and normal modes of the electron-positron ($e^{\pm}$) pair plasma expected to exist in pulsar magnetospheres. The electron Larmor radius near the pulsar is much smaller than the wavelength of the normal modes we are considering, so the plasma is very highly magnetized. The ultra-strong magnetic field ensures that gyration of $e^{\pm}$ decays very quickly due to synchrotron cooling. Therefore, charged particles effectively only move parallel to the magnetic field lines, and the plasma supports a very limited set of normal modes. The dispersion relation is obtained from the Vlasov-Maxwell equations [147],

$$(\omega^2 - c^2k^2)\left[(\omega^2 - c^2k_{||}^2)\left(1 - \frac{\omega_p^2}{\omega^2}g\right) - c^2k_{\perp}^2\right] = 0, \tag{G.1}$$

where ω is the wave frequency, ω_p the plasma frequency, $k_{||}$ and $k_{\perp}$ are the components of the wave-vector parallel and perpendicular to $\boldsymbol{B}$, $g = \langle\gamma^{-3}\,(1 - kv/\omega)^{-2}\rangle$, and $\langle ... \rangle$ indicates an average over particle momenta. If the plasma is cold, $g = 1$ in the plasma rest frame. The dispersion relation describes three modes: The extraordinary (X) mode with $\omega = ck$ and electric field polarized in the $\boldsymbol{k} \times \boldsymbol{B}$ direction, and two modes on the ordinary (O) branch with electric field polarized in the $\boldsymbol{k} - \boldsymbol{B}$ plane. Specifically, the polarization of the O-modes is given by

$$\frac{\delta E_{||}}{\delta E_{\perp}} \approx \begin{cases} -\dfrac{c^2k_{||}k_{\perp}}{\omega_p^2} & \text{(subluminal Alfvén mode)} \\ \dfrac{\omega_p^2}{c^2k_{||}k_{\perp}} & \text{(superluminal mode),} \end{cases} \tag{G.2}$$

where $\delta E_{||}$ is the wave electric field parallel to $\boldsymbol{B}$, and $\delta E_{\perp}$ is the wave electric field perpendicular to $\boldsymbol{B}$ in the $\boldsymbol{k} - \boldsymbol{B}$ plane [147]. The Alfvén mode has phase speed $\omega/k < c$, while the superluminal mode has $\omega/k > c$. For a given $\boldsymbol{k}$, the three modes (extraordinary, Alfvén, and superluminal) are orthogonal.

Appendix H: Beam Instability in Pulsar Plasma

Here we review the relativistic beam instability in highly magnetized $e^\pm$ plasma (for a detailed calculation see [151]). Consider a uniform background of $e^\pm$ with uniform density n_p which streams relativistically along the magnetic field with Lorentz factor γ. The beam has uniform density $n_b < n_p$, and a gaussian distribution of momentum parallel to the magnetic field with mean $p_b = \gamma_b mc$, and width $\Delta p_b = \Delta\gamma_b mc$. If the beam density is sufficiently high the instability operates in the hydrodynamic regime $\Gamma\gamma_b^3/(kc\Delta\gamma_b) \gg 1$, where Γ is the growth rate. If the background plasma is cold the dispersion relation of purely longitudinal oscillations in the pulsar frame has the form (Eq. G.1)

$$1 - \frac{\omega_p^2}{\omega^2}g - \frac{\omega_b^2}{\omega^2}\frac{1}{\gamma_b^3(1 - kv_b/\omega)^2} = 0, \tag{H.1}$$

where the third term is due to the beam with $\omega_b = \sqrt{4\pi n_b e^2/m}$, and $v_b = c(1 + 1/\gamma_b^2)^{-1/2}$ [151]. Near Cherenkov resonance, the dispersion relation can be written in the form $\omega = kv_b + \Delta\omega$, with $|\Delta\omega| \ll kv_b$. The growth rate is maximal when k approaches $k_0 \equiv 2\omega_p\langle\gamma\rangle^{1/2}/c$, and is given by

$$\Gamma = \mathrm{Im}\,\Delta\omega = \frac{\sqrt{3}}{4\cdot 2^{1/3}}\left(\frac{n_b}{n_p}\right)^{1/3}\frac{ck_0}{\gamma_b\langle\gamma^3\rangle^{1/3}}. \tag{H.2}$$

The condition for the instability to operate in the hydrodynamic regime is then

$$\left(\frac{n_b}{n_p}\right)^{1/3} \gg \frac{\langle\gamma\rangle\Delta\gamma_b}{\gamma_b^2}. \tag{H.3}$$

The instability can grow at the maximal rate (Eq. H.2) even when the momentum spread of the beam is large $\Delta\gamma_b \gtrsim \gamma_b$, as long as $\gamma_b \gg \langle\gamma\rangle$, such that Eq. H.3 is satisfied. Note that when $k \ll k_0$ instability still occurs, but at a slower rate than Eq. H.2 [151]. Note also that the beam instability directly couples to the Alfvén mode (the superluminal mode has $\omega/k > c$ so it cannot achieve Cherenkov resonance, and the X-mode does not couple to the plasma).

Appendix I: Instability Growth Rate

Beam instabilities in pulsar magnetospheres are usually discussed in the context of primary accelerated $e^\pm$ with $\gamma_b \sim 10^6$ (beam) interacting with the secondary $e^\pm$ with $\gamma \sim 10^2$ (plasma) [44]. The growth rate (Eq. H.2) is then strongly suppressed by the ultra-high Lorentz factor of the primary accelerated particles, and the instability cannot develop before the plasma leaves the magnetosphere $\Gamma/\Omega \ll 1$, where Ω is the rotation frequency of the pulsar. However, in this work we have showed that non-local gamma-ray emission in the outer magnetosphere can inject $e^\pm$ with a different momentum than the wind. In this case, both streams are made of secondary $e^\pm$, so the growth rate is not suppressed by the ultra-high Lorentz factors typical of the primary accelerated particles. Here we estimate the growth rate Γ/Ω for such a scenario in the outer magnetosphere of an energetic pulsar.

We assume that the bulk of the $e^\pm$ wind in the outer magnetosphere is supplied by the discharge near the pulsar polar cap. For a conservative estimate, we set the multiplicity near the light-cylinder $\mathcal{M} \sim 10^3$ and the typical Lorentz factor $\gamma \sim 10^2$. We assume that the beam particles (created by photon collisions) have $\gamma_b \sim 10^3$. The growth rate (Eq. H.2) near the light-cylinder radius $r_{\rm LC} = c/\Omega$ is then in order of magnitude

$$\frac{\Gamma}{\Omega} \sim \left(\frac{n_b}{n_p}\right)^{1/3} \frac{\omega_p}{\Omega \gamma_b \gamma^{1/2}} \sim 10^3 \left(\frac{\gamma_b}{10^3}\right)^{-1} \left(\frac{\gamma}{10^2}\right)^{-1/2} \left(\frac{P}{0.033\ \rm s}\right)^{1/2} \left(\frac{B_{\rm LC}}{10^6\ \rm G}\right)^{1/2} \left(\frac{\mathcal{M}}{10^2}\right)^{1/2}, \tag{I.1}$$

where $\omega_p = \sqrt{4\pi \mathcal{M} n_{\rm GJ} e^2/m}$, $P = 2\pi/\Omega$, $B_{\rm LC}$ is the magnetic field strength at the light-cylinder, and we set $n_b/n_p \sim 0.1$. Since $\Gamma/\Omega \gg 1$, the instability can easily develop (a larger $\mathcal{M}$ further increases Γ/Ω). The instability could produce radio emission in the outer magnetosphere which is different to the usual polar-cap emission. It requires powerful gamma-ray emission and $e^\pm$ production from the current-sheet. Therefore, it is most relevant for pulsars like Crab, which have high-B_{LC}. Note that for extremely energetic pulsars the $e^{\pm}$ created by the current sheet could have multiplicity larger than the wind. The role of the beam and the plasma would then be reversed.

Appendix J: Numerical Convergence

Figure J.1 shows time evolution of the magnetic flux on the event horizon vs time at different grid resolutions. In GRPIC the simulations are well converged at all scale separations for the resolution 2880 × 2160. In GRRMHD the axisymmetric simulation is well converged, resolving the current layer by approximately 10 cells over its width for $\eta = 10^{-5}$ at a resolution 6144×3072.

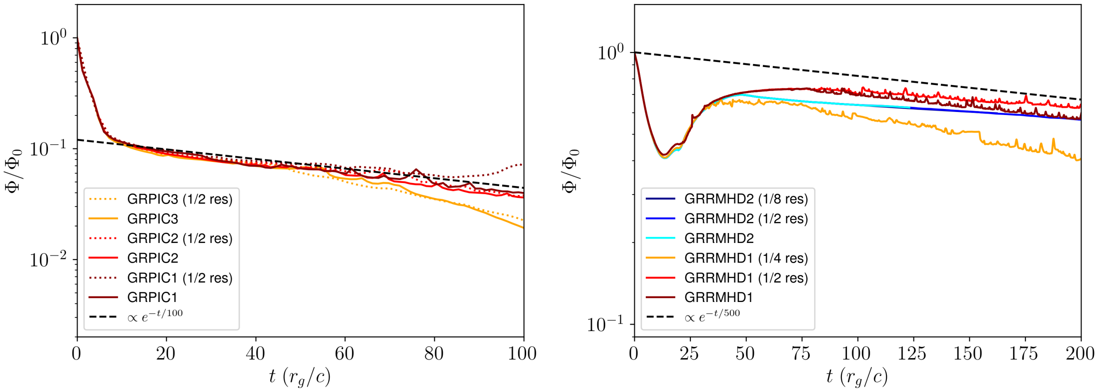

Figure J.1: Convergence study for each simulation. Left: Flux on the event horizon vs time at 2 resolutions for each of the simulations GRPIC1, GRPIC2, and GRPIC3. Right: Flux on the event horizon vs time at 3 resolutions for simulation GRRMHD1 and GRRMHD2.

We confirm that the current sheet is resolved in Figure J.2, showing the AMR blocks for simulation GRRMHD1 (each block contains $N_r \times N_\theta = 16 \times 8$ cells). The reconnection rate and the thinning of the sheet in GRRMHD is converged when there are at least 10 grid cells over the width of the current sheet once it finished the thinning process [162]. In the simulation GRRMHD1 the current sheet width is resolved by slightly more than one AMR block inside the ergosphere, indicating that GRRMHD1 is converged (Figure J.1, right panel dark red curve), while GRRMHD1 at 1/2 resolution and 1/4 resolution are not converged (Figure J.1, right panel red and yellow curves), yet still resolve the current sheet by more than one cell.

The combination of an implicit-explicit (IMEX) time-stepping scheme to capture fast recon-

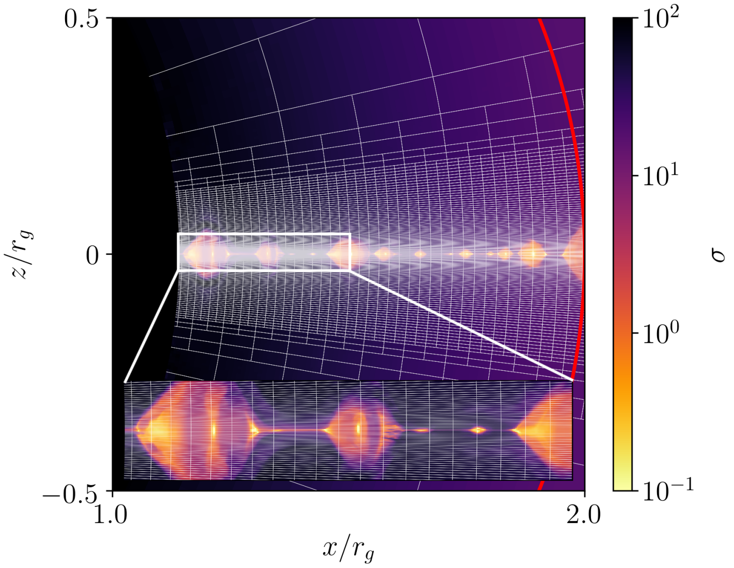

Figure J.2: AMR blocks used in the simulation GRRMHD1, with inset zoomed on the current sheet near the event horizon. Color shows magnetization $\sigma = B^2/(4\pi\rho c^2)$, and the red curve shows the ergosphere boundary.

nection dynamics [161], together with adaptive mesh refinement (AMR) capabilities of `BHAC` to accurately resolve the smallest scales in the system allows us to study resistive reconnection and plasmoid formation in the GRRMHD simulations [162]. For the GRPIC simulations a grid uniform in $\cos\theta$ helps to concentrate resolution on the equatorial current sheet and ensure the plasmoid formation is resolved.

The flux decay time scale converges in the GRPIC simulations with increasing r_H/r_L. The small-r_L model (GRPIC1) displays a full spectrum of plasmoid size, while small plasmoids are not present in the large-r_L model (GRPIC3), thus indicating a transition from many plasmoids to few. We also observe disruption of the current sheet by rapidly growing kink modes in the large-r_L model (GRPIC3).

Appendix K: Collisionality of the Reconnection Layer

The reconnection is collisionless when the plasma skin depth λ_p is larger than the elementary current-sheet width in the resistive-MHD chain $w \sim 100\eta/v_A \sim 100\eta/c$ [64, 165], where η is the diffusivity due to coulomb collisions of pairs. Here we estimate analytically when this condition is satisfied. Following [181], we assume that the pressure of electron-positron pairs and radiation balances magnetic pressure in the reconnection layer,

$$P_{\rm rad} + P_{\rm pairs} = \frac{B^2}{8\pi}, \tag{K.1}$$

where $P_{\rm rad} = (1/3)aT^4$ is the radiation pressure, $P_{\rm pairs}$ is the pressure of the pair plasma, B is the upstream magnetic field strength, and a is the radiation constant. When $k_BT \ll mc^2$, radiation pressure dominates the LHS of Eq. K.1. At high temperatures $k_BT \gg mc^2$, $P_{\rm pairs} \approx (7/4)P_{\rm rad}$. We set $P_{\rm pairs} = (7/4)P_{\rm rad}$, which gives the temperature of the reconnnection layer

$$\frac{k_BT}{mc^2} \approx 0.3\ B_{12}^{1/2}. \tag{K.2}$$

It is a reasonable estimate of T in the non-relativistic and ultra-relativistic regimes. Then the Spitzer diffusivity due to coulomb collisions of pairs is given by

$$\eta = \frac{c^2}{4\pi}\frac{4\sqrt{2\pi}e^2m^{1/2}\ln\Lambda}{3(k_BT)^{3/2}} \approx 0.4\ B_{12}^{-3/4}\ {\rm cm^2s^{-1}}, \tag{K.3}$$

where we have set the coulomb logarithm $\ln\Lambda = 21$ [181]. It determines the elementary current sheet width

$$w = 100\eta/c \approx 10^{-9}\ B_{12}^{-3/4}\ {\rm cm}. \tag{K.4}$$

To estimate the density of pairs we assume annihilation balance in the reconnection layer: $e^+ + e^- \rightleftharpoons \gamma + \gamma$. When the plasma is non-relativistic ($k_BT/mc^2 \ll 1$) it gives $n = 2(k_BT/2\pi\hbar^2)^{3/2}\exp(-mc^2/k_BT)$, and the plasma skin depth follows as $\lambda_p = (mc^2/4\pi ne^2)^{1/2}$. When the plasma is ultra-relativistic ($k_BT/mc^2 \gg 1$) the density is given by $n = 1.202(3/2\pi^2)(k_BT/\hbar c)^3$, and the skin depth follows as $\lambda_p = (\langle\gamma\rangle mc^2/4\pi ne^2)^{1/2}$ where $\langle\gamma\rangle = 3k_BT/mc^2$ is the average particle lorentz factor. The two curves for λ_p join smoothly in the intermediate regime. Figure K.1 shows w and λ_p as a function of B. It suggests that the reconnection is collisionless when $B \ll 10^{12}$ G. However, a self consistent numerical calculation including detailed pair production and collisional physics is required to determine the reconnection rate if the magnetic field is very strong $B \gtrsim 10^{12}$ G, or if pair production is very efficient.

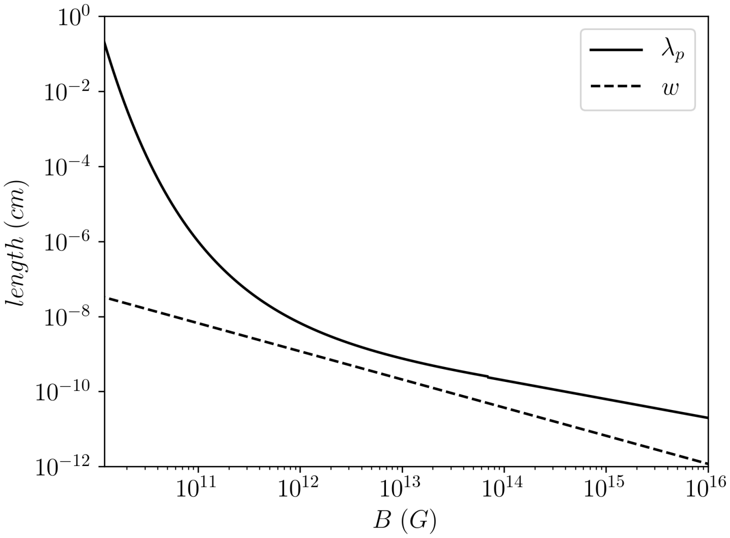

Figure K.1: Elementary current-sheet width w and plasma skin depth λ_p vs magnetic field strength in the upstream, B.

Appendix L: Magnetic Flux Decay Timescale

The flux decay can be understood analytically by assuming a constant reconnection rate at the stagnation surface, and neglecting plasmoid formation. The integral form of Faraday's law gives

$$\frac{d\Phi}{dt} = -2\pi c E_\phi, \tag{L.1}$$

where we have evaluated the line integral on a circle of radius r_0 at $\theta = \pi/2$ (the stagnation surface on the equator). The flux is given by

$$\Phi = \frac{1}{2}\int_0^\pi \int_0^{2\pi} |B^r|\sqrt{\gamma}\, d\theta d\phi, \tag{L.2}$$

where $\sqrt{\gamma}$ is the spatial metric determinant. In this toy model the global flux decay is determined the local electric field E_ϕ at the equator on the stagnation surface. We make the ideal MHD approximation $E_\phi = \sqrt{\gamma}(v^\theta B^r - v^r B^\theta)/c = \sqrt{\gamma} v^\theta B^r/c$, since $v^r = 0$ on the stagnation surface. Converting the velocity to a physical (tetrad) component $v^{\hat{\theta}} = \sqrt{g_{\theta\theta}} v^\theta$, gives

$$E_\phi = \sqrt{\gamma}\frac{v^{\hat{\theta}} B^r}{r_0 c}. \tag{L.3}$$

Assuming uniform $B^r(\theta, r_0)$ would give $\Phi \approx \mathcal{S}(r_0) B^r$, where $\mathcal{S}(r_0)$ is the hemisphere area at radius r_0. However, the distribution of $B^r(\theta)$ is non-uniform and concentrated near the poles, similar to the asymptotic pulsar wind in Minkowski spacetime [182]. This is because our simulations begin with a dipole field which is twice as strong at the poles compared to the equator. The dipole field is then opened, resulting in a non-uniform split-monopole [183]. Therefore, we make the more precise statement $\Phi = k\mathcal{S}(r_0) B^r(r_0, \pi/2)$, where we measure $k \approx 1.7$. Combining this result with

Equation L.1 and Equation L.3 gives

$$\frac{d\Phi}{dt} = -\frac{2\pi\sqrt{\gamma}v^{\hat{\theta}}}{r_0 k \mathcal{S}(r_0)}\Phi. \tag{L.4}$$

It implies exponential decay of Φ on the timescale

$$\tau = \frac{r_0 k \mathcal{S}(r_0)}{2\pi\sqrt{\gamma}v^{\hat{\theta}}}, \tag{L.5}$$

similar to the result of [166]. Equation L.5 gives $\tau \approx 3r_g/v^{\hat{\theta}}$ for $r_0 \approx 2r_g$.

Appendix M: Luminosity

Figure M.1 shows the flux of conserved energy passing through spherical shells of radius r as seen by an observer at infinity. The flux is normalized to units of

$$L_{\mathrm{BZ}} = \kappa \frac{\Omega_H^2 \Phi^2}{4\pi c}, \tag{M.1}$$

where $\kappa = 0.053$ for a split monopole [167]. The luminosity is dominated by the integrated Poynting flux, except in plasmoids in GRPIC simulations, where the particle luminosity can meet or exceed that of the fields. The particle luminosity is dominated by positrons in the GRPIC simulations because a net positive charge is required to support the rotating split-monopole with $\boldsymbol{\Omega} \cdot \boldsymbol{B}_p > 0$ in both hemispheres. The particle luminosity in the ergosphere is mainly due to inward going positive energy particles. Large deviations in Poynting flux are seen at the location of plasmoids in GRPIC, while in GRRMHD the deviations are much smaller because of the smaller plasmoid sizes.

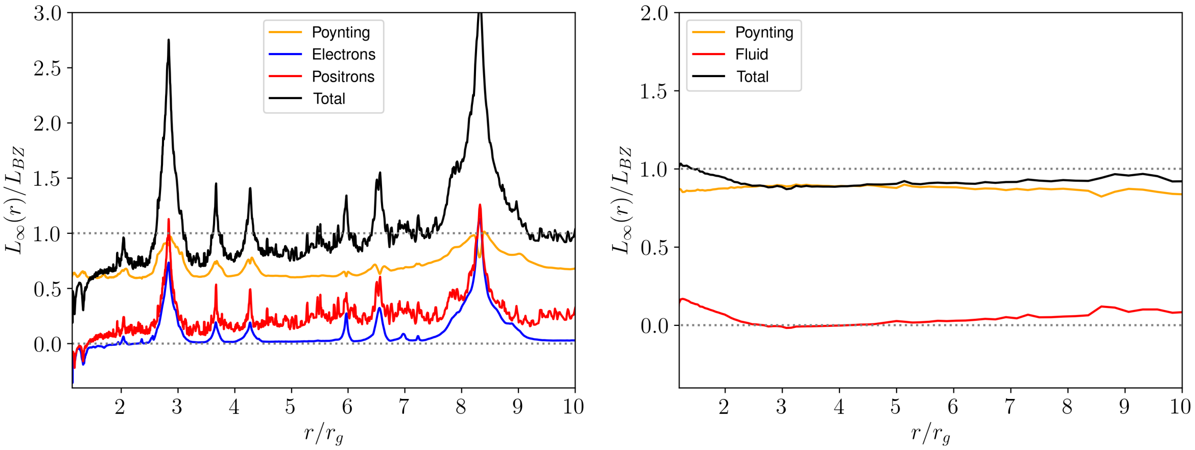

Figure M.1: Flux of conserved energy through spherical shells of radius r, as seen by an observer at infinity in units of L_{BZ}. Left panel: GRPIC1 at $t = 100\ r_g/c$. Right panel: GRRMHD1 at $t = 311\ r_g/c$.